Dissertation

submitted to the

Combined Faculty of Natural Sciences and Mathematics

of Heidelberg University, Germany

for the degree of

Doctor of Natural Sciences

Put forward by

M.Sc. Jürgen Michael Göck

born in Heidelberg

Oral examination: October 20$^{\text{th}}$, 2020

A novel approach for mid-infrared spectroscopy of large carbon systems and the nonthermal fragmentation process of diatomic anions

Referees: **Prof. Dr. Klaus Blaum**

Priv.-Doz. Dr. Robert Moshammer

Eine neuartige Spektroskopiemethode großer Kohlenstoffsysteme für den mittleren Infrarotbreich und der nichtthermischen Fragmentierungsprozess von zweiatomigen Anionen:

Die kryogene, elektrostatische Ionenfalle (CTF) ist für eine Machbarkeitsstudie zur laserinduzierten Emissionsspektroskopie (LIVE) mit einem Detektionssystem für den mittleren Infrarotbereich ausgestattet worden. Das neuartige, hochsensitive Detektionssystem basiert auf Sensoren, die das BIB-Prinzip nutzen. Um das Detektionssystem nicht schon ohne Ionensignal zu sättigen, muss die Schwarzkörperhintergrundstahlung drastisch unter Raumtemperaturniveau gesenkt werden. Es darf nur einer geringe Schwarzkörperhintergrundstrahlung vorherrschen. Um Raumtemperatureinträge zu unterdrücken sind Strahlungsschilde installiert worden.
Der nicht-thermische Autorfragmentationsprozess zweiatomiger Anionen aus Kohlenstoff, Cobalt und Silber ist im kryogenen elektrostatischen Speicherring CSR untesucht worden. Der COMPACT-Detektor auf der entsprechenden Fragmentposition registiert geladenen Fragmente, welche nicht mehr stabil gespeichert werden. Neutrale Fragmente sind entweder durch NICE oder durch COMPACT, auf der Neutralfragmentposition nachgewiesen worden. Die Zerfallskurven, welche von einem einfachen 1/t Potenzgesetz abweichen sind durch zwei verschiedene Ansätze beschrieben und diskutiert worden. Die Funktion zur Anpassung an die Datenpunkte benötigt die Tunnelkonstanten und eine Verteilung der Rotations- und Vibrationszustände. Die Tunnelkonstanten wurden vorab mit dem Programm LEVEL16 berechnet. Die beiden Ansätze versuchen die Verteilung der Rotations- und Vibrationszustände auf verschiedene Arten finden. Die Zerfallskurven der zweiatomiger Anionen sind bis zu 1000 s gemessen worden.

A novel approach for mid-infrared spectroscopy of large carbon systems and the nonthermal fragmentation process of diatomic anions:

The proof-of-principle experiment for Laser Induced Vibrational Emission (LIVE) spectroscopy requires the Cryogenic Trap for Fast ion beams (CTF) to be equipped with a mid-infrared detection system. The novel detection system is based on Blocked Impurity Band (BIB) sensors with a high sensitivity. The detection system requires a low black-body background to avoid saturation. The sequential installation of radiation shields reduces the black-body background of the CTF substantial.
The non-thermal auto-fragmentation process of the diatomic anions of carbon, cobalt and silver is studied at the Cryogenic Storage Ring (CSR). Charged fragments leaving the closed orbit of the CSR are detected by COMPACT at fragment position. Neutral fragments are detected either by NICE or by COMPACT at neutral position. The decay curves which deviate from a simple 1/t power-law are fitted and discussed by two approaches. The fit function requires the tunneling constants and a distribution of the ro-vibrational states. The tunneling constants were calculated by the program LEVEL16. Both approaches try to find the distribution of ro-vibrational states by different methods. The decay pattern of the diatomic anions are measured up to 1000 s.

Contents

1 Introduction

Electrostatic storage devices which are cooled to cryogenic temperatures can open up new scientific opportunities in gas phase spectroscopy of molecular and cluster ions. As stated in many articles and reports, these machines offer conditions allowing infrared-active molecules to cool to their ro-vibrational ground states [Lange, Froese, et al. 2010; Schmidt et al. 2017] due to the low ambient blackbody radiation field. The Cryogenic Storage Ring (CSR) and the the Double ElectroStatic Ion Ring ExpEriment (DESIREE) in Stockholm are the first large scale electrostatic storage rings which can be operated at cryogenic temperatures. Both devices reach temperatures below 15 K ($T_{\mathrm{CSR}} < 6K$ [Hahn et al. 2016]; $T_{\mathrm{DESIREE}} \approx 13K$ [Gatchell et al. 2014]).
The effective temperature of a molecule does not only depend on the ambient photon field, but also on the spectral sensitivity of the molecule itself. The ambient photon field is dominated by higher temperature contributions. The effective equilibrium temperature of the molecule can be higher than the average ambient surface temperature of the device due to the interaction of the molecule with ambient photon field which has contributions from the room temperature environment. The ambient photon field is determined by the blackbody radiation spectrum. Spectral Radiant Exitance (SRE) [Kark 2014] characterizes the black body radiation spectrum of a surface with the temperature T. The SRE, the emitted total power per unit area of the source surface per unit wavelength, is shown color-coded in fig. 1.1 for various temperatures. The SRE can be calculated for a given temperature by:

$$\mathrm{M}^{\circ}_{\lambda}(\lambda, T)\mathrm{d}A\mathrm{d}\lambda = \frac{2\pi\mathrm{hc}^2}{\lambda^5}\frac{1}{\mathrm{e}^{\left(\frac{\mathrm{hc}}{\lambda k_B T}\right)} - 1}\mathrm{d}A\mathrm{d}\lambda. \tag{1.1}$$

Wien's law describes the temperature depending shift of the spectral maximum as shown in fig. 1.1. The derivative of eqn. (1.1) with respect to λ yields the expression:

$$\frac{\mathrm{d}}{\mathrm{d}\lambda}\mathrm{M}^{\circ}_{\lambda}(\lambda, T) = -5 + \frac{\frac{\mathrm{hc}}{\lambda \mathrm{k_B} T}}{1 - \mathrm{e}^{-\frac{hc}{\lambda \mathrm{k_B} T}}}. \tag{1.2}$$

To access the extrema of eqn. (1.1), eqn. (1.2) has to equal zero. Substitution of $x = \frac{\mathrm{hc}}{\lambda \mathrm{k_b} T}$ leads to:

$$5 = \frac{x}{1 - \mathrm{e}^{-x}} \tag{1.3}$$

$$x = 4.96511423 \tag{1.4}$$

The re-substitution then reveals the classical Wien's law: $\lambda_{\max} = \frac{2.8977 \cdot 10^{-3}\ \mathrm{m\ K}}{T}$.

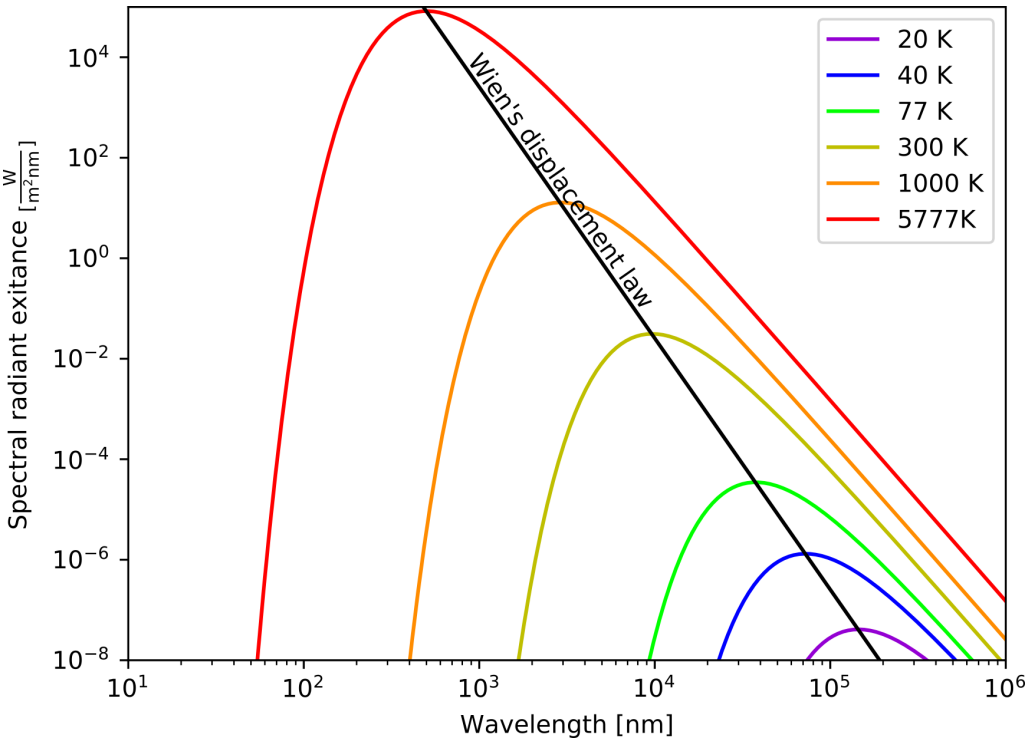

Figure 1.1: Blackbody radiation spectra for various temperature values (see eqn. 1.1). The temperature depending shift of the spectral maximum according to Wien's displacement law is shown.

Two thermometry experiments employing different molecules were performed at the CSR. Both experiments were probing the ambient photon field with known available transitions. One experiment used photo fragmentation of CH^+ yielding an effective temperature of ~ 20 K [O'Connor et al. 2016]. In a second experiment studying photo detachment of OH^-, an effective temperature of 15.1 ± 0.1 K [Meyer et al. 2017] was determined. The difference of these temperatures compared to the vacuum chamber temperatures of 4 to 6 K arises from openings in the experimental chamber where light from surfaces at higher temperature can enter. A similar thermometry experiment with the hydroxyl anion OH^- was performed at DESIREE. The molecular temperature of OH^- for DESIREE was determined to be 22.0 ± 0.3 K [Schmidt et al. 2018]. The difference between OH^- thermometry experiments at the CSR and at DESIREE can be attributed to a different photon flux from the room-temperature environment and the higher background temperature of DESIREE.
As demonstrated by the thermometery experiments, Cryogenic storage devices can provide a low blackbody radiation background at surface temperatures below 10 K. This opens up a new perspective on direct fluorescence measurements by laser excitation of large molecules like fullerene and Polycyclic Aromatic Hydrocarbons (PAH). The fluorescence of these large molecules is expected in the mid-infrared spectral range [Léger, d'Hendecourt, and Defourneau 1989]. The low blackbody radiation background of cryogenic storage devices allow the direct measurement of the

re-emitted photons. Fig. 1.1 shows a reduction of the SRE between 300 K (yellow) and 20 K (violet) by at least 4 orders of magnitude in the spectral range from 5 μm to 75 μm. The fluorescence signal from the stored ions which are excited by a laser is expected to exceed the residual photon background. To follow this spectroscopic idea, the former test-bench for the CSR, the Cryogenic Trap for Fast ion beams (CTF), was equipped with a IR-detection system and additional infrastructure during this thesis.
Magnetic storage rings like the Experimental Storage Ring (ESR) at the Gesellschaft für Schwerionenforschung (GSI) in Darmstadt confine ions on an orbit. These devices have been employed as tools to closely examine ion-ion, ion-electron and ion-photon interactions in particle [Touschek 1961], atomic [Seelig et al. 1998] and molecular physics [Rahman and Schiffer 1986]. However, these devices have a major drawback as they can only store particles within a certain mass-range. The suppliable magnetic field strength of the bending magnets is technically limited and defines the mass-range of the device. Electrostatic devices like the CSR or DESIREE overcome this limitation. The kinetic energy E_{kin} and the charge q of the ions define the required settings for the bending elements to store the particles, independent of their mass m. It is essential to cover a large mass-range to examine the transition (see fig. 1.2) from single atoms, which are quantum-mechanically well understood, to large clusters with bulk material-like properties. The decay of various dimer anions have been studied within this work.

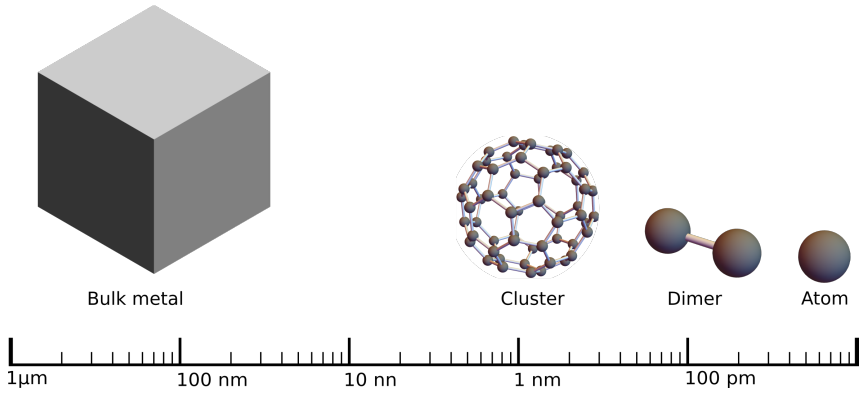

Figure 1.2: Size range from atoms to bulk metal inspired by [Hou et al. 2020]

2 LIVE Project

Laser Induced Vibrational Emission (LIVE) spectroscopy is a new experimental approach combining a cryogenic ion trap with a tunable laser system and a sensitive photon detection system to investigate mid-infrared emission of molecular species. The aim is the identification of ionic species by their absorption and emission features.

2.1 Motivation

Recent catalogs of the Diffuse Interstellar Bands (DIBs), which have been already discovered in 1922 [Heger 1922], listed more than 500 entries ranging from ∼400 nm to ∼1300 nm [Hobbs, York, Snow, et al. 2008; Hobbs, York, Thorburn, et al. 2009]. PAHs are regarded as potential carriers of the DIBs. In 1987 the existence of the charged PAH C_{60}^+ in the interstellar medium was postulated by Harry Kroto [Kroto 1987]. 1994 Foing and Ehrenfreund proposed two DIB lines being associated with C_{60}^+ [Foing and Ehrenfreund 1994] according to absorption spectroscopy in a neon matrix [Fulara, Jakobi, and Maier 1993]. Due to matrix broadening and line shifting, no final conclusion could be drawn. In 2015, four absorption features of C_{60}^+ were confirmed as DIB carrier [Campbell et al. 2015; Walker et al. 2015]. The experiment used an indirect method. A cryogenic 22-Pole trap was utilized to store and cool C_{60}^+. The cooling of the ions is facilitated by collisions with cold and dense helium gas which leads to cold $C_{60}^+ - He$ complexes. Subsequent resonant photon-fragmentation was applied to determine the absorption features of C_{60}^+ [Campbell et al. 2015]. In fig. 2.1 two of the known DIBs with the correlation to C_{60}^+ are shown. So far only C_{60}^+ features have been correlated to DIB lines.

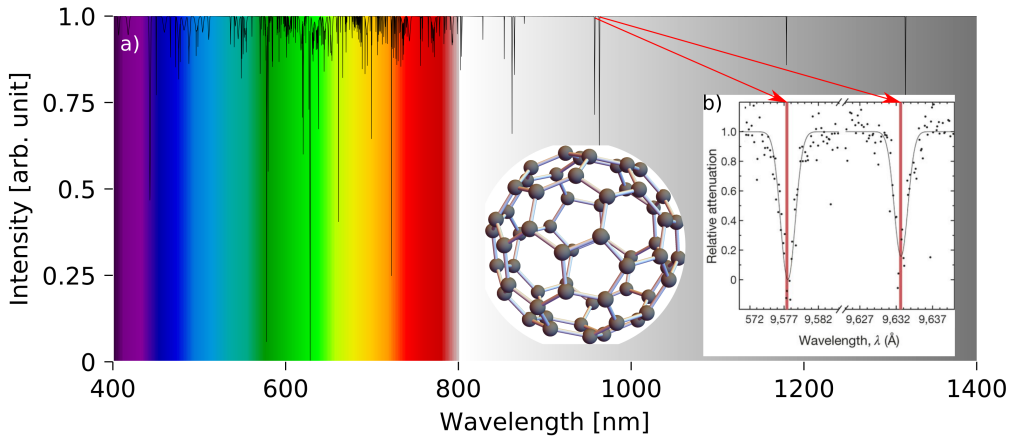

Figure 2.1: a) DIB spectrum generated from data of [Jenniskens]. b) Near-infrared absorption features of C_{60}^{+} from gas-phase spectroscopy. The graph of the insert was adopted from Campbell et al. [Campbell et al. 2015].

The so called Unidentified Emission (UIE) band, which have been observed in spectra of interstellar objects since the 1970's, could not be linked unambiguously to a carrier. The emission lines range from 3 μm to 20 μm, their spectroscopic properties point to carbon based molecules [Tielens 2008]. Conventional absorption spectroscopy addressing the spectra of PAHs is limited by the vapor pressure of the substrate. For example anthracene, a PAH consisting of three linear benzene rings (fig. 2.2 a)), has a vapor pressure of 0.258 Pa at a temperature of 347.25 K whereas coronene, a molecule consisting of seven benzene rings in rotational symmetry (fig. 2.2 b)), has a vapor pressure of 0.00191 Pa at 421.05 K [Oja and Suuberg 1998].

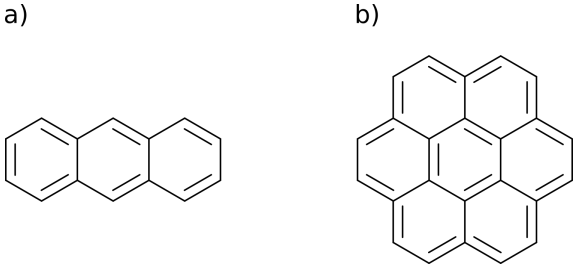

Figure 2.2: Structural formula of a) Anthracene and b) Coronene.

The column gas-phase density of the particles at room temperature is not sufficient to study the spectrum. To acquire a gas-phase sample with a sufficient density, the substrate requires heating, introducing an IR radiation background from the particle source [Schlemmer et al. 1994] and exciting the particles. The resulting spectrum is difficult to disentangle. Additionally, the high IR photon flux above 4μm (see for comparison fig. 1.1 at 300 K) is limiting the experimental IR sensitivity beyond

4μm [Schlemmer et al. 1994]. Classical laser induced fluorescence experiments do not apply to fullerene and large molecules as the fluorescence is not emitted in the visible to near infrared range. Furthermore, the two-color two-photon gas phase spectroscopy of fullerene and large molecules is in most cases not possible due to the fast internal redistribution process which is faster than fragmentation. One possible method to address the emission spectra of fullerene and PAHs is the Single-Photon InfraRed Emission Spectroscopy (SPIRES) which was used by Saykally et al.. The sample was irradiated by an UV-excimer laser to evaporate and excite the ions. The IR-fluorescence was dispersed by a cryogenic monochromator. The intensity of separated wavelengths were then measured by a block-impurity band solid-state photo-multiplier [Schlemmer et al. 1994; Cook et al. 1996].

2.1.1 Laser Induced Vibrational Emission (LIVE) spectroscopy

The principle methods of laser induced florescence can be transferred to ions stored in an electrostatic trap. Laser excitation in the visible to near-infrared spectral range followed by the rapid internal conversion to lower energies levels over the wast vibrational bands lead to the re-emission of photons in the mid-infrared region ∼100 ms after absorption. This principle is applied as Laser Induced Vibrational Emission (LIVE) spectroscopy. To perform this direct gas-phase spectroscopy method we implemented Blocked Impurity Band (BIB) detectors with a very high sensitivity in the field free region of the cryogenic linear electrostatic ion beam trap (Cryogenic Trap for Fast ion beams—CTF) [Lange, Froese, et al. 2010]. The cryogenic environment suppresses the blackbody radiation from 300 K surfaces. Additionally the trap allows the data acquisition for hundreds of milliseconds by storing the particle. Linear electrostatic ion beam traps were introduced by Zaifman as an intermediate step between the high energy storage rings and the low energy Paul or Penning traps for cluster or molecular ions [Zajfman et al. 1997]. In 1990 the electrostatic storage principle was applied in atomic ion studies as Multi-Reflection Time-of-Flight Mass-Spectrometer (MR ToF MS) by Wollnik [Wollnik and Przewloka 1990]. The CTF reaches temperatures below 15 K and a residual particle density corresponding to a pressure of about 10^{-14} mbar at room temperature. Within the LIVE project we propose to store C_{60}^{+}-ions in the cryogenic ion beam trap. Resonant laser excitation by a tunable pulsed laser system (OPO) will be applied followed by the detection of emitted infrared radiation with the BIB-detector. This might lead to the first direct background-free gas-phase absorption spectroscopy of molecular ions.

2.2 Experimental Setup

The CTF is an electrostatic ion beam trap which is operated between room and liquid helium temperature. Two vacuum systems, radiation shields and superinsulation are constructed in an onion shell structure to suppress heat input by blackbody radiation on the inner experimental vacuum chamber at cryogenic temperatures.

The outer most part is the isolation vacuum, followed by several layers of super-insulation, which are mounted on the 80 K radiation shield. The system is completed by a 40 K radiation shield surrounding the experimental chamber. The multilayer insulation and the two-step radiation shield reduces the blackbody radiation significantly [Lange, Froese, et al. 2010]. The outer isolation vacuum reduces the thermal flux by convection. To reduce the heat conductivity, inconel wires are used to hold the experimental chamber in place. Each wire connection for temperature sensors and high-voltage feedthroughs is thermally anchored on the 40 K and 80 K shields for proper thermalization respectively. The inner chamber is cooled by a closed-cycle refrigeration system with a cooling power of ∼20 W at 2 K [Hahn et al. 2016]. This allows the CTF apparatus to reach temperatures below 15 K and residual gas pressures of about 10^{-14} mbar [Lange, Froese, et al. 2010]. The trap of ∼800 mm length consists of two electrostatic mirror stacks, each equipped with an Einzellense focusing towards the trap center. Each electrode has a central aperture of ∼40 mm for ion injection, escaping neutralized fragments, and laser irradiation of the ion beam. Between the mirrors a field free region of ∼300 mm length for interaction experiments is available. The trap is connected to an electrostatic ion beamline with two source ports. One port is utilized for a Middelton Ion Sputter Source or a Laser-ablation source. It contains a mass-selecting magnet to separate the molecular and cluster ion species. The other port is connected to the CTF via a purely electrostatic beamline and hosts a Knudsen-Cell type ion source for the production of C_{60}^{+} and C_{60}^{-} (see fig. 2.3).

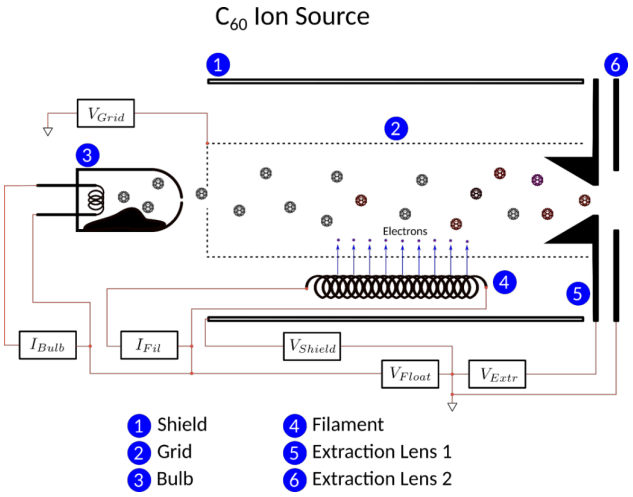

Figure 2.3: Schematic view of the C_{60} source.

The ions are accelerated up to 5 keV. After acceleration the ions are focused by an Einzellense with vertical and horizontal steerers. The beam is bend by a double-focusing deflector by 90° and further guided towards the trap. In order to inject ions into the trap, the potentials of the first set of mirror-electrodes (right set of potentials fig. 2.4) is switched off and back on before the ions can escape the trap after being

reflected at the second set of mirror-electrodes. The operation of the trap needs a working point, i.e. a set of electrode voltages allowing a potential depth between 4 keV and 7 keV. For the LIVE project, a Micro-Channel Plate (MCP) detector system in chevron configuration with a central hole of ∼8 mm was implemented behind the second mirror stack. The MCP set allows the detection of neutral particles leaving the trapping region in forward direction. The central hole was a necessity to allow laser beams to be aligned on the horizontal axis. To detect the escaping neutral particles, the trap is then operated with a special set of voltages, leading to an ion density distribution where the trapped ions are concentrated in a ring around an empty trap center.

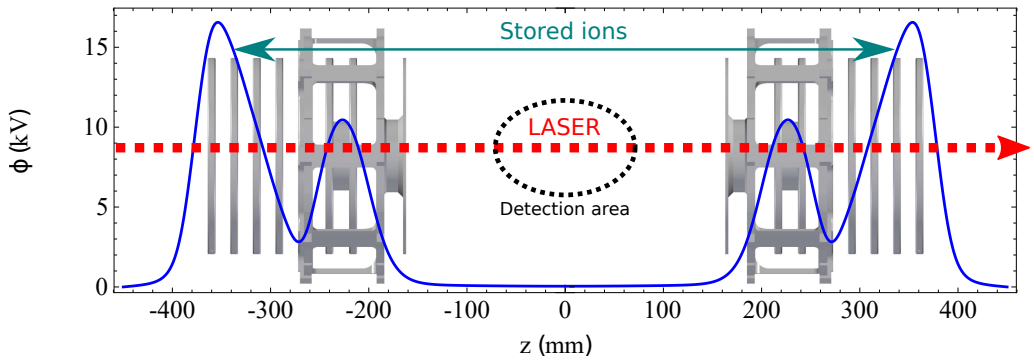

Figure 2.4: Lateral view of the CTF trapping potentials (blue curve). The laser is guided on the trap axis against the beamline direction. The shown potentials were calculated to trap an ion beam with a kinetic energy of ∼ 15 keV [Grieser 2019]. For details see text.

Standard operation modes typically lead to density distributions concentrating the ions in the trap center [Menk 2013]. Two modifications were designed to reduce the radiation flux into the central experimental chamber: A rejuvenation cooled to cryogenic temperatures in the injection beamline in order to reduce infrared radiation from the environment (left magnification in fig. 2.5) and a multilayer copper shield replacing the MCP detection system, to reduce infrared radiation from the backside of the CTF (right magnification in fig. 2.5). The mulilayer copper shield is a temporary installation for base-line tests of the detector system without an ion beam. It was installed to reduce the infrared background from the pumping system and the view-port. Multiple reflections of the photons on the metal surface increase the absorption probability and therefore reduce the infrared background in the central chamber.

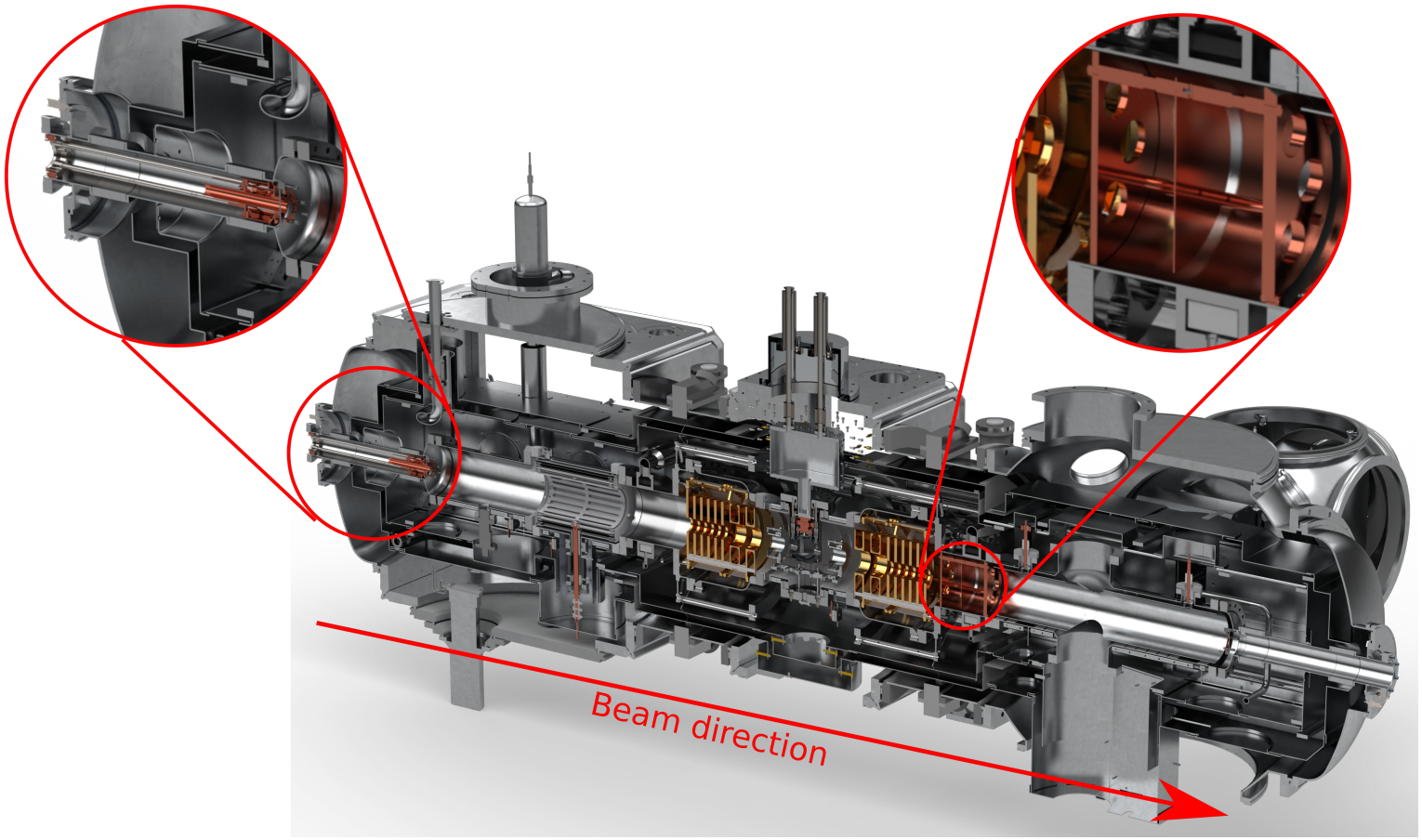

Figure 2.5: Lateral schematic view of the CTF [Lange, Blaum, et al. 2008; Lange, Froese, et al. 2010]. The gold-plated electrostatic mirrors with cylindrical symmetry are positioned in the central chamber. Two modifications to reduce the infrared background are magnified: the cryogenically cooled rejuvenation of the injection beamline (left magnification) and the radiation shield at the extraction site of the trap (right magnification) (for more information see chap. 2.3.2).

2.3 Mid-Infrared Detection System

The key part of the LIVE project is the implementation of a mid-infrared detection system into the CTF. The detector is located in the field free region between the electrostatic mirror sets. It replaces the former central pick-up system. The detector itself, the required infrastructure, electronics and new shielding concepts are discussed in the following.

2.3.1 Setup

Due to the operation temperature of the BIB detectors of about 5 K, a separate liquid helium cryostat with a volume of 4.5 l was implemented into the central experimental and isolation vacuum chambers of the CTF. The cryostat is surrounded by a copper shield (see fig. 2.7 a)), which is connected by copper mesh strips to the cryogenic cooling system of the CTF. This connection supplies the cooling power for the copper shield as well for the pre-cooling of the cryostat. The cryostat itself is only weakly coupled to the cryogenic cooling system of the CTF, balancing out the thermal load on the cryostat at liquid helium temperatures and the pre-cooling without liquid nitrogen. Therefore, it is suspended inside the copper shield by ten lace screws. The filling tubes are decoupled by long bellows towards room temperature environment and the connection flange to the central chamber is decoupled by a bellow and long rods (see fig. 2.7 b)). Depending on the temperature environment of the CTF, a maximum refilling cycle of 36 h was achieved for this cryostat. The small copper block, which is connected to the bottom surface of the liquid helium reservoir, thermalizes and cools the BIB detector block down to ~ 5 K (see fig. 2.7 c) for optimal operation. A small heating resistor serves for temperature stabilization at 5 K. An optical mirror system focuses the mid-infrared photons on four BIB detectors (see fig. 2.7 d)) which are protected by a longpass filter transmitting only photons above 4 μm. Four BIB detectors were connected to three Junction Field-Effect Transistor (JFET) pairs. Two BIB detectors were individually connected to a JFET pair. The two remaining detectors were connected in parallel to a JFET pair. The amplification and conversion of current to voltage is carried out by the circuit shown in fig. 2.8. To reduce noise effects and capacitance, the JFET pairs are positioned as close as possible to the BIB detectors. After a short warm up the JFETs are self heating by the flowing current. The thermal noise voltage of a resistor can be calculated by:

$$U_{R,\mathrm{eff}} = \sqrt{4\mathrm{k_B}TR\Delta f}. \tag{2.1}$$

It depends on the absolute temperature T, the resistance R and the frequency bandwidth Δf. Therefore the feedback-resistor was placed on the liquid helium cooled substrate in close proximity to the BIB-detectors. The BIB detector acts as photo-sensitive resistor. A current arises from the negative bias voltage and acts via capacitance as a negative gate voltage. The gate voltage trims the current over the JFET. Therefore the voltage on the inverting input of the operational amplifier gets

reduced. No current can flow over the gate of the JFET. The amplifier forces the inverted input back to the original voltage by adjusting the voltage on the output. Flowing current over the feedback resistor compensates the detector current. The amplification factor follows from the feedback resistor. The detector current can be calculated by Ohm's law:

$$I_{\text{det}} = \frac{U_{\text{out}}}{R_{\text{feedback}}}. \tag{2.2}$$

Fig. 2.6 shows the characteristic spectral responsivity of a BIB detector. The measurement was carried out at the Max-Planck-Institut für Astronomie in Heidelberg under optimal settings. The responsivity (A/W) describes the electrical (A) response of an optical detector depending on the power (W) per wavelength of the photons hitting the detector.

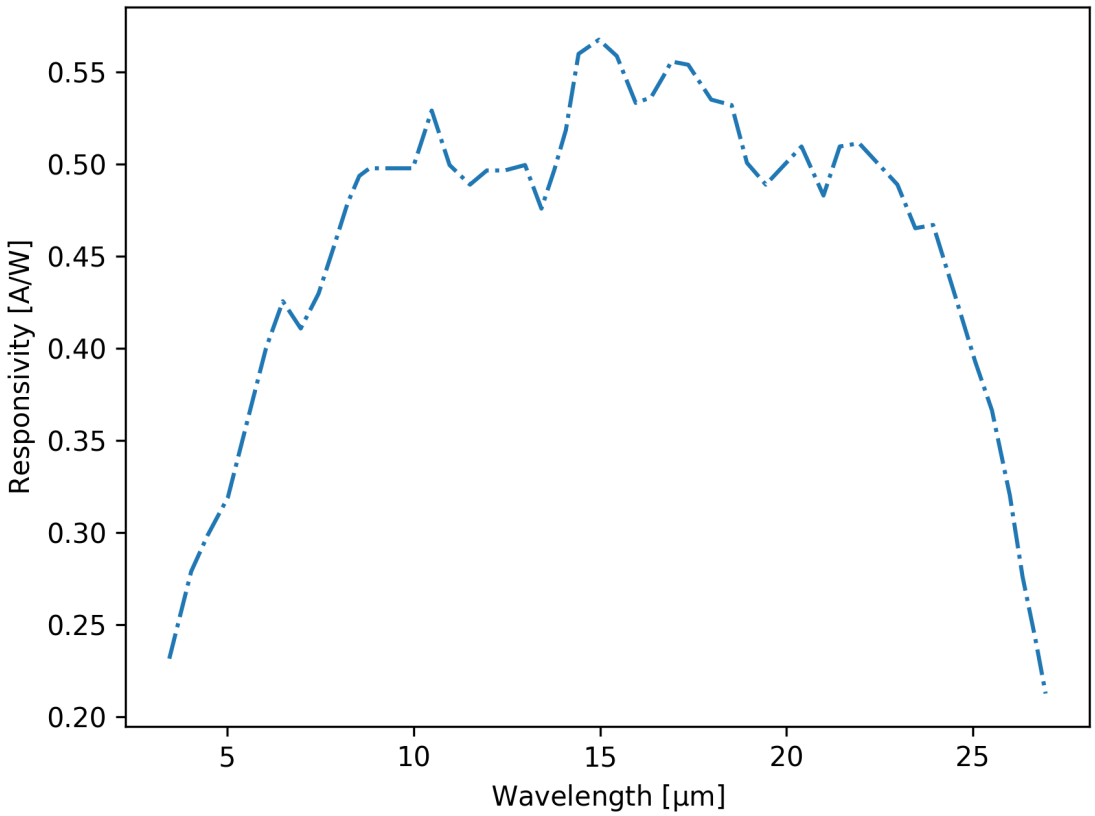

Figure 2.6: The characteristic spectral responsivity of a BIB detector. The dots are connected by splines.

The implemented circuit converts the current from the detectors into a voltage. The voltage response is therefore a measure for the number of photons hitting the detector. For a single known wavelength in a low background environment the

intensity of the emission line can be calculated from the resistance R_{feedback} and the responsivity. Employing a logging voltage-meter, the voltage response versus the laser wavelength can be observed.

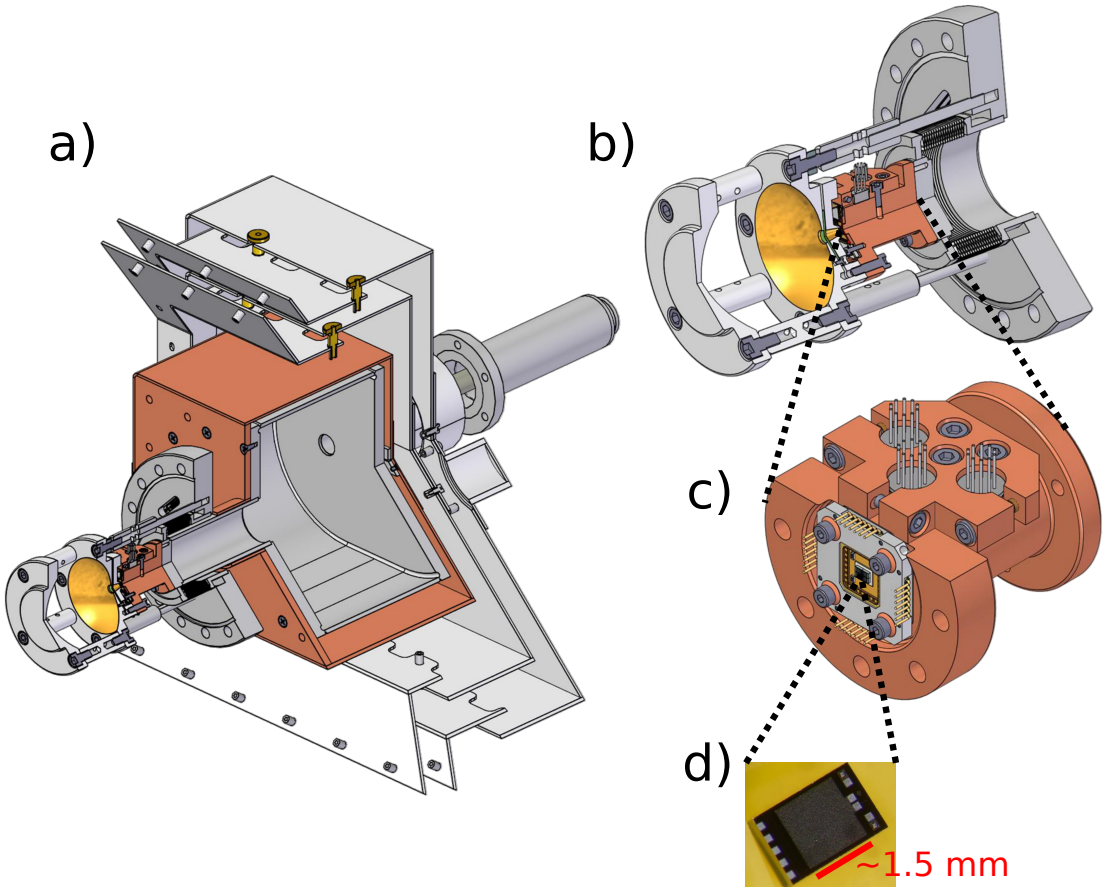

Figure 2.7: a) Detector setup connected to the LHe Dewar, including copper shield, 40 K, and 80 K shields, respectively. b) Gold-plated mirror system with mechanical support and mounted BIB detector. c) BIB detector within mechanical mounting and JFET stage on a copper finger for optimal thermal conductivity. d) Single BIB detector.

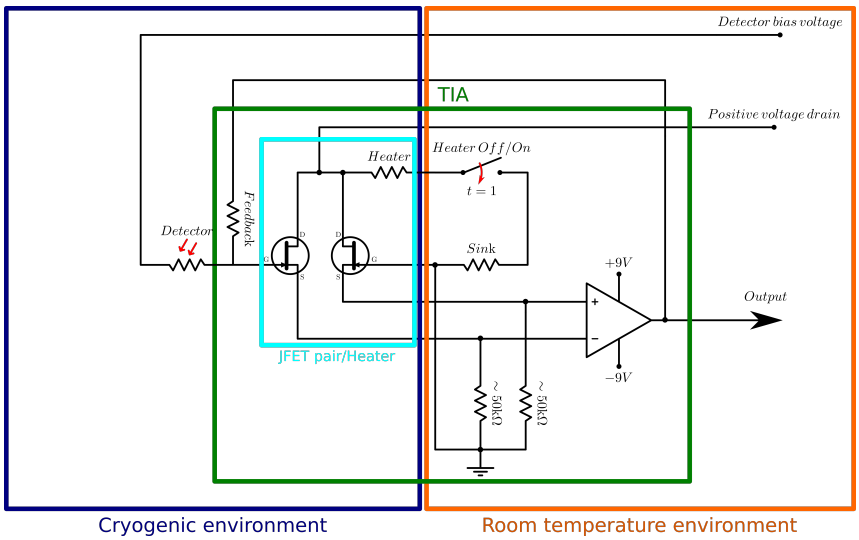

Figure 2.8: Electronic circuit for amplification and current-to-voltage conversion of the detector signal.

To increase the fraction of detectable photons emitted by the passing ion beam and therefore the signal strength, an optical mirror system was developed. For optimization of the geometry of the mirrors, ray-tracing simulations were performed. As result a special spherical and a special elliptical mirror were developed to focus the photons onto the detectors. Fig 2.9 shows a schematic drawing used in the ray-tracing software ZEMAX.

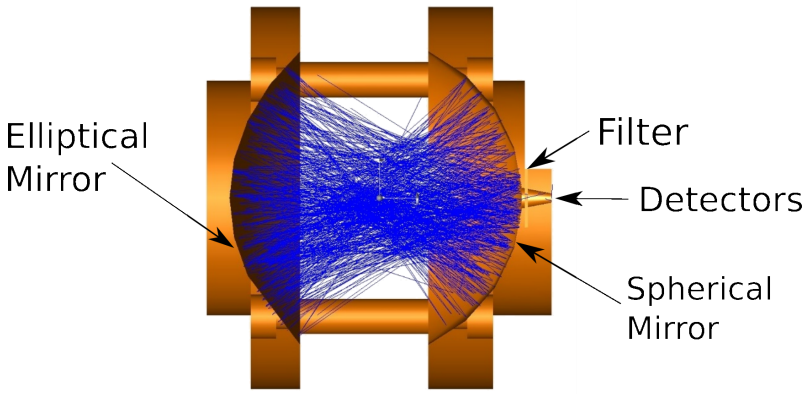

Figure 2.9: Ray-tracing simulation of the optical mirror system performed with ZEMAX.

The detectors are connected to the mirror system by a reflective cone. To guarantee an optimal reflectivity a mean surface roughness of $R_a < 4$nm was chosen combined with a gold coating. Stray light from the laser and the optical ports is blocked by a long-pass filter in front of the detector. The filter transmits wavelengths between 3 μm and 12 μm with an transmittance larger than 90%. In an optimal case the

simulations showed a signal-to-noise ratio of ~ 30 with photons of the wavelength 7.1 μm for the detection system.

2.3.2 Radiation Shielding

The commissioning tests of the detectors implemented in the CTF showed that they were already saturated far below the optimal operation voltage due to the background infrared radiation level. Thus, the radiation shielding was improved as discussed in the following. A cryogenic flap in front of the main pumping section was implemented. By closing this passively cooled cryogenic radiation flap the infrared background radiation from the 300 K environment is reduced [Lange, Froese, et al. 2010]. A schematic drawing of the connection between the experimental vacuum chamber and the pumping system is shown in fig. 2.10.

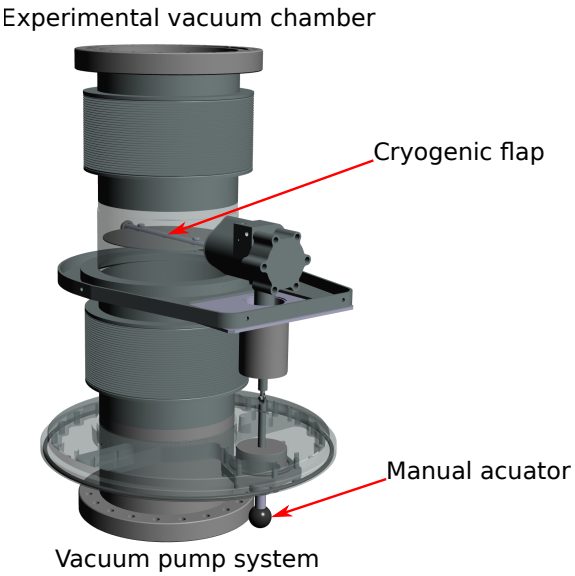

Figure 2.10: Schematic drawing of the intermediate vacuum chamber between experimental vacuum chambers and vacuum pumping system. The section containing the cryogenic flap is made transparent.

To shield the BIB detector system two additional radiation barriers were implemented in the experimental vacuum chambers of the CTF. At the side of the ion beam injection an actively cooled radiation barrier, narrowing the opening for the ion beam as well as for the room temperature radiation, was introduced. Fig. 2.11 a) shows the model of the shielding installed in the injection beamline. The holder of the shield is mounted at room temperature upstream in the beamline. It contains long and thin stainless steel rods for thermal decoupling. The shield is connected by 24 layers of ultrapure copper sheets (99.995%) to a cold head of type COOLPOWER 140 T from Leybold. It operates down to ~15 K with a cooling power of 20 W at 20 K. The temperature of the radiation shield was monitored by a PT1000 temperature sensor. The copper sheets are isolated against room temperature by 1 mm

thick polytetrafluroethylen sheets. Additional Marcor cylinders, with a height of 5 mm, support the copper structure to prevent direct contact with the room temperature vacuum chambers. Both insulators are protected by the grounded copper sheets to prevent a charging of the insulator surface which would deflect the ion beam. A second radiation shield temporarily replaces the MCP mounted behind the electrostatic trap setup in order to suppress room temperature radiation from the backside of the setup. Possible sources for IR-radiation from the backside of the trap are a port for a turbo-molecular pump and a saphire viewport. The model of the radiation shield and a picture of its installation are shown in fig. 2.11 b) and fig. 2.11 c), respectively. It is cooled passively by thermal contact to the experimental chamber. Its temperature is monitored by a PT1000 resistance sensor and a silicon diode. Both modifications significantly reduced the radiative background while keeping the minimal required gas flow for efficient pumping and safety of the experiment.

Technical requirements

For safety reasons, the mass flux through both radiation shields has to match a mass flux through a safety burst disk with a diameter of 40 mm. In case of a liquid helium leak inside the experimental vacuum chamber, the safety burst disks prevent a pressure build-up which could lead to a breakage of the experimental vacuum. By damaging the safety burst disks, the evaporating helium is vent into the isolation vacuum chamber. The isolation vacuum chamber has a safety flange which allows the helium to exit the system. The calculations to evaluate the effect of closing the flap and reducing the diameter of the experimental vacuum chamber by the radiation shields are based on a safety study in 2011 [Haberstroh 2011]. It estimated the risk of pressure build-ups by utilizing the mass flux equation through a surface area [J. D. Anderson 1982]:

$$\dot{m} = \rho\left(T\right) v_{\text{Sound}}\left(T\right) A. \tag{2.3}$$

To calculate the mass flux the speed of sound in helium was adopted as a mean velocity of evaporated helium. The temperature and pressure dependent quantities speed of sound and density were taken from [Lemmon, McLinden, and Friend 2020]. The variable A corresponds to the flux area in square meter. The mass flux relations are displayed in fig. 2.12.

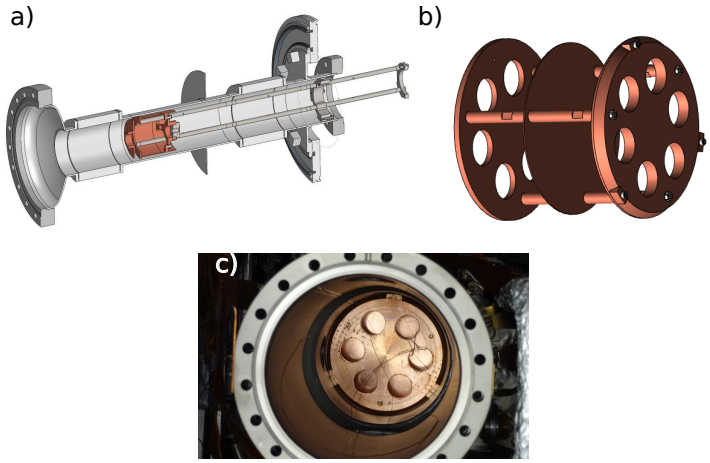

Figure 2.11: Radiation shields. a) Model of the radiation shield in the injection beamline. b) Model of the radiation shield at the backside of the EIBT. c) Picture of the mounted backside radiation shield.

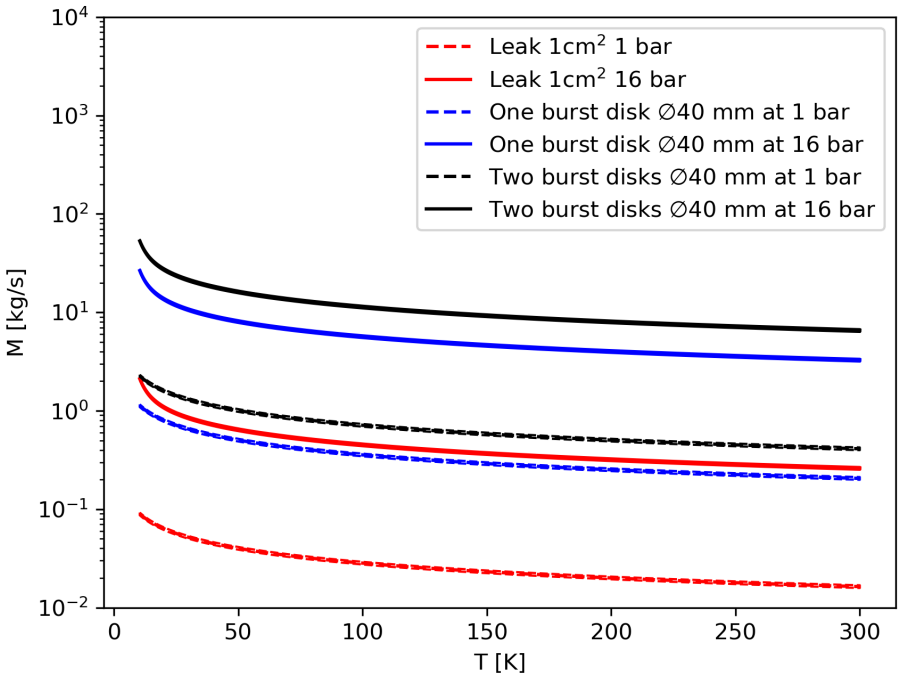

Figure 2.12: Mass flux through a helium leak at different pressures and through a safety burst disk of 40 mm diameter at different pressures. The uncertainty for each calculation appears as the thickness of the plotted lines. The maximal uncertainties were taken from the NIST database ($\Delta\rho\,(T) = 1\%$ and $\Delta v_{\mathrm{Sound}}\,(T) = 3\%$ [Lemmon, McLinden, and Friend 2020]).

As demonstrated in fig. 2.12, higher pressures in the helium system might exceed the safety limit of one safety burst disk. Therefore, the cryogenic flap in front of the turbo-molecular pump has to be fixed at an minimum angle of ∼18° to the horizontal axis. This flap position doubles the possible mass flux allowing a safe operation of the CTF by two operational safety burst disks.

2.3.3 Detector commissioning

Before its installation in the CTF at the Max-Planck-Institut für Kernphysik the BIB detection system was tested at the Max-Planck-Institut für Astronomie. General functionality and responsivity were successfully proven. Temperatures of ∼20 K as expected in the CTF introduce only a minimal background signal due to the persisting infrared background radiation. For optimal photon detection a bias voltage between -2 V and -4 V is required for the detectors. After installation in the CTF, performance tests of the detection systems were carried out. Due to massive infrared background radiation, the signal amplifier saturated significantly below the operational bias voltages of the detector. Thus, sources of infrared background radiation were subsequently identified and reduced.

First BIB detector operation at CTF

The first cryogenic operation at the CTF was performed after implementation of the BIB detectors. CTF was cooled down to about 20 K. The liquid helium cryostat was used to cool the BIB detection system to approximately 5 K. A test at room temperature which was performed before cool-down already indicated a working detection system. At cryogenic temperatures only tiny bias voltages were applicable $U_{\mathrm{bias}} > -0.2$ V before the saturation level of the output operational amplifier of $U_{\mathrm{out}} \approx 5$ V was reached. An adjustable reference voltage source was implemented (Gleichspannungsstandard Model 2003 0.02%) as source of the bias voltage. No particles were stored in the trap during these primary tests with the exception of one measurement during the first BIB detector operation at CTF. The evaluated behavior indicates a strong infrared radiation field inside the experimental vacuum chamber. The following table shows the bias voltages applied to detector 2 (Det 2) and the output voltages:

Bias voltage [V]	Output voltage [V]
0.03	-3.44±0.03
0.01	-1.22±0.01
-0.01	-1.14±0.01
-0.03	1.90±0.02
-0.10	2.60±0.02
-0.20	——–
-0.10	3.00±0.03

Table 2.1: Output voltage of Det 2 at given bias voltage. This part of the installed detection system utilizes a single pixel. The uncertainty of the output voltages corresponds to the measurement uncertainty of the used multimeter (Fluke 112: output voltage*0.7%+0.002V).

At a bias voltage of -0.20 V, the output voltage was drifting to higher values fast. Therefore, the bias voltage was reduced to -0.1 V and the output voltage stabilized at (3.0±0.03) V. Listed in table 2.2 are the measurements for detector 3 (Det 3), which detects more photons due to its doubled surface area (two pixels):

Bias voltage [V]	Output voltage [V]
-0.01	1.77±0.02
-0.10	——–
-0.08	4.29±0.04

Table 2.2: Output voltage of Det 3 at given bias voltage. This part of the installed detection system utilizes two pixels. The uncertainty of the output voltages corresponds to the measurement uncertainty of the used multimeter (Fluke 112: output voltage*0.7%+0.002 V).

To observe stable conditions, the bias voltage was reduced from -0.10 V to -0.08 V. The output signal was examined with a spectrum analyzer. By periodically varying the incidence of light into the CTF through a laser viewport periodically a clear signal of about $\sim$ 20 dBV at 2 Hz and a span of 85 Hz could be induced. The measurement scheme was repeated for detector 1. In the following table the applied bias voltages and the output voltages are listed:

Bias voltage [V]	Output voltage [V]
-0.05	1.83±0.02
-0.10	2.26±0.02
-0.15	2.80±0.03
-0.20	4.03±0.03
-0.20	4.23±0.04

Table 2.3: Output voltage of Det 1 at given bias voltage. This part of the installed detection system utilizes a different single pixel than Det 2. The uncertainty of the output voltages corresponds to the measurement uncertainty of the used multimeter (Fluke 112: output voltage*0.7%+0.002V)

The test with a time modulated light signal was repeated for Det 3. The bias voltage was set to -0.20 V and the output voltage was stable around 4.23 V. The acquired data of Det 1 from the spectrum analyzer with the same settings as for Det 3 is shown in fig. 2.13. A clear signal of $\sim$ 20 dBV at 2 Hz could be observed.

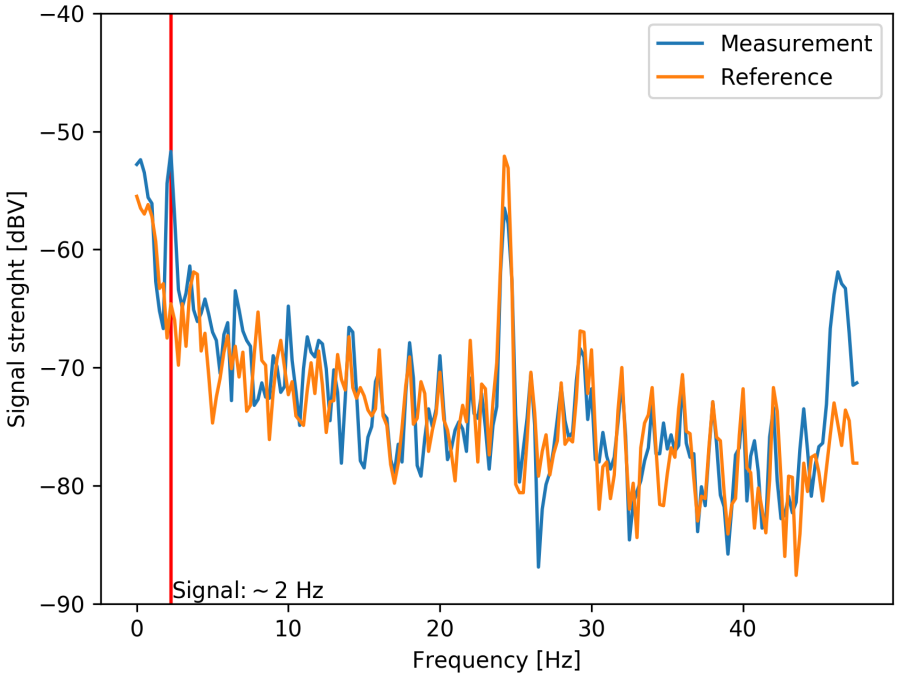

Figure 2.13: Acquired spectrum for Det 1. The instability in the time-modulated light signal might introduce the noise peak around 48 Hz.

C_{60}^{+} ions were stored and irradiated with pulsed laser light at the main absorption line 957.7 nm. The laser operated at a fixed frequency of 20 Hz. For the measurement every fifth laser pulse was picked by a shutter. This should lead to an emission signal at $\sim$4 Hz. Due to its larger surface area the detector pair (Det 3) was used for signal detection. The bias voltage was set to -0.09 V an output voltage of (4.30±0.04)V was

observed. Due to the high background radiation no ion signal could be identified, even with signal averaging of 450 times. The spectrum is displayed in fig. 2.14.

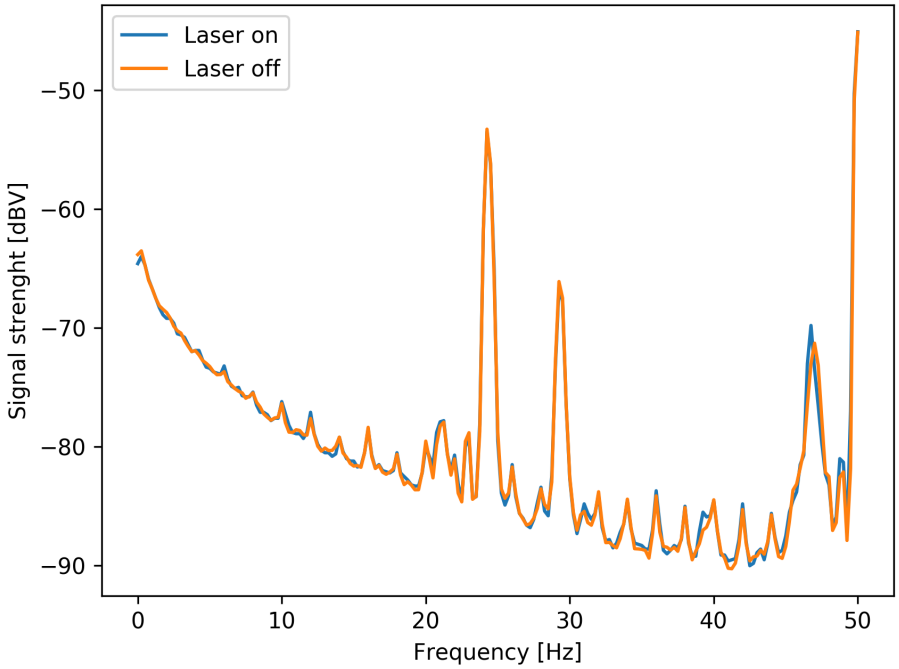

Figure 2.14: Signal spectrum from Det 3 when irradiating C_{60}^{+} with laser light at 957.7 nm no response at 4 Hz to the laser irradiation can be seen.

As a consequence of these tests, all unnecessary openings in the 40 K and 80 K shields were closed to minimize the influence from the 300 K blackbody background.

Shield modifications

At the second operation, the CTF was cooled down to ∼12 K. The detector reached temperatures around 5 K after filling the LHe cryostat. A functionality test for each detector was performed as before. Bias voltages and detector responses are listed in table 2.4. Compared to the first test the bias voltage could be increased to about -0.4 V for Det 1 and Det 2. Det 3 reached the limit of the amplifier for -0.3 V. Nevertheless, this is considerable below the optimal voltage range of -2 V to -4 V. During this test no signal could be induced artificially by time modulated external light sources at the remaining openings of the CTF. Only a resistor of 3.9 kΩ, which was implemented as a test source in close proximity to the mirror system, could introduce changes in the output voltage of the detection system.

	Det 1	Det 2	Det 3
Bias voltage [V]	Output voltage [V]		
0.0	-0.16±0.01	———	-0.16±0.01
-0.1	1.6±0.02	2.15±0.02	2.8±0.03
-0.2	2.2±0.02	2.5±0.02	3.5±0.03
-0.3	2.9±0.03	3.5±0.03	4.3±0.04
-0.4	4.6±0.04	4.5±0.04	———

Table 2.4: Output voltage of Det 1, Det 2 and Det 3 at given bias voltage. The uncertainty of the output voltages corresponds to the measurement uncertainty of the used multimeter (Fluke 112)

Unfortunately, the infrared background radiation still limits the applicable bias voltage. As a consequence, additional beamline radiation shields were designed, constructed and implemented to reduce the IR-background aiming for a bias voltage of ~ -2 V (see chap. 2.3.2).

Implementation of the radiation shield at the injection site

After implementation of the cryogenic injection, a new operation test of the detection system was performed. The CTF was cooled down to about 12 K and the detectors to about 5 K. During this test the bias voltage was limited below the saturation threshold for drift and infrared background tests. The bias voltage was incremented stepwise. After each step a relaxation time of a few minutes allowed the output voltage of the amplifier to stabilize. The results are shown in fig. 2.15. The stabilization time depends drastically on the step size of the bias voltage within the given limits. The larger this step, the longer the stabilization time. This was tested by reducing the bias voltage to 0 V for some time between two steps (see fig. 2.15). The relaxation behavior might result from the large feedback resistor ($\sim 10^{11}$ Ω) in the transimpedance amplifier circuit. Nevertheless, the equilibrium level is unaffected. In order to test the effect of the cryogenic modifications in the injection beamline, the beamline was slowly warmed up and the output voltage was monitored. As can be seen in fig. 2.16, the level of the detection systems output is almost unaffected within the measurement uncertainty. The detectors output voltage was stabilized for 700 s before the measurement was started. The cold head Displex DE 202 O.S.P limits the achievable minimal temperature around 145 K. In order to suppress the background for the detectors considerably, temperatures below 40 K are essential. To achieve this temperature range, a cold head with more cooling power is required.

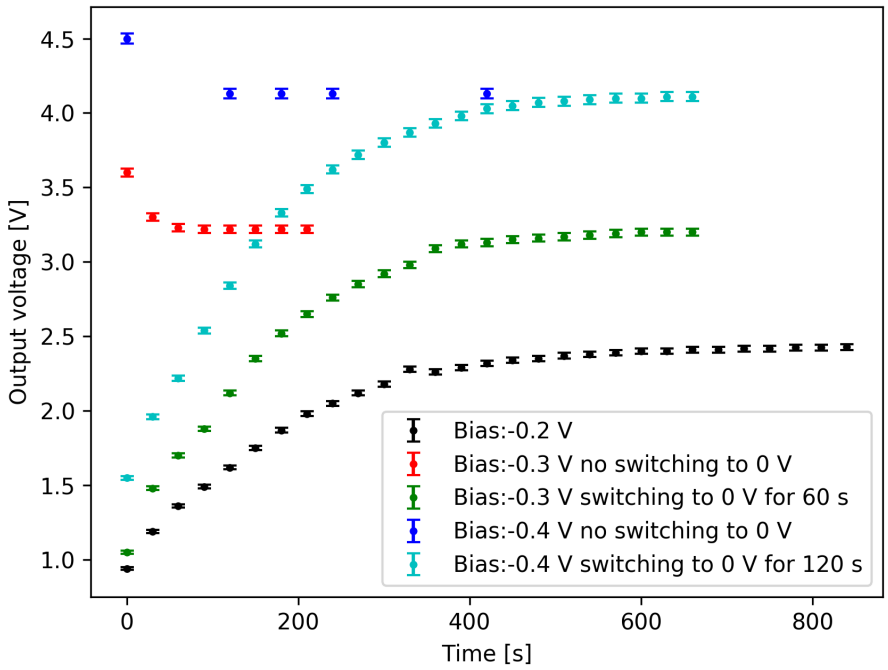

Figure 2.15: Drift measurement for Det 1 at different bias voltages below the saturation threshold. The shown uncertainty arises from the measurement uncertainty of the multimeter (Fluke112)

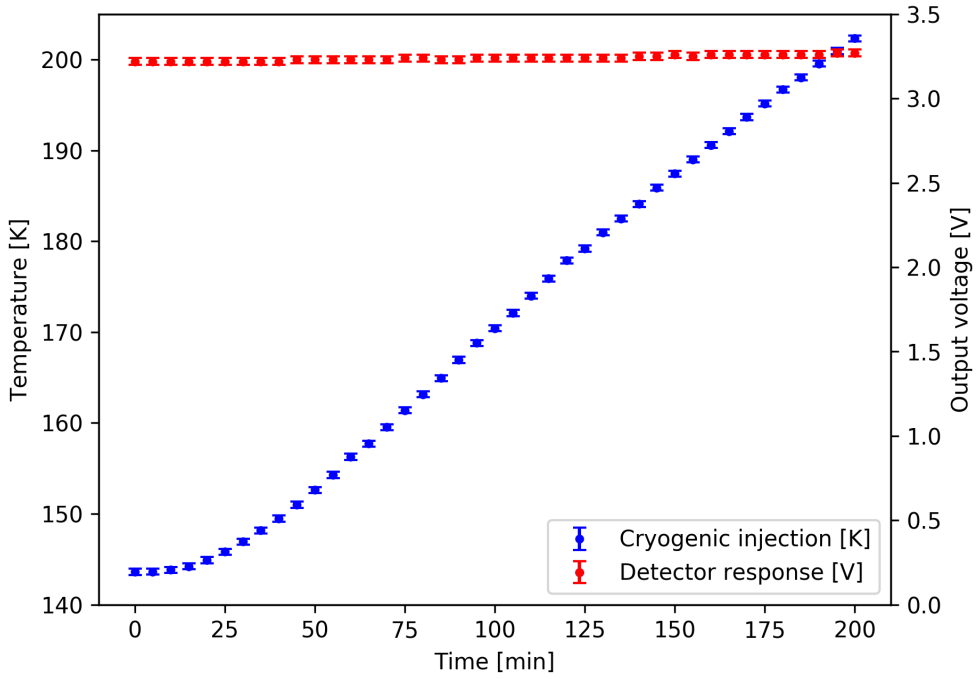

Figure 2.16: Impact of the cryogenic injection temperature on the output voltage of Det 1. The uncertainty is defined by the used instruments. The output voltage was measured with a Fluke 112. For the temperature measurement a Cryocon 24 C temperature controller was utilized. From the calibration curve of the Cryocon 24 C a maximal uncertainty of 0.33 K was estimated for the measured temperature region.

Reduction of infrared radiation by use of a cryopump

A cryogenic pump installed at the injection site of the CTF was used to additionally cool the injection part of the CTF and the response on Det 1 was observed. The temperatures of CTF was about 12 K. For the LHe cryostat, temperatures around 5 K were measured. A bias voltage of -0.3 V was applied to Det 1 without saturation. Three temperature sensors were monitored to acquire the temperature status of the cryo pump and of the cryogenic injection for this test. A minimal temperature of 125 K was registered for the cryogenic injection. Cooling down the cryopump to ∼120 K yielded an enormous effect on the detection system (see fig. 2.17). The output voltage dropped by nearly 1 V. Modifications to achieve temperatures below 30 K might yield better results.

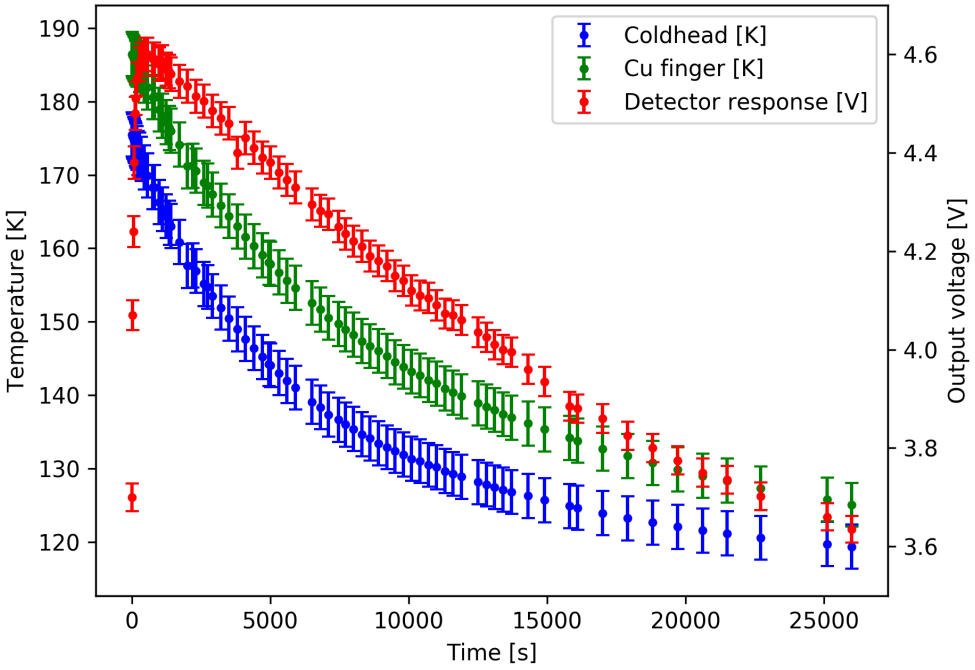

Figure 2.17: Correlation between cryogenic pump temperature and output voltage of Det 1. The output voltage was monitored with a multimeter (Fluke 112) and the uncertainty was treated as described in the manual and is included in the plot. The temperature was monitored by a custom made temperature monitoring system. The uncertainty was assumed to be ±3 K

Implementation of second radiation shield on the backside of CTF and further upgrades

The next update included a cold head of the type CP 140 T from the company Leybold. It replaced the coldhead Displex DE 202 O.S.P. with lower power from the company Air Products at the cryogenic injection. The multi-layer copper mirror as a passive element to reduce the infrared background was installed and replaced

the MCPs at the ion extraction side. The mirror stayed at a stable temperature of about 30 K over the test period. The CTF and the cryostat were cooled down to the nominal operation temperatures. Det 1 was operated with a bias voltage of -0.9 V. Depending on the position of the cryogenic flap (fig. 2.10), the output voltage varied between -3.0 V (closed flap) and -4.9 V (opened flap). From the bias voltage one can conclude that the IR background was reduced. Due to the unknown sensitivity, a calculation of the photon flux is not possible. A fully opened flap saturated the detector (output voltage:∼4.9 V). Det 2 and Det 3 could now be operated with a bias voltage of -1.2 V, showing a general trend of a reduced IR background. The effect of warming up the cryogenic pump (fig. 2.18) and the cryogenic injection were monitored separately by Det 1. The bias voltage was set to -0.3 V. Warming the cryogenic pump up to 160 K increased the output voltage by 0.35 V. The spikes in the detector response correspond to the opened cryogenic flap. For the cryogenic injection an increase of 0.1 V of the output voltage was found for a temperature rise to 200 K.

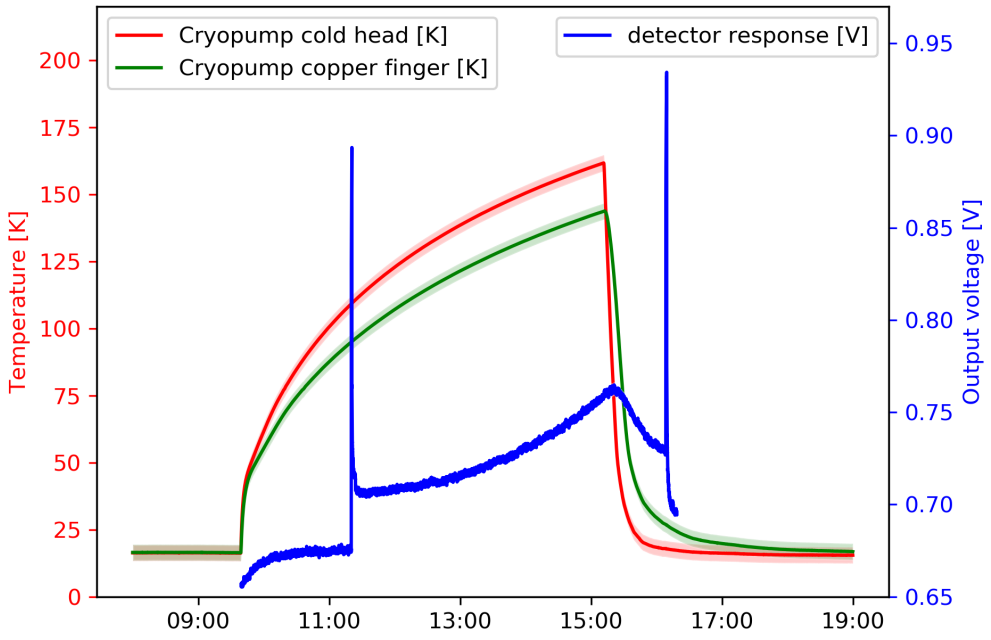

Figure 2.18: The cryogenic pump was switched off and the effect on the detection system was observed over time. The temperature uncertainty was assumed to be ±3 K as the temperature was monitored by a custom made monitoring system. An uncertainty of 0.1%+0.0002 V for the voltage measurement was assumed as described by the manual of the multimeter Uni-T UT61E.)

To reduce the infrared background radiation further, modifications on the detector system are necessary.

Implementation of a radiation shield surrounding the BIB detection system

To reduce further the flux of background IR-radiation onto the BIB detectors, a shield surrounding the mirror-system and the detectors was developed. A schematic drawing of the mounted shield is shown in fig. 2.19. It is coated on both sides in a graphite black to increase the absorption of the IR-radiation. The black coating consists of graphite and can be sprayed directly onto the object. After the evaporation of the solvents, the graphite coating is vacuum compatible. The reflectance of the coating varies between 10% and 20% in the spectral range of 2.5 to 20 μm [Mellouki, Bennaji, and Yacoubi 2007]. This reduces the reflected amount of light in comparison to metal surfaces. Stainless steel has varying reflectance between 10% to nearly 100% for 2.5 to 20 μm. The reflectance strongly depends on the wavelength and the roughness of the surface [Namba and Tsuwa 1980]. A polished metal surface reflects more photons than a metal surface with visible machining marks. To allow the ion beam to circulate in the trap, the surrounding cylinder has two 15 mm holes. The holes are extended by tubes inside the shield to 20 mm. This acts as long aperture reducing the solid angle and thus the flux of stray light.

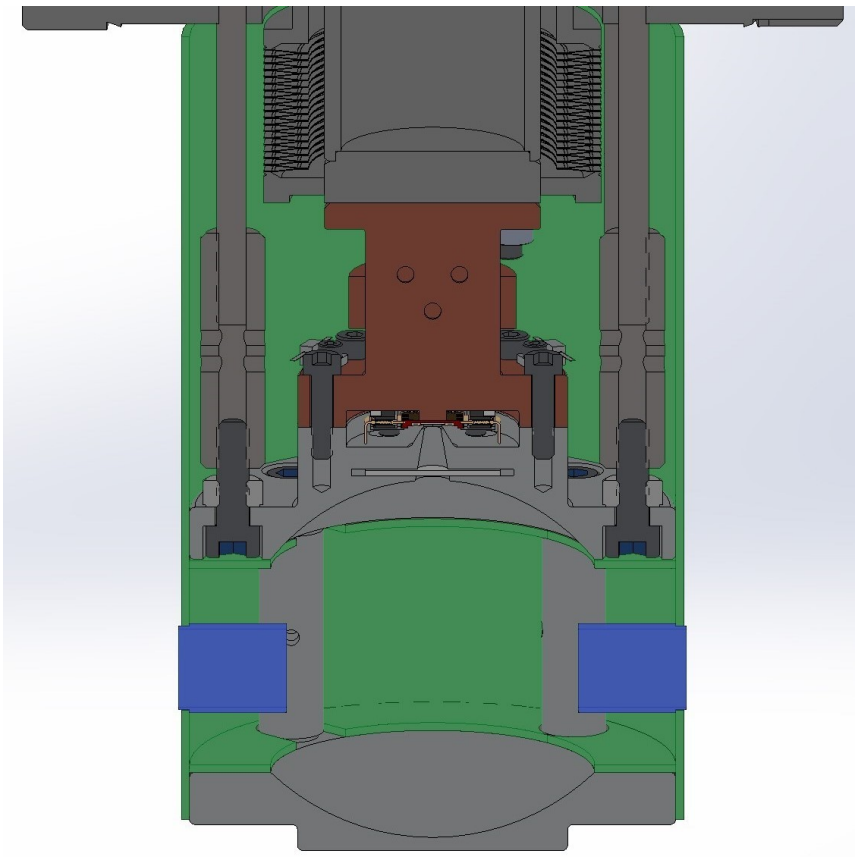

Figure 2.19: Schematic drawing of the shield surrounding the BIB detection system. The shieled is colored in green and the apertures for the ion beam are colored in blue.

During the first cryogenic test run of the implemented shield, a new amplifier system was used. The new amplifier has a higher output voltage of 15 V. This allows to amplify higher input currents until the saturation threshold of the amplifier is reached. After filling with liquid helium the temperature sensors in close proximity to the BIB detectors reach approximately 5 K. Each detector was tested without an ion beam to evaluate the IR background with the shield and the new amplifier. As a result bias voltages close to -2 V could be applied to all BIB detectors. The results are summarized in tab. 2.5.

Detector	Bias voltage	Output voltage
1	-1.8	10.0
2	-2.0	8.1
3	-2.0	8.0

Table 2.5: Applied bias voltages and measured output voltages of the latest detector test.

The latest test results seem promising. The level of IR-background radiation is strongly reduced. The bias voltage of the BIB-detectors could be decreased to -2 V without saturating the amplifier system. Further modifications have to be performed to test the limits of the detection system, as the multi-layer copper shield and the cryogenic modification on beam injection side are not coated in graphite black. This might further reduce the IR-background. For laser experiments, the multi-layer copper shield has to be modified further with a central aperture. This modification might increase the IR-background radiation, as it connects the BIB-detection system with a 300 K environment by a line of sight.

3 Decay Processes Of Anionic Dimer Systems

3.1 Motivation

In 2015, the newly commissioned CSR was introduced into the scientific community. To demonstrate the capabilities of the new storage ring, the non-thermal power law decay of anionic dimers was investigated. The state-of-the-art description of the physical process was based on experiments with a maximum storage time of 80 ms [Fedor et al. 2005]. Here, we extend these studies by more than four orders of magnitude up to 1000 s, enabling deep insight into the long term time evolution of such small systems. Dimers define the starting point of the transition between atoms and bulk material.

3.2 Experimental Details

Purely electrostatic storage devices are mass independent and can therefore store even large systems up to biomolecules. Cold, cryogenic environments allow infrared active particles to cool-down to their ro-vibrational ground state by interacting with the ambient photon field. The electrostatic Croygenic Storage Ring (CSR) in Heidelberg at the Max-Planck-Institut für Kernphysik combines these properties. The detailed information characterizing the CSR have been taken from [Hahn et al. 2016]. CSR has a circumference of 35 m and a four-fold symmetry. A beam storage lifetime of 2717±81 seconds for Ag_2^- was achieved, yielding a residual-gas particle density of less than 140 per cm^3 at a temperature of ∼5.5 K, which corresponds to a room temperature equivalent pressure of below 10^{-14} mbar. The schematics of the CSR, which is adopted from [Hahn et al. 2016], are shown in fig. 3.1.

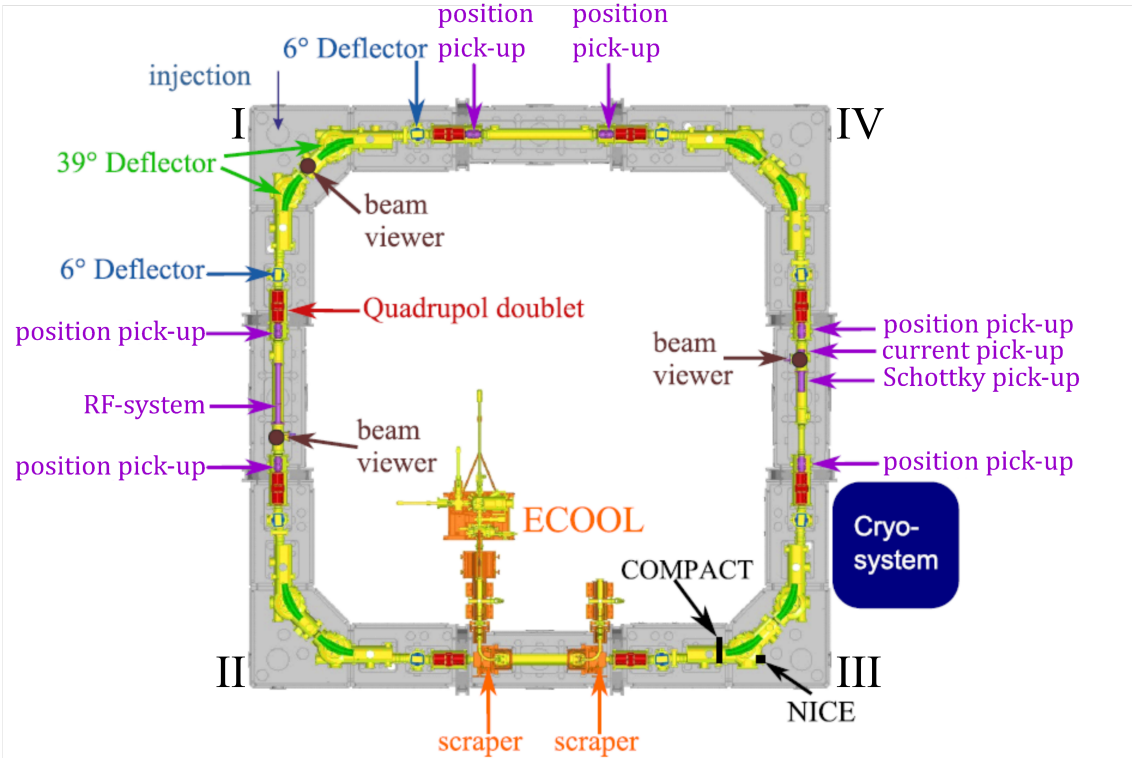

Figure 3.1: The CSR has a four-fold symmetry with two 39° and two 6° electrostatic deflectors in each corner. Four field free sections of 2.6 m length for experimental and diagnostic tools each connecting two corners are available. Between the injection part in corner one (I) and the second corner (II) the RF-System and the neutral beam line setup are placed. In the straight section between the second (II) and the third corner (III), the E-cool system as well as the laser setup are implemented. The following field free section between the third (III) and fourth corner (IV) houses the beam diagnostics system including the current pickup and the Schottky pickup. Between the fourth (IV) and the first corner (I) a reaction microscope will be implemented which is currently under construction. Two position pick-ups for beam position monitoring are included in each field free straight section except the one where the E-cool system is implemented.

To bend the ion trajectory by 90 degrees in each corner a set of four deflectors are utilized, two 6° and two 39° deflectors. Before and after each set of bending deflectors, a quadruple electrode doublet is placed to focus the ion beam. The field free section between the corners is used for experiments. Starting from the injection port, the first field free section is utilized for ion-neutral interaction experiments and radio frequency (RF) excitation of the ion beam. The second field free section holds the photocathode electron cooler system for ion-electron interaction and a laser mirror system for ion-photon interactions. The electron cooler can be used to perform phase-space cooling of the ion beam as well as serve as an electron target, depending

on the energy and mass of the examined particle. Section three contains the beam diagnostic tools, current pickup and Schottky-noise pickup. Additionally a reaction microscope is currently under construction, which will be implemented in the fourth section. CSR consists similar to the CTF of two vacuum systems. The isolation (outer) vacuum system reduces the thermal flux by diffusion onto the experimental vacuum chamber drastically. Furthermore, it reduces the leak rate of residual-gas particles into the experimental (inner) vacuum chamber by several orders of magnitude. The experimental vacuum chamber is wrapped in copper (Cu>99.95%) to increase the thermal conductivity of the chambers at cryogenic temperatures. Two thermal shields at 40 K and at 80 K, which are cooled actively, surround the experimental vacuum chamber. Each feedthrough is thermally anchored on the shields and thus a reduced thermal flux onto the experimental vacuum chamber is achieved. Blackbody radiation from the isolation vacuum chambers at room temperature is reduced by 30-40 layers of super insulation, wrapped around the 80 K shield. For the experimental vacuum chambers, 20 W at 2 K cooling-power is available. For the cryogenic shields a cooling power of 600 W is available. To reduce stress on the experimental vacuum system a mean thermal gradient of ∼0.6 k/h over ∼20 days is used for cooling down and heating up CSR. To minimize the mechanical stress from the thermal expansion coefficient, bellows are frequently mounted between parts of the experimental vacuum system. The beam guiding elements are kept in place on thermally decoupled room-temperature supports. Thus a precise alignment is guaranteed over all temperature regions. The ions are produced on two high-voltage platforms with up to 300 keV/q and 60 keV/q kinetic energy respectively. For anionic dimer production, a Middelton Ion Sputter Source (MISS) was employed. For details see fig. 3.2.

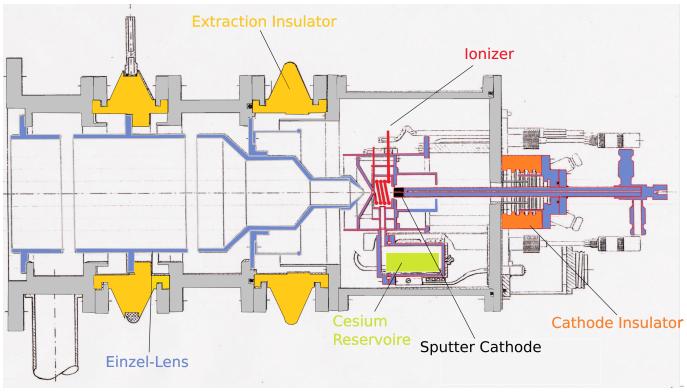

Figure 3.2: Schematic drawing of a Middelton-Ion-Sputter-Source (MISS) which was adapted from [Blaum]. It was utilized to produce anionic dimer clusters.

Here, the production medium is the alkaline metal cesium. It is evaporated in a cesium oven, which already partially ionizes the vapor. The thermally ionized cesium ions are accelerated towards the target in the center of the source. Bombarding the target with cesium ions produces a variety of fragments escaping the surface

of the target. The fragments interact with the cesium vapor, which might lead to electron attachment to the fragments. Due to the attraction of the positive ions by the negatively floated target, only negative ions are extracted from the source. The hot mixture of fragment ions is then mass-selected by electro-magnets and guided to the storage ring.
At CSR two detection principles were available. Non-destructive image charge detection and Micro-Channel Plate (MCP) based detection systems. The mirror charge effect induces a detectable signal in the pick-up electrodes. Depending on the connected electronics and the electrode shape, various information about the ion beam can be obtained. For the following experiments, two MCP based detectors were employed which detected the daughter fragments from the ion beam. The Neutral Imaging in Cold Environment (NICE) detector, which consists of a double stack MCP set with a diameter of 120 mm and a phospor screen anode [Becker 2016; Hahn et al. 2016] is placed in corner three in forward direction of the field-free section beforehand. Its main purpose is the detection of neutral fragments exiting the ion beam. As second detector, the COld Movable PArticle Counter (COMPACT), is available for measurements [Spruck et al. 2015]. It is constructed to be movable in the cryogenic vacuum to adapt for the beam position of charged daughter fragments. Fig. 3.3 shows an overview of the linear section utilized for the experiment.

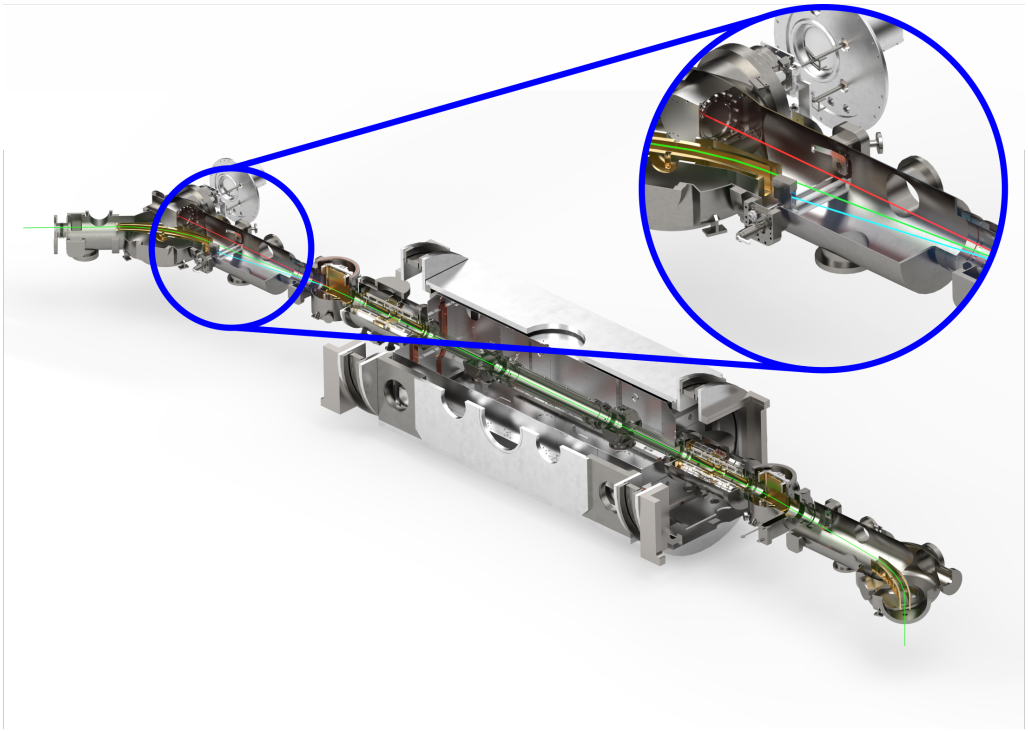

Figure 3.3: Cut through the E-cool section of CSR. The green colored line indicates the stored ion beam, whereas the red line symbolizes the neutral fragments. The cyan line demonstrates the detection position for the charged fragments.

In case of COMPACT, a plate in front of the MCP stack converts impacting particles into electrons, which are accelerated towards the MCP front plate. The amplified electron current is collected on a sheet metal anode for counting [Hahn et al. 2016]. Depending on the measurement scheme either COMPACT or both detectors (NICE and COMPACT) are used.

3.3 Data acquisition

The data acquisition system is based on a Field-Programmable Gate Array (FPGA) card. A LabView progamm interface controls the data acquisition system and stores all data. The program defines the storage time and beam-off period for each measurement cycle, as well the start and stop of the measurement. The measurement cycle for one injection shown in fig. 3.4 is started by a trigger which requests the injection of ions into the storage ring (injection request trigger). This trigger is synchronized and phase-locked to the 50 Hz sinusoidal modulation of the mains voltage. The synchronization and phase-locking reduces the voltage fluctuations of the high-voltage platforms. Therefore, the beam energy is stabilized and the beam position between injections is less fluctuating. From the synchronized trigger, an Atmega-Clock generates various triggers. One of these triggers opens the chopper and another one confirms the injection (injection confirmation trigger). The injection confirmation trigger starts the data acquisition and defines the zero time. The chopper trigger controls a deflector unit (chopper) which is placed in the beamline from the ion sources to the CSR. To inject ions for storage in the CSR, the deflector unit is grounded by the low state of the chopper trigger. Additionally the first 6°-deflector of the CSR in corner 1 is grounded by a trigger derived from the chopper signal. The continuous ion beam can enter the CSR. The time period for which the chopper unit is grounded defines the ion bunch length injected into the CSR. To successfully store ions, the 6°-deflector is switched to high-voltage before the ion bunch completes a full orbit in the CSR. To measure the dark count rate during the beam off period, the ion beam is stopped by grounding the first 6°-deflector in corner one. The stored ions decay randomly and produce daughter fragments which can be detected in corner three. The data acquisition started ∼10 ms before the first fragments from the decays arrived at the detectors. Upon impact of the fragments the MCP based detectors (COMPACT and NICE) produce an electron avalanche towards an anode (COMPACT) or Phosphor screen (NICE). For COMPACT, the resulting negative pulse is amplified by a factor of 200 and electronically discriminated before the signal is fed in the digitizer card (Keysight U1084A digitizer). The discriminator values are chosen as defined in the previous work of Spruck and coworkers for maximum pulse yield [Spruck et al. 2015]. The threshold was set to 10 V for the discriminator. For NICE, the pulse signal is amplified and fed into the same digitizer card. For both detectors a pulse height is stored in the file. Therefore, the waveform is pre-sampled and the local maximum within a time window of 50 ns is acquired. The signals from the MCP based detectors are counted by the FPGA

card. To cope with the amount of data, a circular dual memory bank system is used. During data acquisition, the system switches between both banks with period of ∼33 ms at a sampling time of 1 ns. Under high data load the subsequent writing of the data to a storage machine may take more time than ∼33 ms. Therefore a dynamic dead time between the banks can be observed (see fig. 3.4 data acquisition). It varies between 10 μ s and a few ms. Each step of ∼33 ms is written to the measurement file with its start time. Within this step events are recognized with their pulse height, detector channel and time in dependence to the starting time of the step. The timing of each event is the sum of the start time of the step and the time of the event within the step.

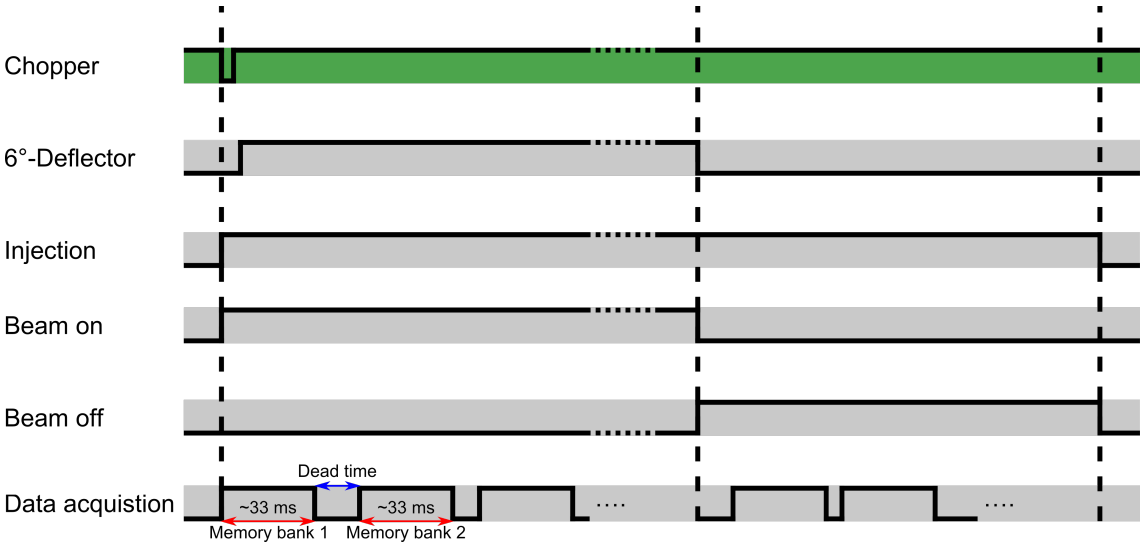

Figure 3.4: Measurement cycle for one injection.

3.4 Data analysis

The measurements were taken during the first cryogenic beam-time in 2015, as well as in 2017. Continuous measurements define certain requirements on the stability of the detection system and on the environment. Pressure and temperature fluctuations might introduce changes in the count rate by collisional events. A close environmental surveillance and a stable storage ring is essential. Long-term stability of the measurement requires stable oscillators e.g. clocks. Here a 100 MHz precision clock was utilized controlling the timing of the data acquisition system. Noise bursts introduce fluctuation in the count rates which might interfere with the observation of a physical process. High count rates might deplete the MCPs. Time-of-flight measurements without lasers have no previously known starting point, which requires further steps of analysis. To clean the data from noise and correct for dead time of the data acquisition system, several steps have been performed. In contrast to

measurements with pulsed events and low count rates on the detectors which were performed to measure the photo-electron detachment of OH^-[Meyer et al. 2017] and the photo-fragmentation of CH^+[O'Connor et al. 2016]. Here a triggered data acquisition limited the effect of noise on the data. Furthermore, the noise is reduced by coincidence measurements on both detectors with a pulsed laser. The particles time-of-flight and the time-frame when the laser interacts with the ion beam is known exactly. Additionally, for low count rates, no depletion effect on the detection efficiency of cold MCPs is expected.

3.4.1 Ion bunches

Ion beams have a momentum spread. For chopped ion beams the momentum spread can be defined as the time which is needed to equally distribute the particles within the beamline due to dispersion. The cycling ion bunch introduces a pulsed signal scheme in the early storage phase on the MCP based detectors, which diminishes as over time the bunch disperses in the CSR. This signal, as shown in fig. 3.5, can be used to determine the time when the ring is completely filled after ∼30 ms. Additionally the signal provides information about the depletion status of the MCP, as the count rate changes per cycle. The count rate is influenced by the beam position, the number of particles in the ring and the fragmentation process. Saturation can occur when a high number of particles hit the detector. At room temperature, an MCP can tolerate rates in the order of $10^6 \frac{\text{particles}}{\text{s}}$ [Wiza 1979]. Cooling down to cryogenic temperatures increases the internal resistance of the MCPs and thus limits the charge diffusion, which reduces the saturation threshold. A balanced heating of the system decreases the resistance and allows higher rates, while keeping the temperatures in the storage ring stable. At a temperature of ∼30 K the MCP of COMPACT can tolerate rates of up to 10000 s^{-1}. The larger MCP of NICE saturates at a rate of ∼700 s^{-1} at a temperature of ∼20 K [Becker 2016]. A constant count-level for each bunch would indicate a saturated detector, as the number of particles should decrease over time if a decay process is to be observed. Here the MCP is limited by the recharging. During the digitization time-window of 15 ns only two very close events would appear as one event. A re-triggering, i.e. the prolongation of an event by a second event, is not possible on the readout side. If the count-level decreases within an ion bunch beyond the expected process and the statistical uncertainty, saturation can also be inferred. This type of saturation can be explained by a cycling process. Here the detector is irradiated by high number of particles on a wide area. The local charges are depleted and further particle detection is impossible within the time period of an ion bunch. Until the next cycle, a partial recharging of the MCP might be possible and a count rate is observed until the charges are again depleted. This cycle continues until the particle rate from the ion bunch matches the recharging rate of the MCP. The modifications from saturation influences the observed decay strongly as the particle count rate is underestimated and thus the slope of the decay is modified. In fig. 3.5, the time modulated count signal is demonstrated integrating over all injections, with an oscillating event-rate expected to be

arising from the beam oscillation within the CSR. After data evaluation the first 30 ms were removed. For each measurement file the state of the MCP was examined.

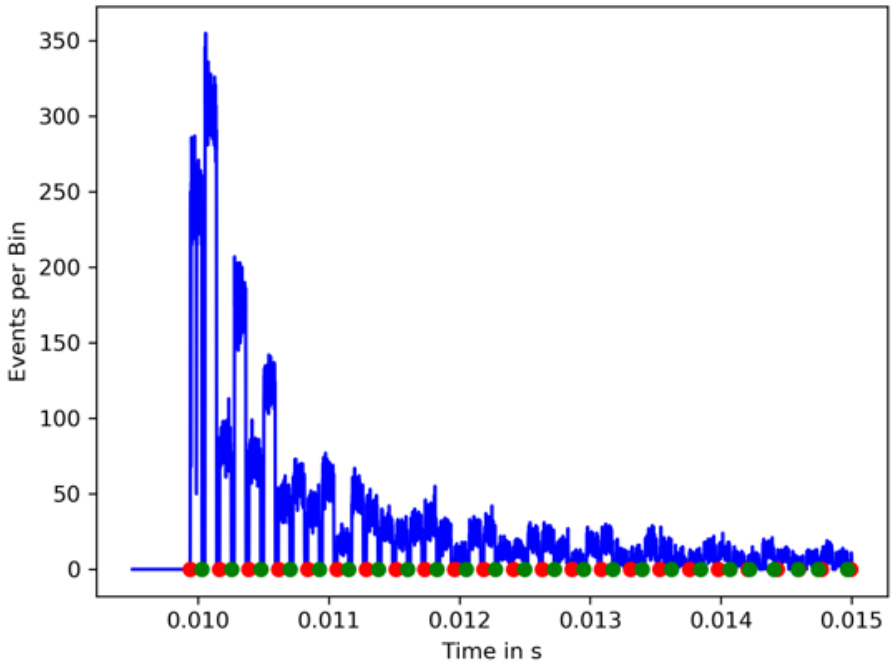

Figure 3.5: The plot shows particle counts on COMPACT versus time with a bin-size of 1 μ s for the first 15 ms.

3.4.2 Pulse height distribution

The digitizer card records not the full waveform, but a defined maximum pulse-height. To reduce the number of noise pulses, a threshold of -0.056 V is applied by the digitizer card. A large number of noise events would lead to longer gaps between the steps, if the recording and emptying of the memory bank takes longer than ∼33 ms. Fig. 3.6 demonstrates the pulse-height distribution of COMPACT for a measurement file acquired from an anionic silver dimer beam. The recharging pulses of the MCPs produce only negative pulse heights in the used configuration. Positive pulses which might appear were removed by the data analysis. A possible explanation for the positive pulses is a strong radio-frequency source which appears randomly and interferes with the data acquisition system after the digitization of the pluses. COMPACT, due to its size, is suited for high count rates with a relative low dark count rate where as NICE is more suited for low count rates with high precision as the pulses are more sharp. Segmenting the measurement time in smaller time windows where the pulse height distribution is examined might reveal saturation of the MCPs. The slope of the pulse height distribution changes strongly when saturation is observed. For the MCP of NICE the pulse heights are shifted to lower amplitudes with a maximum close to -0.4 V [Becker 2016]. For the MCP of

COMPACT a similar shift is expected. The usage of the time development of the pulse-height distribution is of limited use in power law decays. As the decay slope is not exactly known, the managing of statistics is difficult. For a precise time-dependent evaluation of the pulse height distribution, each window should contain a similar number of events which is a time consuming iterative process. The integrative method mentioned in chap. 3.4.1 was found to be more time effective.

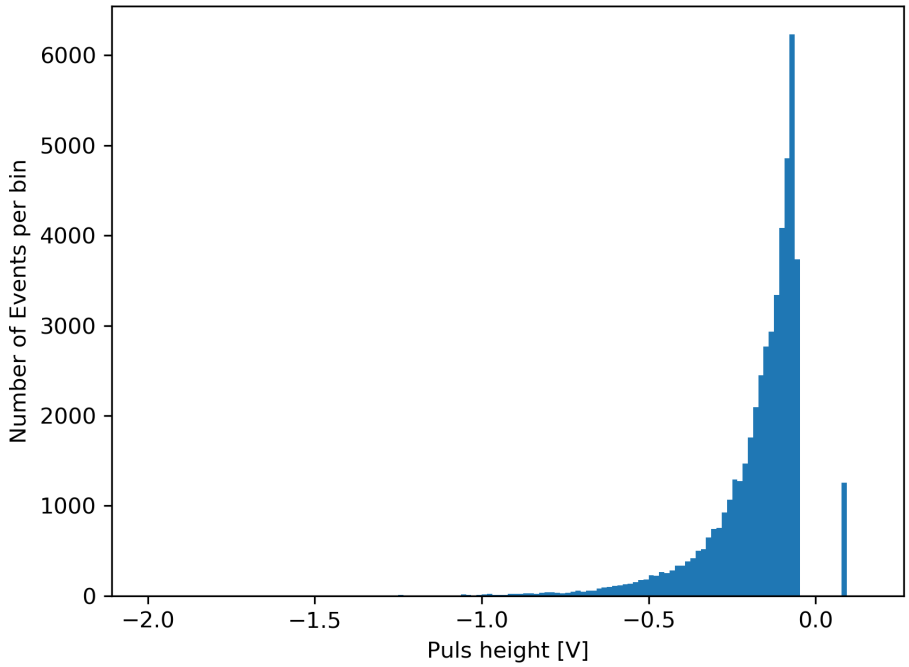

Figure 3.6: Pulse-height distribution of COMPACT for an anionic silver dimer measurement of 15 s. A single positive pulse bin at ∼0.092 V is visible.

3.4.3 Memory bank gaps

As stated in the chap. 3.3, two memory banks were available. The switching between the two memory banks introduced gaps in the measurement file. Writing of the data from the memory bank into a step consumes time which depends on the number of events acquired by the memory bank. The length of the gaps are not precisely repeated, as the number of events fluctuates between injections. To detect the gaps between the steps, each injection was scanned with a resolution of 1 μ s for the timing of each step. The gaps are visible as deep gaps in the sum over all injections for these scans. The sum of all injections for file Co_2^-0057 is shown in fig. 3.7 where the blue line corresponds to the sum of steps per 1 μ s. The red crosses indicate the left edge of the logarithmic bins which are required for the data analysis. The correlation between the position of the logarithmic bins and the gaps in the data acquisition is visible. In fig. 3.7, some red crosses fall into regions with a gap in the number of active steps. This modifies the local number of events, leading to false

rates. A procedure was developed as described in the chap. 3.4.5 to counteract the modified rate.

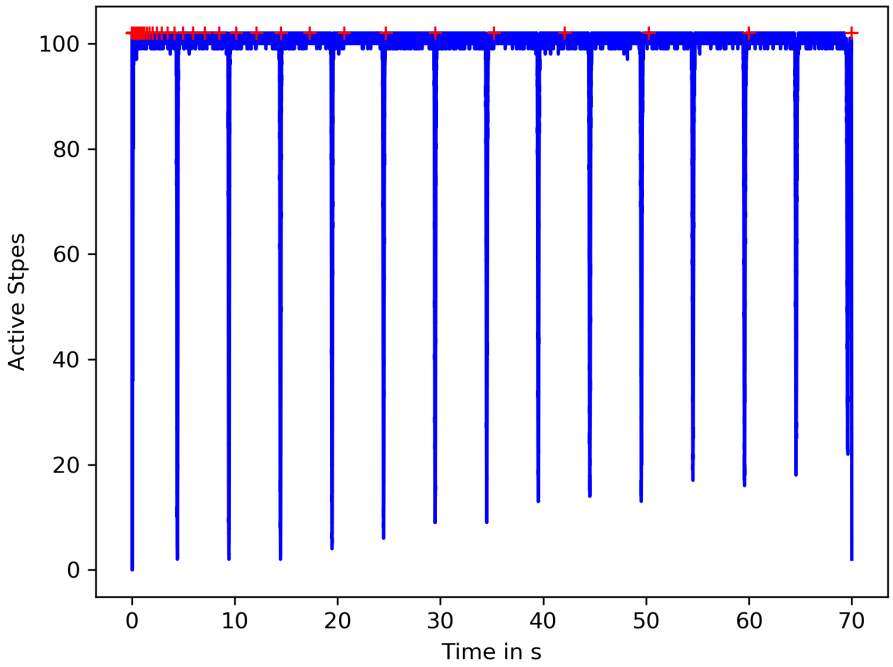

Figure 3.7: The blue line indicates the active steps, superimposed with the position of 50 logarithmic bins visualized as red crosses.

3.4.4 Coincidence

Coincidence methods require at least two independent detectors. A physical process which produces at least two particles like fragmentation might trigger either none, one or both of these detectors. The ratio of the event classes (none, one or both) strongly depends on the geometry of the setup and the detector efficiency. Particles might not activate one or both detectors, have a flight trajectory which bypasses one or both detectors or are captured by a surface. The time between two events triggering both detectors depends on the physical distance between the detectors. For ions measured in a storage device, the momentum spread of the ion beam introduces a distribution for the coincidence time. The width of this time distribution corresponds to a time window. This time window can be implemented in a detection system as e.g. a gate-generator, or after data acquisition as software filter. The coincidence method reduces the background rate R_{Random} depending on the length of the time-window δt and the single rate of both detectors (R_1, R_2), as only events within the time window are counted [Eland 1996].

$$R_{Random} = R_1 R_2 \delta t \tag{3.1}$$

This method can be used to resolve low count rates below the uncorrelated background. Here the method was applied to find and remove correlated noise as well as for the fragmentation process with two daughter fragments.

Noise

We observed a type of noise which appears as correlated noise on both detection systems. It might be introduced by radio waves of various sources. The cables and the electronics act as antennas for the radio waves, which are then digitized and stored in the data stream. It was first detected in the beam-off period, when no ions are stored and the dark count rates of the detection systems are well known. During the beam-off period an average rate of $\sim 0.1\ s^{-1}$ is expected for COMPACT [Becker 2016]. For NICE, the average rate during the beam-off period increases to several $10\ s^{-1}$. Noise appears as high-intensity steps within an injection. Consecutive steps with high intensities within one injection are noise trains. Fig. 3.8 shows the noise pattern during the beam-off period for one file of Co_2^-. The colors from blue to green indicate the number of events per step per injection, ranging from one to twenty events. It is safe to assume that during the beam-on period the same noise structure is superimposed on the signal of the be observed process as the noise appears randomly. Therefore it is important to filter the noise and the noise trains out.

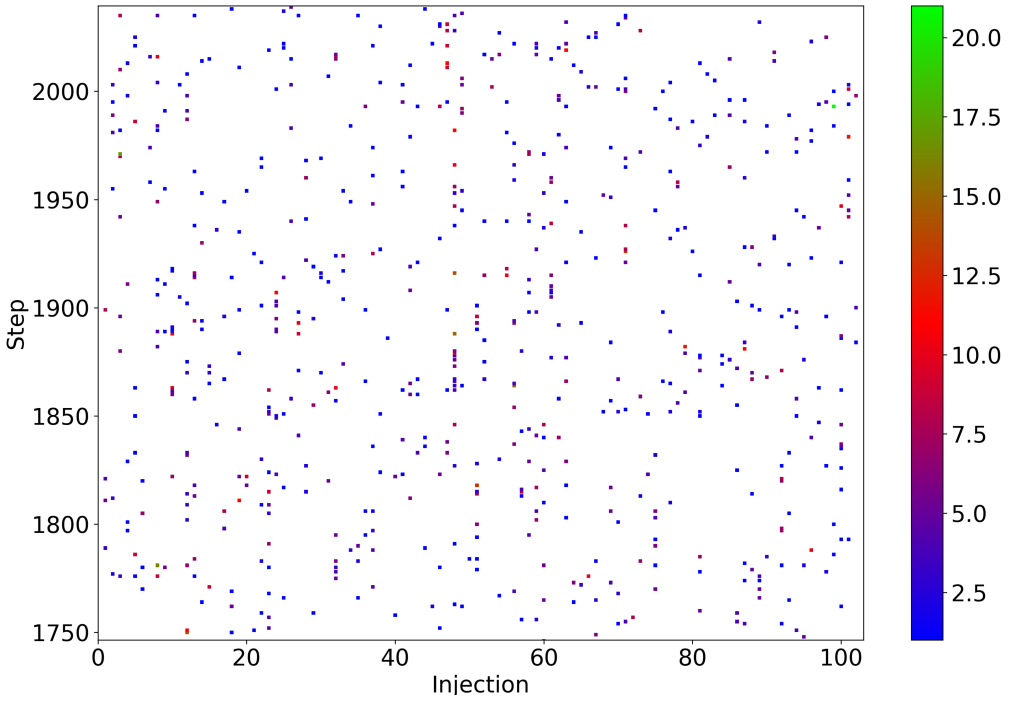

Figure 3.8: The two dimensional plot shows events per bin versus injection for an measurement of an anionic cobalt dimer during the beam off period. The intensity per step is color-coded.

The correlated noise which appears during the measurements is removed by a software filter. In general the coincidence time between two noise events is below 500 ns as shown in fig. 3.9. The coincidence method removes events for which the absolute time value between an event on COMPACT and an event on NICE is less than 500 ns. For the anionic cobalt dimer with mass 118 amu, the measured coincidence time for an energy of 60 keV was around 1364 ns. It was the lightest anionic dimer measured in coincidence mode. Heavier particles which were measured at the same energy require more time to arrive at the second detector. From this follows that the threshold of 500 ns to remove noise events is well below the coincidence time of the examined fragmenting particles.

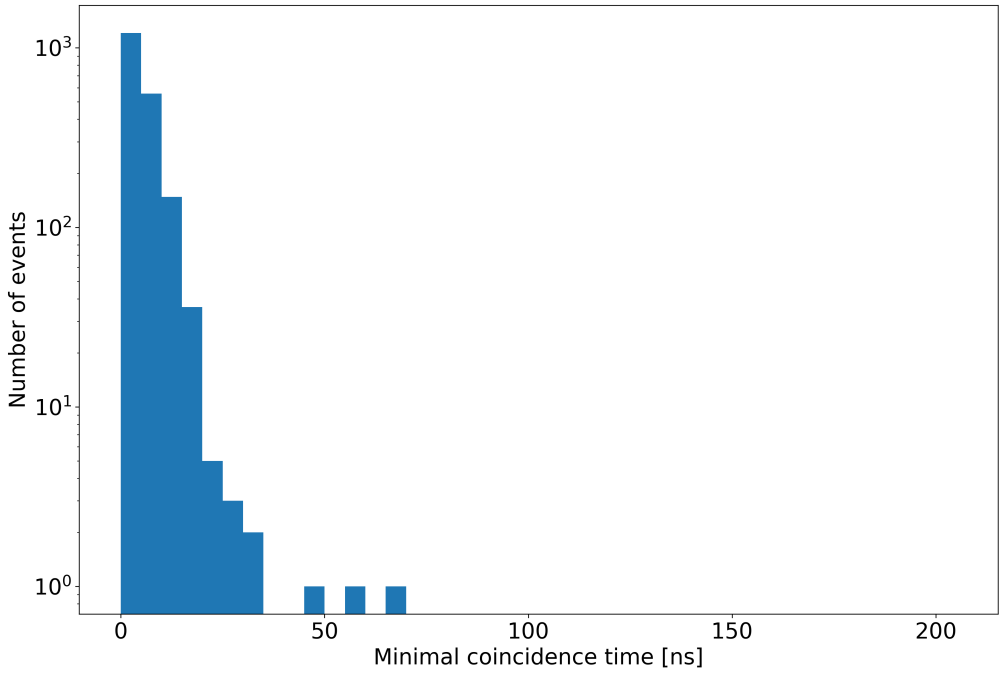

Figure 3.9: Coincidence time between two noise events on both detector channels for an anionic cobalt dimer during the beam-off period. All positive puls-heights have been removed. The absolute minimal time difference between two events is displayed on the time axis.

After removing the noise from the measurement by the coincidence method, the pattern for the dark count rate was randomly distributed as demonstrated in fig. 3.10. The average dark count rate for the 10 s beam-off period of the demonstration file reduced from $\sim 2.2 s^{-1}$ to $\sim 0.28\ s^{-1}$. The coincidence filter was then applied to the whole measurement with the defined maximum coincidence time for noise events.

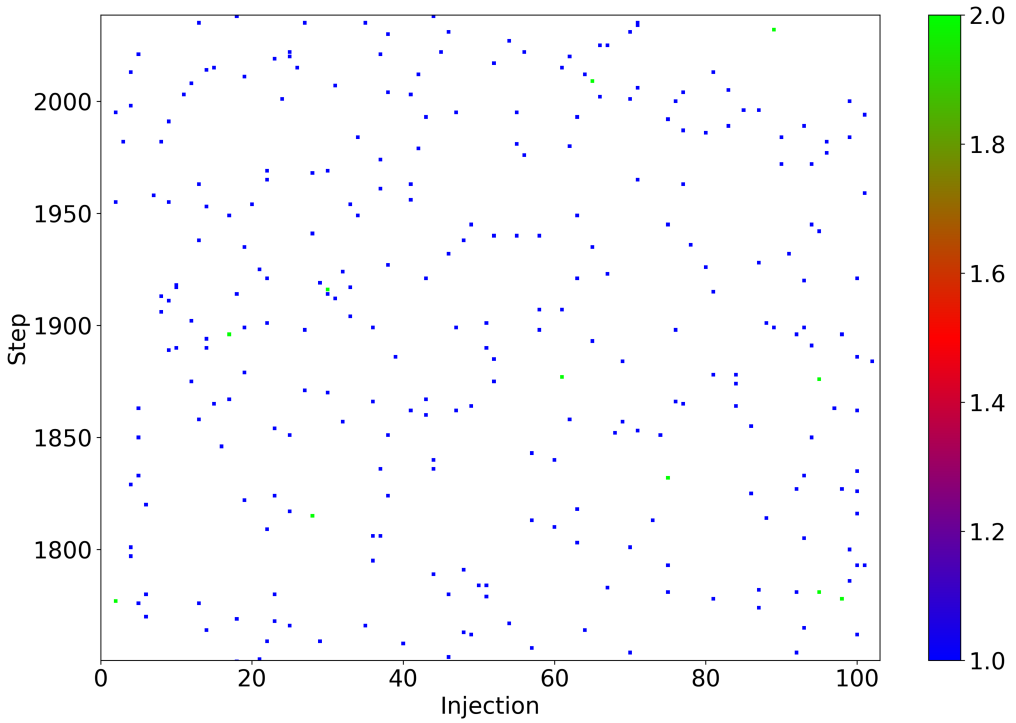

Figure 3.10: Same as fig. 3.8, but this time the coincidence noise filter has been applied.

Coincidence filter

For coincidence measurements data, was continuously taken from both active detection systems. To filter the real events on both detectors, the same principle as for the coincidence noise filtering was applied. The algorithm was modified for the particles impinging first on COMPACT and then on NICE. Only positive time differences are relevant for the coincidence measurement. The coincidence time range was larger than in the previous noise filtering process, as the particle travels with less than 0.5% of the speed of light. The coincident events were stored in a file. Hence no hardware gate was used, the evaluation was flexible and the time window for coincidence was evaluated within the measurement. Fig. 3.11 demonstrates a coincidence time distribution for both detectors. It shows the number of events versus the minimal coincidence time, which is the minimal time between two events. The coincidence peak was fitted with a Gaussian distribution and the Full-Width-Half-Maximum (FWHM) was taken as coincidence window. Each measurement was evaluated for its own coincidence time. The coincidence time window depends on the particles mass and the kinetic energy.

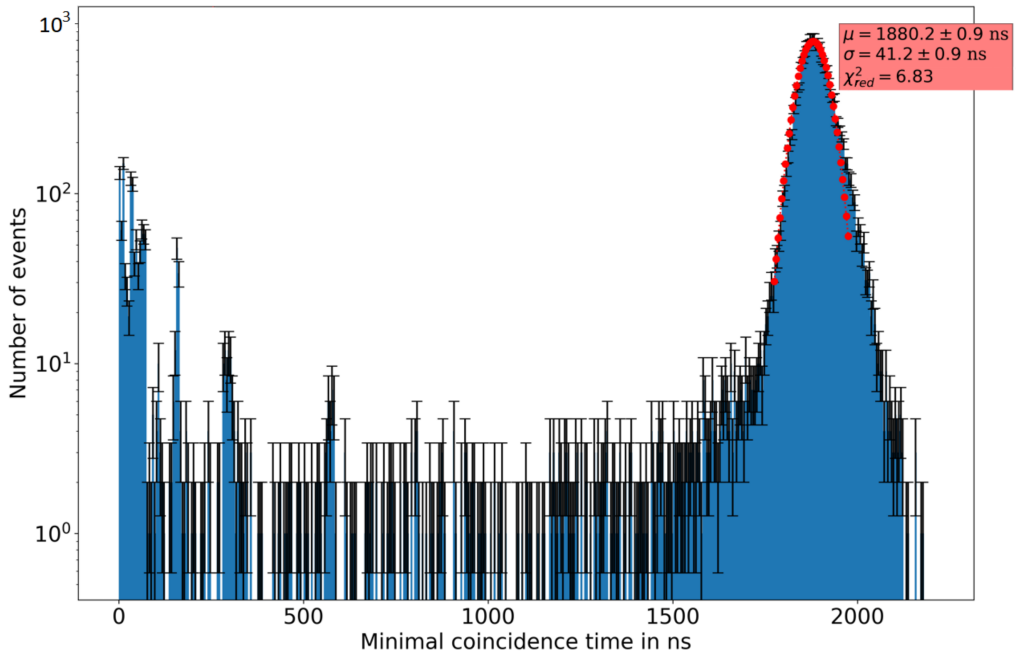

Figure 3.11: Time-of-flight spectrum for a coincidence measurement of anionic silver dimers. Events on COMPACT and NICE below 2.2μ s minimal coincidence time are shown. The events on COMPACT are used as timing reference. The peak is fitted with a Gaussian distribution (red dots). It yields the coincidence time as the mean with the standard deviation as uncertainty.

3.4.5 Corrective weighting

To fit the experimental data, a continuous binning is required. For the acquired measurements, a logarithmic binning was chosen. This should result in an even distribution events per bin for a perfect 1/t power law decay. The rate observed for this power law is inverse proportional to the time $R(t) \propto t^{-1}$. By superimposing the chosen binning with the experimental data, the mentioned gaps between the steps modify the resulting particle count rate. A rate R can be defined as an average number of events E per time window δt:

$$R = \frac{E}{\delta t}. \tag{3.2}$$

Keeping the number of events E constant, but increasing the length of the time window δt corresponds to a reduced rate R'. For binned data, the length of the bin defines the time window for the rate calculation. Due to the gaps within the logarithmic bins, the time window for the rate calculation is overestimated. A normalization can counteract the reduced count rate as it corrects for the gaps. Additionally, a relative injection strength has to be included into the normalization, to compensate for the varying beam intensity. Fig. 3.12 shows the filtered experimental data of a file with 200 logarithmic bins over a period of 70 s. The gaps are visible as intrusions

in the number of events per bin. Similar plots as fig. 3.12 were generated of each file with varying bin numbers. This demonstrated that increasing the number of bins deepens the intrusions. For smaller bins the effect of the gaps increases as the bins sample less time. To apply Gaussian statistics for normalization, at least 20 events per bin for all injections are required. This results in a counting uncertainty of $\sqrt{N}$. The binning of the experimental data is chosen such that the limit of 20 events per bin is not violated. For this purpose, the mentioned plots for each file similar to fig. 3.12 were evaluated.

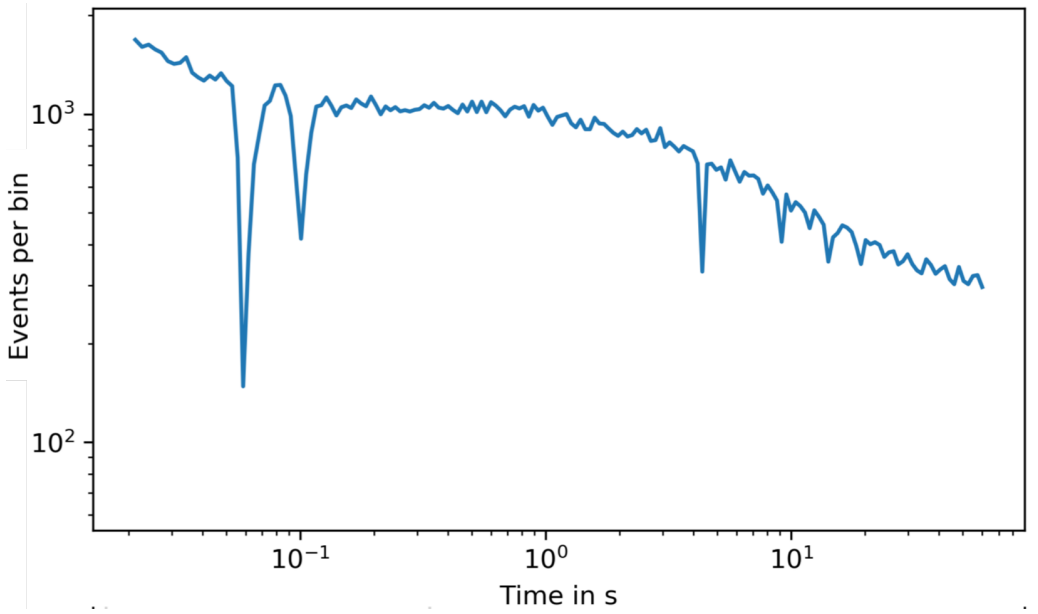

Figure 3.12: Particle events per bin versus storage time. The binnings along the x- and y-axis are logarithmic.

The procedure for normalizing the data is described in the following. The acquired and filtered particle events per time bin for all injections $\sum_{Inj} N_{\mathrm{Inj,Bin}}$ were normalized to the sum of the fraction of measured time $T_{\mathrm{Inj,Bin}}$ during the defined bin length T_{Bin}. Additionally, the intensity of the ion-beam was relatively weighted. As a stable reference, the second data step is used ($\sim$ 33 ms to $\sim$ 66 ms). In the second data step the ion bunches are already dispersed within the CSR and no intensity dependent shift of the data step is observed. For each injection the number of events within this step is summed as $N_{\mathrm{Inj}}^{\mathrm{Ref}}$. The mean value of these sums is described as $N_{\mathrm{Mean}}^{\mathrm{Ref}}$. The fraction of $N_{\mathrm{Inj}}^{\mathrm{Ref}}$ over $N_{\mathrm{Mean}}^{\mathrm{Ref}}$ corresponds to the relative injection strength. Formula (3.3) shows the normalization:

$$N_{\mathrm{Norm,Bin}} = \frac{\sum_{Inj} N_{\mathrm{Inj,Bin}}}{\sum_{\mathrm{Inj}} \frac{T_{\mathrm{Inj,Bin}} N_{\mathrm{Inj}}^{\mathrm{Ref}}}{T_{\mathrm{Bin}} N_{\mathrm{Mean}}^{\mathrm{Ref}}}} I. \tag{3.3}$$

The derived correction is to be multiplied by the number of injections I to yield the integrated number of events per logarithmic bin. For both variables $N_{\mathrm{Inj}}^{\mathrm{Ref}}$ and

$\sum_{Inj} N_{\mathrm{Inj,Bin}}$, the classical counting uncertainty of $\sqrt{N}$ is assumed. The uncertainties are Gaussian propagated. The equations (3.4) and (3.5) are partial derivatives of eqn. (3.3) with respect to $\sum_{Inj} N_{\mathrm{Inj,Bin}}$ (eqn. 3.4) and to $N_{\mathrm{Inj}}^{\mathrm{Ref}}$ (eqn. 3.5):

$$\Delta_1 = \left(\frac{\sqrt{\sum_{\mathrm{Inj}} N_{\mathrm{Inj,Bin}}}}{\sum_{\mathrm{Inj}} \frac{T_{\mathrm{Inj,Bin}}}{T_{\mathrm{Bin}}} \frac{N_{\mathrm{Inj}}^{\mathrm{Ref}}}{N_{\mathrm{Mean}}^{\mathrm{Ref}}}} \right) I, \tag{3.4}$$

$$\Delta_2 = \left(\frac{\sum_{\mathrm{Inj}} N_{\mathrm{Inj,Bin}} \sqrt{\sum_{\mathrm{Inj}} \left(\sqrt{N_{\mathrm{Inj}}^{\mathrm{Ref}}} T_{\mathrm{Inj,Bin}} \right)^2}}{\frac{1}{T_{\mathrm{Bin}} N_{\mathrm{Mean}}^{\mathrm{Ref}}} \sum_{Inj} \left(N_{\mathrm{Inj}}^{\mathrm{Ref}} T_{\mathrm{Inj,Bin}} \right)^2} \right) I. \tag{3.5}$$

Under the assumption of a power law decay $R(t) \propto t^{-a}; a > 0$ the gap position within a logarithmic bin might affect the normalization accuracy. Here the rapid change of rate might play a role. The integrated number of events within a logarithmic bin changes drastically close to the start of the bin, and slowly to the end of the bin. The plot in fig. 3.13 shows the percentage of events within the first half of a logarithmic bin for several power laws for example. The exponents range from 0.1 to 5. The bin starts at a value of two and ends at a value of four.

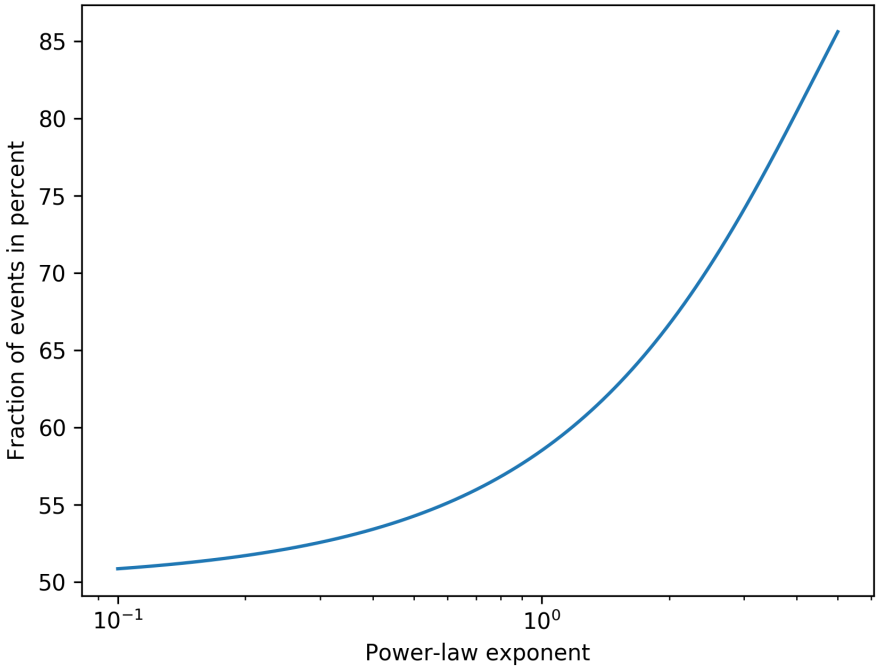

Figure 3.13: Percentage of events within the first half of a logarithmic bin with the length of two which starts at a value of two.

To evaluate the effect of the asymmetric distribution within the logarithmic bins on each file, a method was developed. The injection strength variation was modeled

by a random Gaussian distribution with a maximum height and a sigma of 10% of the maximum height. The number of sampled injections corresponded to the number of injections in the particular file. The decay was modeled by power laws with exponents ranging from 0.5 to 2 and the generated injection samples as starting values. The height of the random Gaussian distribution was adapted such that at least 20 events per bin were generated. From the previous scan of the acquired data from the experiment the position of the gaps in each file for each injection are known. This information is folded with the generated model decay curves and yields similar gaps as previously observed in the data from the experiment. The normalization is applied to the folded data, and the result is compared with the model decay curves. Fig. 3.14 shows the comparison between the model decay curve and the normalized folded data for a power law with the exponent $a = 0.5$.

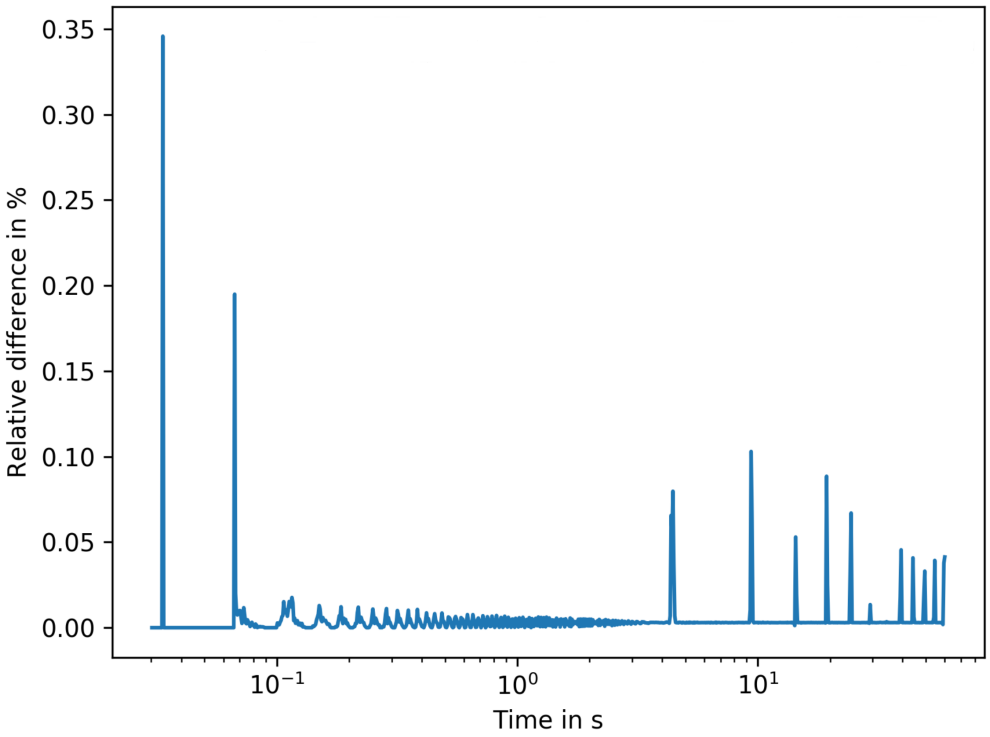

Figure 3.14: Comparison between model decay curve and normalized data-folded model decay curve. The deviation is shown as percentage of the exact model. Here the model decay curve corresponds to $R(t) \propto t^{-0.5}$.

The evaluation found a maximal additional uncertainty of 4% on the counted events$N_{\text{Inj,Bin}}$ (see eqn. 3.6):

$$\Delta_3 = 0.04 \sum_{Inj} N_{\text{Inj,Bin}}. \tag{3.6}$$

Adding quadratic the uncertainties:$\Delta N_{\text{Norm,Bin}} = \sqrt{\Delta_1^2 + \Delta_2^2 + \Delta_3^2}$ yielded the observed uncertainty within the decay plots by dividing the uncertainty by the length

of the bin to result in a rate.

3.5 Theory

Anionic dimers can spontaneously decay either by electron detachment (eqn. 3.7) or by autofragmentation (eqn. 3.8) [E. K. Anderson et al. 2020]:

$$X_2^- \rightarrow X_2 + e^- \tag{3.7}$$

$$X_2^- \rightarrow X + X^-. \tag{3.8}$$

For Electron detachment, the potential curves of the neutral dimer and the anionic dimer must overlap. Additionally the vibrational excitation must exceed the required energy to detach the electron. It was found for the anionic silver dimer that electron detachment is limited to rotational states below L = 250 and vibrational states above $\nu = 75$ [E. K. Anderson et al. 2020]. Autofragmentation requires highly excited ro-vibrational states. The rotational excitation modifies the ground-state potential with a rotational barrier [Fedor et al. 2005]. Vibrational states behind the barrier, which have been populated, can decay by tunneling. The decay follows an exponential function with a state dependent lifetime[Fedor et al. 2005]. The lifetime of such states varies greatly. For example the paper [R. J. Le Roy 2017] demonstrates a variation of the lifetime, for these states, between a few 100 ps and $\sim$ 300 years. The observed decay curve is the sum over all independent exponential decay channels. Here the amplitude, i.e. the occupation of states, modifies the shape of the observed decay curve. Former experiments on short time scales assumed a merely equal distribution of states which resulted in a 1/t power law which fitted their results [Fedor et al. 2005].

Potentials

As potential for the dimer ground state, a Morse-potential [Demtröder 2018] was assumed [Fedor et al. 2005]. To accommodate for angular momentum excitations of the ground-state, the Morse-potential (eqn. 3.9) was modified with an additional term to eqn. (3.10). It provides the potential with an angular momentum barrier depending on the total angular momentum l excitation [Fedor et al. 2005]:

$$V_{\text{eff}}(r) = D_{\text{e}}\left(1 - e^{a(r-r_{\text{e}})}\right)^2 \tag{3.9}$$

$$V_{\text{eff}}(r) = \frac{l(l+1)\hbar^2}{2q\mu r^2} + D_{\text{e}}\left(1 - e^{a(r-r_{\text{e}})}\right)^2. \tag{3.10}$$

To describe the Morse-potential, three variables have to be known: the Depth of the potential D_{e}, which corresponds to the binding energy of the dimer in the ground

state, the equilibrium distance of the atoms in the ground state r_e and the value of a, which modifies the width of the potential. The constant a can be determined by the relation $\omega_0 = a\sqrt{\frac{D_e}{\mu}}$ [Demtröder 2018], where the ground state frequency ω_0 and the reduced mass for two particles $\mu = \frac{m_A m_B}{m_A + m_B}$ have to be known. To express all energies in eV, the elementary charge q is introduced in the term for rotational excitation. For the pure Morse-potential the Schrödinger equation has an analytical solution [Demtröder 2018] and reads as:

$$E_{\text{vib}}(\nu) = \hbar\omega_0 \left(\nu + \frac{1}{2}\right) - \frac{\hbar^2\omega_0^2}{4D_e}\left(\nu + \frac{1}{2}\right)^2. \tag{3.11}$$

For the modified Morse-potential only numerical solutions are known. The measurement files in tab. 3.1 are required inputs for the modified Morse potential to calculate the energy levels and the lifetime of meta-stable states. The variables ω_e and $\omega_e\chi_e$ have the following relations [Demtröder 2018]:

$$\omega_e = \frac{\omega_0}{2\pi c} \tag{3.12}$$

$$\omega_e\chi_e = \omega_e^2 \frac{hc}{4D_e}. \tag{3.13}$$

The tab. 3.1 contains the dissociation energy D_0 from the ground state to the continuum. The true potential depth lies well within the uncertainty range of D_0. Assuming a minor effect on the ground state by the rotational modification the energy of the ground state can be calculated as $E(0) = \frac{\hbar\omega_0}{2}$. Assuming the central frequency ω_e with the relations of (3.12) yields a minor contribution for Cu_2^- of 0.024 eV whereas the uncertainty lies at 0.2 eV. For all further calculations $D_e \approx D_0$ is assumed.

Dimer	State	r_e[Å]	ω_e[cm^{-1}]	$\omega_e\chi_e$[cm^{-1}]	D_0[eV]	$D_{0,\text{calc}}$[eV]	Source
C_2^-	$X^2\Sigma_g^+$	1.2683	1781.189 ± 0.018	11.6717 ± 0.0048	8.11 ± 0.10	8.12	[Ervin and Lineberger 1991]
Al_2^-	$^4\Sigma_g^-$	2.558	335	—	$2.45[D_e]$	2.956	[Sunil and Jordan 1988]
Al_2^-	$^2\Pi_u$	2.461	355	—	$1.87[D_e]$	2.956	[Sunil and Jordan 1988]
Al_2^-	$^2\Pi_u$	2.720	287	—	$1.81[D_e]$	2.956	[Sunil and Jordan 1988]
Fe_2^-	—	2.10 ± 0.04	250 ± 20	—	1.53 ± 0.17	1.775	[Leopold, Almlöf, et al. 1988]
Co_2^-	—	2.31[8]	240 ± 15	—	—	1.768	[Leopold and Lineberger 1986]
Ni_2^-	X	2.257 ± 0.017	210 ± 25	—	1.84 ± 0.03	1.83	[Ho, Polak, et al. 1993]
Cu_2^-	$X^2\Sigma_u^+$	2.343 ± 0.007	196 ± 15	~ 0.7	1.62 ± 0.20	1.636/1.502	[Ho, Ervin, and Lineberger 1990]
Ag_2^-	$X^2\Sigma_u^+$	$2.480 + 0.124 \pm 0.007$	145 ± 10	~ 0.9	1.37 ± 0.16	1.371	[Ho, Ervin, and Lineberger 1990]
Au_2^-	$X^2\Sigma_u^+$	2.582 ± 0.007	149 ± 10	~ 0.7	1.92 ± 0.15	1.92	[Ho, Ervin, and Lineberger 1990]

Table 3.1: Accumulated data for anionic diatomic clusters. The data was used in the LEVEL16 calculations.

The potential depth for Co_2^- was calculated. The formula (3.14) calculates the dissociation energy D_0 [Ervin and Lineberger 1991] from the electron affinity of the uncharged dimer $EA(X_2)$ and monomer $EA(X)$ as well as from the potential depth of the uncharged dimer $D_0(X_2)$. D_0 is calculated as:

$$D_0(X_2^-) = D_0(X_2) + EA(X_2) - EA(X). \tag{3.14}$$

For Co_2^- the value of D_0 can be estimated by [Hales et al. 1994; Leopold and Lineberger 1986] to:

$$D_0(Co_2^-) = 1.32\ \text{eV} + 1.11\ \text{eV} - 0.662\ \text{eV} \tag{3.15}$$
$$= 1.768\ \text{eV}. \tag{3.16}$$

From the data set in tab. 3.1 the potentials shown in fig. 3.15 were calculated.

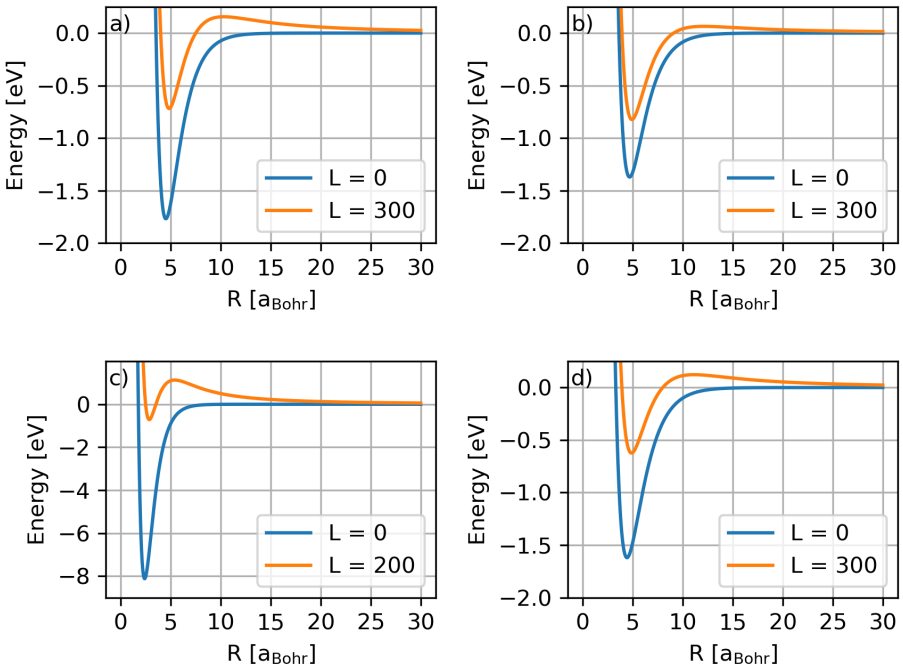

Figure 3.15: The figure shows modified Morse-Potentials (eqn. 3.10). L = 0 demonstrates the unperturbed Morse-Potential whereas L = 300/200 shows rotational barrier, where tunneling can happen. a) Denotes for Co_2^-, b) for Ag_2^-, c) for C_2^- and d) for reference Cu_2^-.

Tunneling

The modification of the potential with a rotational barrier allows metastable states, which lie above the dissociation threshold of the unperturbed ground state potential [Demtröder 2018]. Due to the finite height of the potential barrier, quantum mechanical tunneling is possible. States above the threshold decay via tunneling. The effect is known for example to cause α-particle decays in nuclei which was firstly explained by Gamow in 1928 [Gamow 1928]. To access the tunneling probabilities, the solution of the radial Schrödinger equation (3.17) for the modified Morse-potential is required [R. J. Le Roy 2017]. Additionally the quasi-bound states, i.e. states above the dissociation threshold of the ground-state, are to be identified.

$$-\frac{\hbar^2}{2\mu}\frac{d^2\Psi_{\nu,l}(r)}{dr^2} + V_l(r)\Psi_{\nu,l}(r) = E_{\nu,l}\Psi_{\nu,l}(r) \tag{3.17}$$

Fedor et al. combined three methods [Fedor et al. 2005] to find the approximated wave functions solving the radial Schrödinger equation for the anionic dimers. The Numerov method [Pang 1997] substitutes all derivatives of the radial Schrödinger equation by Taylor-Expansions for a simpler numerical treatment. A δ-function method was utilized for normalization of the continuum wave functions [Robert J Le Roy and Liu 1978]. To find the orbiting resonances, a phase shift technique was applied [Chen et al. 1994]. To gain access to the tunneling matrix element, the Wentzel-Brillouin-Kramers (WKB) method was used. It approximates the squared tunneling matrix element $|T|^2$ as shown in fig. 3.18 [Fedor et al. 2005]. It requires for integration the classical turning points of the potential barrier (r_a, r_b), the potential depth $V_{\text{eff}}(L, R)$ and the energy of the particle E, which in turn requires the solution of the radial Schrödinger equation (3.17). The wave functions which were obtained in the first step are used for the energy estimation in the integral [Fedor et al. 2005]. The integral starts and stops at the classical turning points for the energy levels, integrating the classical forbidden region between r_a and r_b [Fedor et al. 2005]:

$$|T|^2 = exp\left(-\frac{\sqrt{8\mu}}{\hbar}\int_{r_a}^{r_b}\sqrt{V_{\text{eff}}(L,R)-E}dR\right). \tag{3.18}$$

In former work [Fedor et al. 2005], the tunneling rates k were calculated from the squared tunneling matrix element and the attempt frequency ν as:

$$k = \nu|T|^2. \tag{3.19}$$

For this work the tunneling rates k were calculated by the program LEVEL16. It is the latest version of a program developed to solve the radial Schrödinger equation (3.17) for diatomic molecules numerically. It integrates eqn. (3.17) by the application of the Numerov method to remove all derivatives in the equation. The results are calculated on a grid with a maximum (RMAX) and minimum range (RMIN) [R. J. Le Roy 2017]. Additionally the eigenvalues and eigenfunctions are found by the Cooley-Cashion-Zare algorithm [R. J. Le Roy 2017]. It modifies the reduced mass to $\mu = \frac{m_A m_B}{m_A+m_B-m_e q}$, where the mass of the electron m_e and the charge of the particle q is propagated [R. J. Le Roy 2017]. The centrifugal term of the potential is modified by the projection of the electronic angular momentum Ω onto the internuclear axis [R. J. Le Roy 2017]:

$$E(L,\Omega) = \frac{(L(L+1)-\Omega^2)\hbar}{2\mu r^2}. \tag{3.20}$$

LEVEL16 delivers as result a list of all possible states for which the potential is not too shallow and if possible a decay rate as lifetime of the state.

Modelling of the decay process

The population of ro-vibrational states of the observed ions lead, under summation of all tunneling processes, to an envelope decay slope. Each tunneling process is

described as an exponential function with an amplitude and an exponent derived by LEVEL16. In contrast to the well-known single exponential function as seen in radioactive decays, the envelope decay slope depends on the underlying distribution of states. Assuming a smooth broad distribution, which might be approximated as constant for all states, leads to a 1/t power law decay [Fedor et al. 2005]. The general principle is shown in fig. 3.16 for arbitrary summed exponential functions.

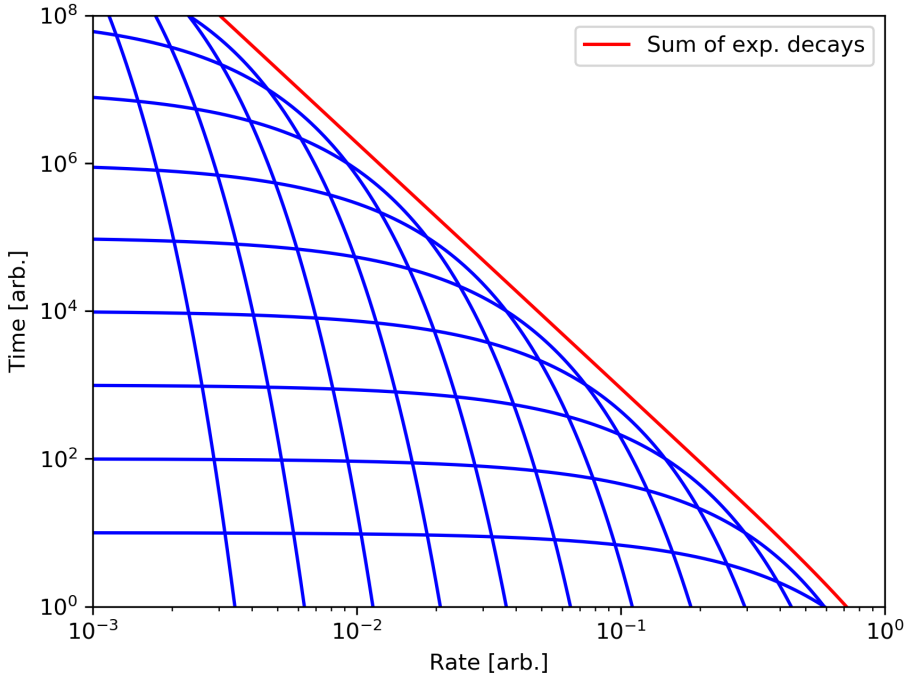

Figure 3.16: The figure shows the summation effect of 12 exponential decays - it shows a power law decay behavior.

In 2005 a model for the decay intensity was derived using the sum of tunneling rates fold with an distribution for the occupation of states, see eqn. 3.21 [Fedor et al. 2005]:

$$I(t) = \sum_{\nu,L} (2L+1) k(\nu, L) e^{-k(\nu,L)t} \rho(\nu, L). \tag{3.21}$$

The distribution was assumed to be constant over a broad range of rotational states L and vibrational states ν. Additionally, the large number of states was approximated as quasi-continuum and the sum was substituted by an integral. This resulted in the approximation of the decay rate as a 1/t power law.

3.6 Results

This thesis examined the decay of anionic dimers stored in the CSR. Three elements (carbon, cobalt and silver) were used to produce homonuclear anionic dimers. To

evaluate the effect of a heteroisotopic composition on the decay of anionic dimers, two different masses of silver dimers were stored in the CSR. The measurement time for the dimers ranged from 5 s to 1000 s. The decay rate was recorded on the charged fragment position as well on the neutral fragment position. Additionally, the decay rate was recorded in coincidence of both positions.

3.6.1 Comparison of fragmentation rates on NICE and COMPACT

From the decaying anionic dimers stored in the CSR, two signals have been recorded. The charged fragments were detected by COMPACT and the neutral fragments were detected by NICE. To evaluate the branching ratios between fragmentation and electron detachment, the neutral fragmentation rate on NICE was compared with the charged fragment rate on COMPACT. Electrons emitted from electron detachment of the anionic dimers are lost before they could be counted by detection system. The fragments are detected by COMPACT and NICE. COMPACT detects fewer particles than NICE. The count rate on COMPACT was scaled to the count rate of the first bin of NICE to compare the slope of both count rates. A second decay process is not compensated by the multiplication or addition of a single fixed value and leads to diverged slopes. Electron detachment for diatomic anions would be therefore indicated by diverged slopes between COMPACT and NICE. The following three measurements of anionic cobalt and silver dimers were used to demonstrate the rate on each detector. Tab. 3.2 shows the measurement details.

Dimer	Measurement time [s]	Time bins	Mass [amu]	Figure
Co_2^-	100	500	118	3.17
Ag_2^-	110	500	216	3.18
Ag_2^-	110	200	214	3.19

Table 3.2: Evaluated measurements for electron detachment.

The normalization process described in chap. 3.4.5 has been applied to the data beforehand. For comparability of the fig. 3.17 to fig. 3.19 the same time binning has to be used for the signals of both detectors. To assume Gaussian statistics at least 20 events per bin are required. The decay signal with lowest number of possible time bins which fulfills the criteria for Gaussian statistics, determines the time binning. The upper part (a)) of fig. 3.17 to fig. 3.19 shows the count rates per injection on NICE and COMPACT. The uncertainties derived in chap. 3.4.5 are based on the rate integrated over all injections. To propagate the uncertainties correctly, their values have been divided by the individual number of injections. The logarithmic scale of the y-axis suppresses the visibility of the uncertainties in the plot. The lower part b) of all three figures show the count rates on both detectors from which the individual dark count rate have been subtracted. The rate of the first bin of COMPACT has been scaled to the rate of NICE in the first bin. The subtraction

of the dark count rate from the signal rate leads to the quadratic addition of both uncertainties. Additionally, the scaling leads to the multiplication of the resulting uncertainties with the scaling factor. This leads to large uncertainties where the rate is mainly governed by the dark count rate. Here the low count rate limits the statistics. Fig. 3.17 to fig. 3.19 shows in part a) a similar slope of the rate on both detectors at the beginning of the measurement. Depending on the initial amount of particles, the slopes of the rates start to diverge at different times. As the rate from the decaying particles diminishes, the dark count rate of NICE ($\sim$ 60 s^{-1}) becomes dominant. This induces a bending of the rate towards the dark count rate of NICE as lower limit. The subtraction of the dark count rate on both detectors and the scaling of the COMPACT rate to the NICE rate in b) reveals an identical slope for the rate on both detectors. Here no effect of electron detachment could be identified up to 2 s, as the slopes align perfectly within the uncertainties. The effect of electron detachment would lead to diverged slopes of the rates on both detectors. The uncertainties become large and the signal of NICE shows a large scattering which makes the identification of an effect difficult as well. The electron detachment signal might be hidden in the large uncertainties.

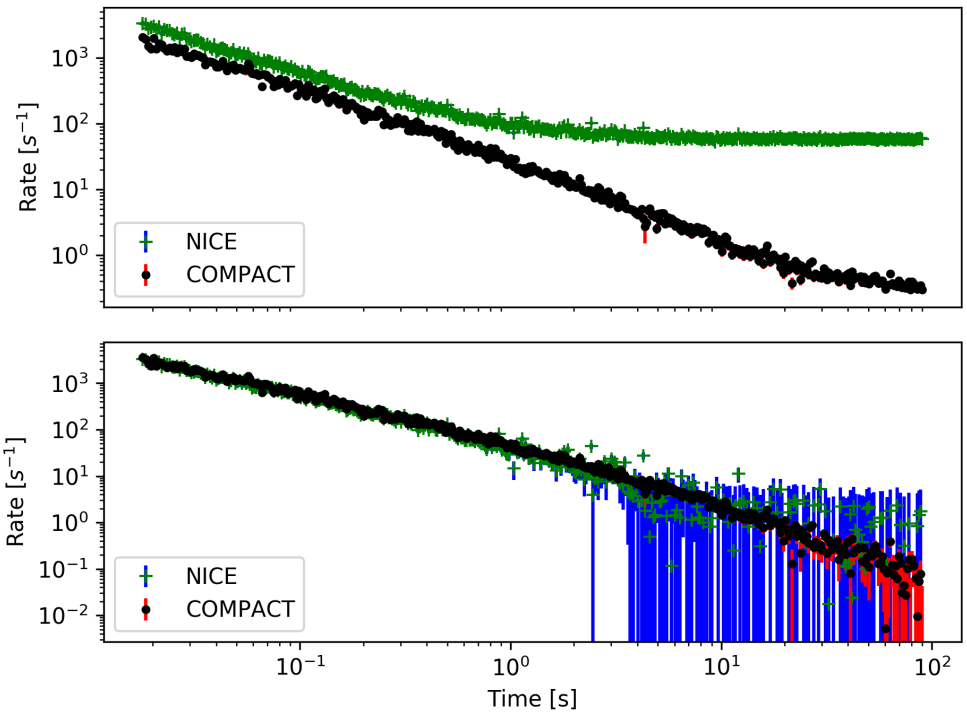

Figure 3.17: Decay pattern of Co_2^-. a) Neutral and charged fragments of the decay of Co_2^-. b) Same as in a) but corrected for the dark count rates and scaled to match.

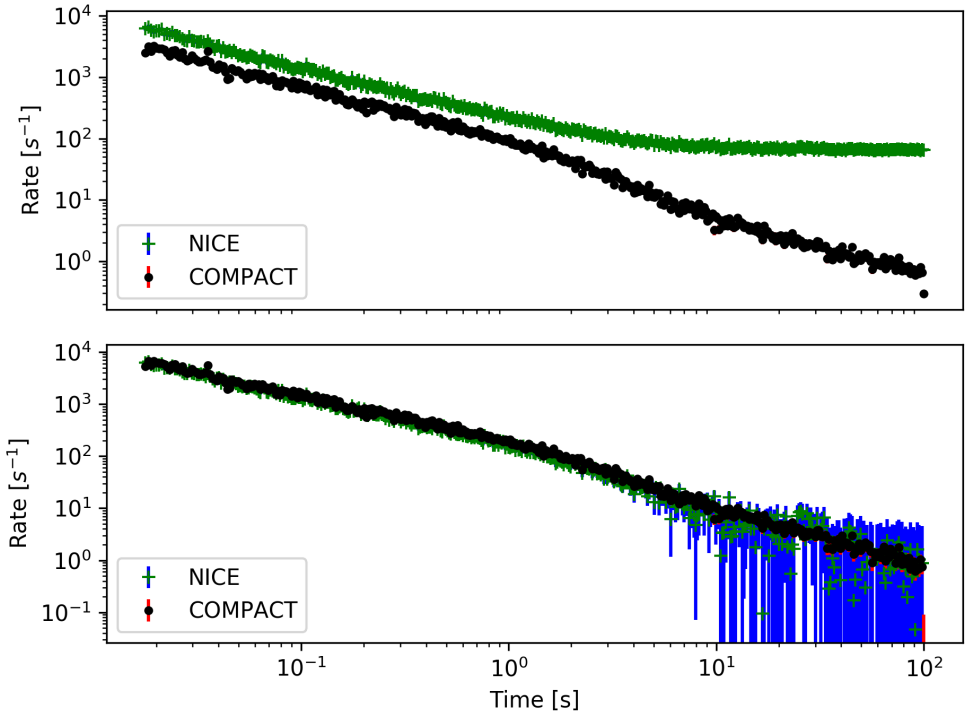

Figure 3.18: Decay pattern of Ag_2^- with mass 216 amu. a) Neutral and charged fragments of the decay of Ag_2^-. b) Same as in a) but corrected for the dark count rates and scaled to match.

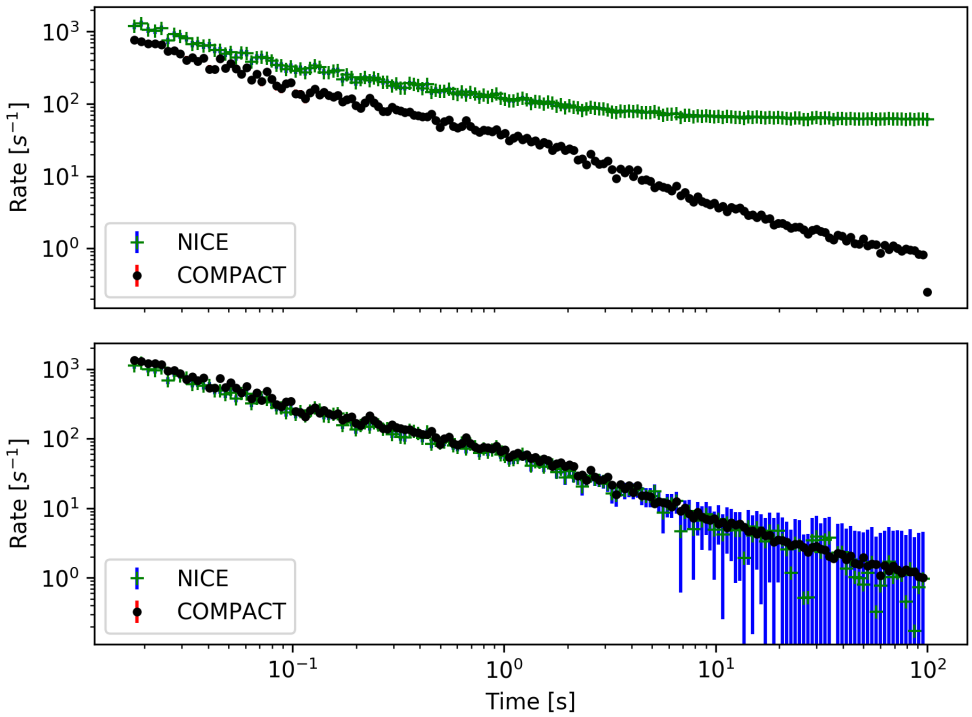

Figure 3.19: Decay pattern of Ag_2^- with mass 214 amu. a) Neutral and charged fragments of the decay of Ag_2^-. b) Same as in a) but corrected for the dark count rates and scaled to match.

3.6.2 Anionic cobalt dimer

Three measurements of the Co_2^- decay with measurement durations of 70 s, 100 s and 250 s were performed in 2015. The dark count rates of the detectors were determined during the last 10 s, 10 s, and 25 s, respectively, of each injection after the stored ions were dumped inside the CSR. The COMPACT detector was positioned at the charged fragment position (mass ratio mother daughter = 0.5). Only the measurement with a duration of 100 s employed both detectors, COMPACT and NICE, measuring both products in coincidence. The two remaining measurements only employed the COMPACT detector measuring the charged fragment.
The decay rates observed at the CSR deviate from the expected rates of a 1/t power law decay, which was found in earlier experiments at timescales of some ten milliseconds [Fedor et al. 2005]. The logarithmically binned decay rate for the anionic cobalt dimers, observed at the CSR showed a bending of the slope in a double logarithmic plot. A single power law would be represented as a straight line. Fitting the observed decay a new fit function was necessary. The 1/t power law decay was an approximation of the formula (3.21) [Fedor et al. 2005] which was successful on short time scales. A simple power law fit of the type $At^{-k} + d$ follows our measurements in good agreement for up to 0.7 s with an exponent of ~ 1. The described fragmentation process is based on the tunneling of quasi-bound states. To find the quasi-bound vibrational states of rotational excited dimers and the corresponding tunneling constants, the program LEVEL16 was employed. According to the formula (3.21), the individual tunneling process of the vibrational state ν of the rationally excited anionic dimer is weighted by a distribution of the ro-vibrational levels (L, ν). Only the highest available vibrational levels contribute to the decay pattern. The spacing between the levels reduces with increasing ν. For the highest available vibrational states and their nearest neighbor the required energy can be approximated as equal. For example the rotational state L = 308 requires at least 38 vibrational levels to be occupied before a lifetime for the tunneling process is found. For low lying vibrational levels which contribute to the decay pattern highly excited rotational states are required and the potential curves are shallow. For shallow potential cures the vibrational level spacing is small. The vibrational levels have a similar energy and can be approxmiated as equal. The vibrational part of the distribution has been approximated as constant. The fit function for the decay includes the individual tunneling constants and a distribution of the rotational states of the tunneling constants. A full description of the distribution would include an amplitude for each rotational state. The large number of rotational states, for the dimers examined in this thesis between ∼280 and ∼600, prevents a successful fit. The degrees of freedom must be reduced. Limiting the tunneling constants to the observed time span from 10 ms to 1000 s reduced the amount of rotational states slightly. The majority of rotational states have more than one vibrational level which can decay by tunneling. Limiting the time span removes rotational states only if all vibrational levels are excluded by their lifetimes. Sorting the tunneling constants by their corresponding rotational excitation and introducing a binning reduces the

degrees of freedom of the distribution. The bins are assigned with an amplitude. This type of fit was not successful due to the large spread of lifetimes within a bin. Combining short lifetimes with long lifetimes in one bin requires for the same time scale at least two contradictive weights. To solve this issue the tunneling constants are sorted by their decay time and are binned in time classes with an amplitude A_t. The resulting distribution is included into the fit function. In the beginning, all amplitudes are equal. The fit function weighs the individual exponential decay from the tunneling process with the corresponding value of the distribution. The weighted exponential functions are summed per bin g_{bin}. This sum is compared to the measured integrated rate per bin Y_{bin} and its uncertainty ΔY_{bin}. The function F_{bin} was minimized to fit the data by the least square method:

$$F_{bin} = \sqrt{\left(\frac{(g_{bin} - Y_{bin})}{\Delta Y_{bin}}\right)^2}. \tag{3.22}$$

The result of the minimizing process determined the amplitudes for the distribution of rotational states. Up to 120 time classes ranging from 1 ms to 1000 s were used for the distribution. The time classes are logarithmically binned within a decade for the fit. This binning distributes the amount of time classes per binning equally. The assigned amplitudes to each time-class allows a conversion to an angular momentum distribution. The angular momentum distribution is generated by summing the amplitudes $A_t(\nu, L)$ of the tunneling constants $k(\nu, L)$ for each L. From the angular momentum distribution, a weighted mean energy can be derived by the rotational energy $E(L)$ (eqn. 3.20 with $\Omega = 0$).

$$E_{Mean} = \frac{\sum_L A_t(\nu, L) E(L)}{\sum_L A_t(\nu, L)} \tag{3.23}$$

Single detector evaluation

From the former evaluation of the two detector signals, no difference between the charged fragment channel and the neutral fragment channel could be identified. Therefore, a single detector evaluation is possible and all available measurements have been evaluated. It is based on the data recorded by COMPACT. To fit the time class distribution, the method described above is applied to all three files.
Fitting the time class distribution is difficult as the degrees of freedom increase with the number of time classes. Additionally, the fit parameters for the time class distribution require boundaries. To prevent the overpopulation of a single time class an upper limit is to be defined. A distribution containing an overpopulated time class for short lifetimes and a few sparsely populated time classes can be used to describe the observed decay pattern. This distribution would require a state selective ion source. Only the highest available vibrational level per rotational state would contribute to the decay pattern. For example the rotational state L = 308 has two vibrational levels $\nu = 54$ and 55 with a lifetime of 1.46 ms and 200.5 s. A single overpopulated time class for short lifetime would prefer only $\nu = 54$. The ion source

employed for theses measurements is known to produce ions with a broad energy distribution which contradicts the described selectivity. The measurement for 250 s of the anionic cobalt dimer yields the best statistics and up to 120 time classes have been fitted to the decay. It will be used in the following as benchmark. The two fig. 3.20 and fig. 3.21 demonstrate the effect of the fit boundaries on the distribution. The lower limit was fixed to zero but the upper limit was varied between 2 and 100. Starting from an equal continuous distribution of amplitudes for the time classes the variation of the maximum amplitudes allows to acquire a stable solution for the fit and a distribution with minimal constrains on the amplitudes. The dark count rate as an additional parameter for the fit was allowed to vary from 20 s^{-1} to 300 s^{-1}. The top part a) of these three figures shows the data and the fitted curve. The middle part b) of the figures shows the fitted time class distribution. The bottom part c) of the figures shows the distribution derived from part b) for the occupation of rotational states. Fig. 3.20 shows a fit in agreement with the data in a) with 30 time classes and an upper boundary of 100 for the amplitudes. An χ^2_{red}= 0.86 was achieved. But in the part b) of fig. 3.20 a single time class dominates the distribution.

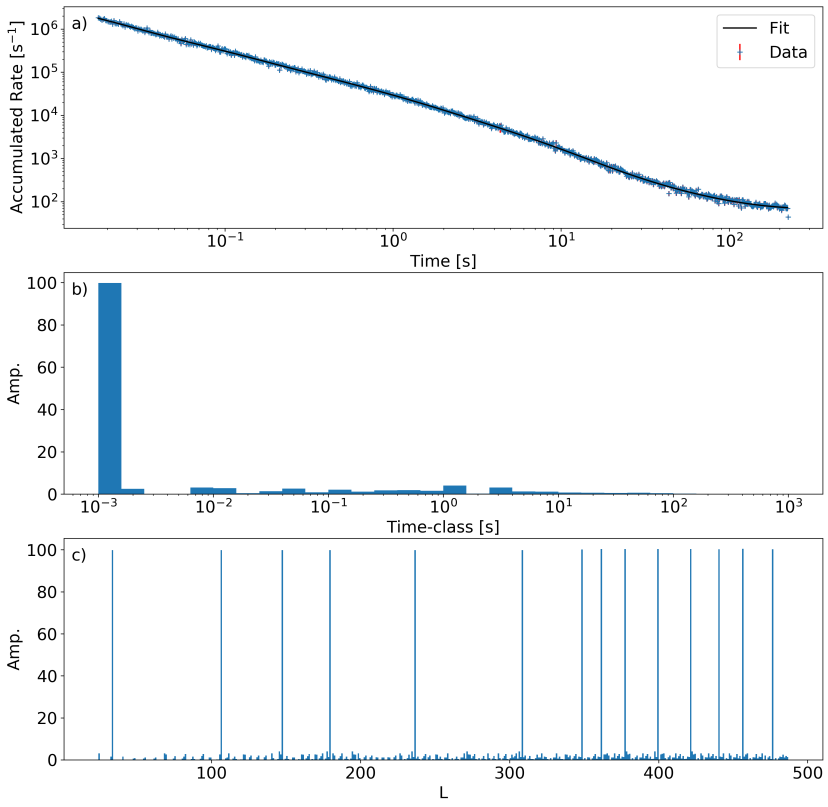

Figure 3.20: The figure shows the decay signal recorded for a measurement of 250 s. a) Shows the normalized count rate which has been fitted by the described method with 30 time classes. b) Displays the time class distribution for a maximum amplitude of 100. c) Demonstrates the to b) equivalent distribution of rotational states.

The fit with a maximum amplitude of 100 has been performed with an increasing number of time classes. Starting with 6 time classes the value was increased in steps of 6 to 30 time classes. Only fits up to 18 time classes could demonstrate a quasi-continuous population of time classes without a dominating time class. The maximum amplitude of these distributions is ∼2. Decreasing the maximum amplitude to an value of 4 introduces two dominating time classes. It is required to reduce the maximum amplitude for the fit further. Fig. 3.21 shows the results for the fit with a maximum amplitude of 2 and 30 time classes. Fig. 3.21 a) shows a fit in agreement with the data and a χ^2_{red} of 0.87 was achieved. No overpopulated time classes can be identified in fig. 3.21 b). The distribution is broad and yields a mean energy of 1.37 eV. Fig. 3.21 c) shows more populated rotational states with less variation of amplitudes.

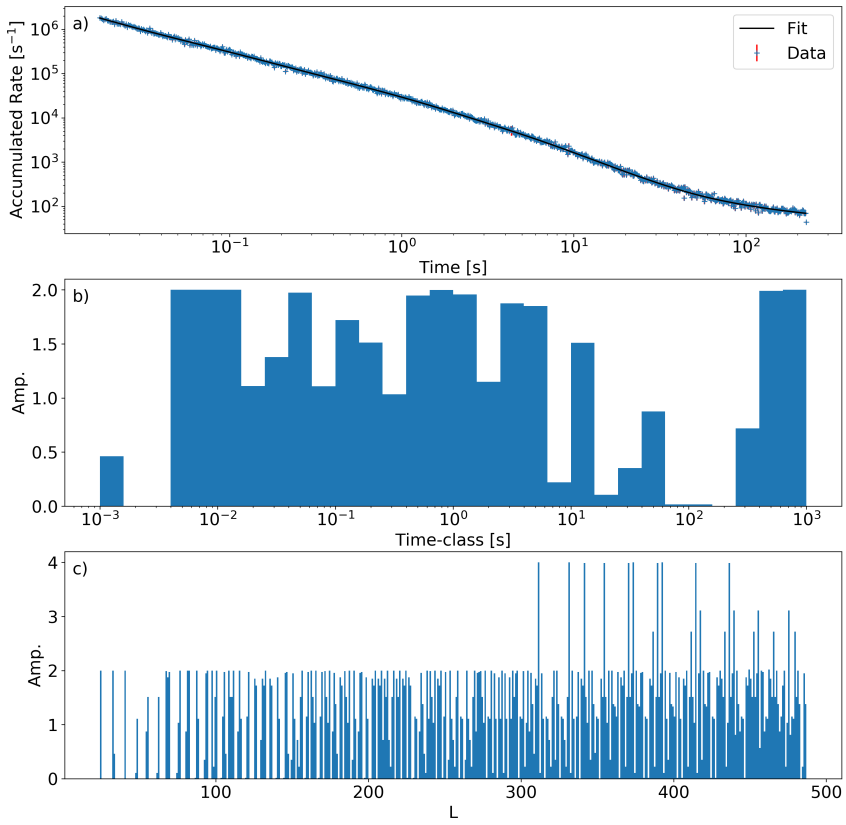

Figure 3.21: The figure shows the same as fig. 3.20 but with a maximum amplitude of 2.

The mean energy varies only little for increasing the number of time classes. The fits achieved a maximum χ^2_{red} value of 0.97 for a distribution of 120 time classes. The χ^2_{red} value increased slowly from 0.85 to 0.97 with the increasing number of time classes. Overall stable conditions are achieved by limiting the amplitudes to 2. Tab. 3.3 shows the results for the examined limits of the upper amplitude. The upper

limit for all further examined anionic cobalt dimers is set to 2.

Lower limit	Upper limit	Time classes	χ^2_{red}	$E_{rot,mean}$[eV]
0	2	30	0.87	1.37
0	2	120	0.97	1.38
0	4	30	0.86	1.37
0	100	30	0.86	1.46

Table 3.3: Results for fitting the rotational occupation by time classes for a measurement of 250 s.

For a better comparison between the available measurements the number of time classes was limited to 36. Fig. 3.22 shows the same measurement as fig. 3.21 only with 36 time classes. The conversion of the time class distribution yields a quasi uniform occupation of rotational states. The modulation of the occupation allows the fit function to follow the bending slope of the decay pattern.

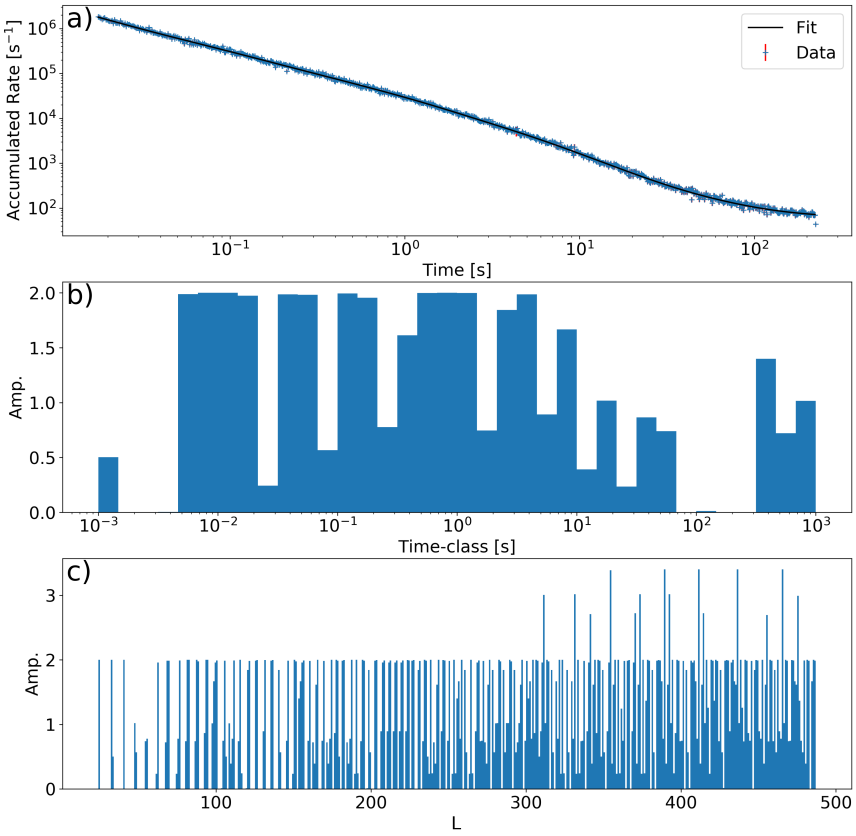

Figure 3.22: Shows the same as fig. 3.21 but with 36 time classes.

Limiting the fits to 36 time classes with an amplitude ranging from 0 to 2 for all three files resulted in fits agreeing with the data. Additionally these limits allow

to compare the result from the coincidence measurement with the data set from the single detector evaluation. The χ^2_{red} ranged from 0.81 to 1.17. The fits were performed with 500 to 1000 bins depending on the available statistics. The mean rotational energy for 36 time classes ranged from 1.36 eV to 1.39 eV. This lies well within the groundstate potential depth of $\sim$ 1.77 eV. The results for all three measurements are shown in tab. 3.4.

Measurement time [s]	Bins	χ^2_{red}	$E_{rot,mean}$[eV]
70	500	0.81	1.37
100	500	1.17	1.36
250	1000	0.87	1.39

Table 3.4: Mean energy, χ^2_{red} and the amount of available data bins for the charged fragment measurements of the anionic cobalt dimer.

Coincidence measurements

For the measurement of 100 s the decay pattern was recorded with both detector channels. Both channels were evaluated for coincidence events. The resulting decay pattern was fitted with the same procedure. Only 100 time bins were available for the fit which limited the amount of time classes to less than 100. The fit with the best agreement was achieved for 36 time classes and resulted in a $\chi^2_{red} = 1.03$. Fig. 3.23 shows the fit result. The resulting distribution of time classes strongly differs from the already observed distribution in fig. 3.22. The distribution has a pronounced structure at $\sim$1 ms and the time classes above 5 ms have amplitudes below 0.5. The high amplitudes of $\sim$2 for this file, are distributed over the full range of rotational states. This possibly correlates to the pronounced structure in the time classes. Nevertheless a mean rotational energy of 1.39 eV was found for this case which fits well within the previously found range for the mean rotational energy from 1.36 eV to 1.39 eV. It was demonstrated that a distributions of states could be found for each examined measurement by fitting the data with time classes. The resulting distribution for the time classes as well for the occupation of rotational states follow no single Boltzmann distribution. The mean energy varied between 1.36 eV and 1.39 eV. The fit funciton generates a single broad distribution for the measurement.

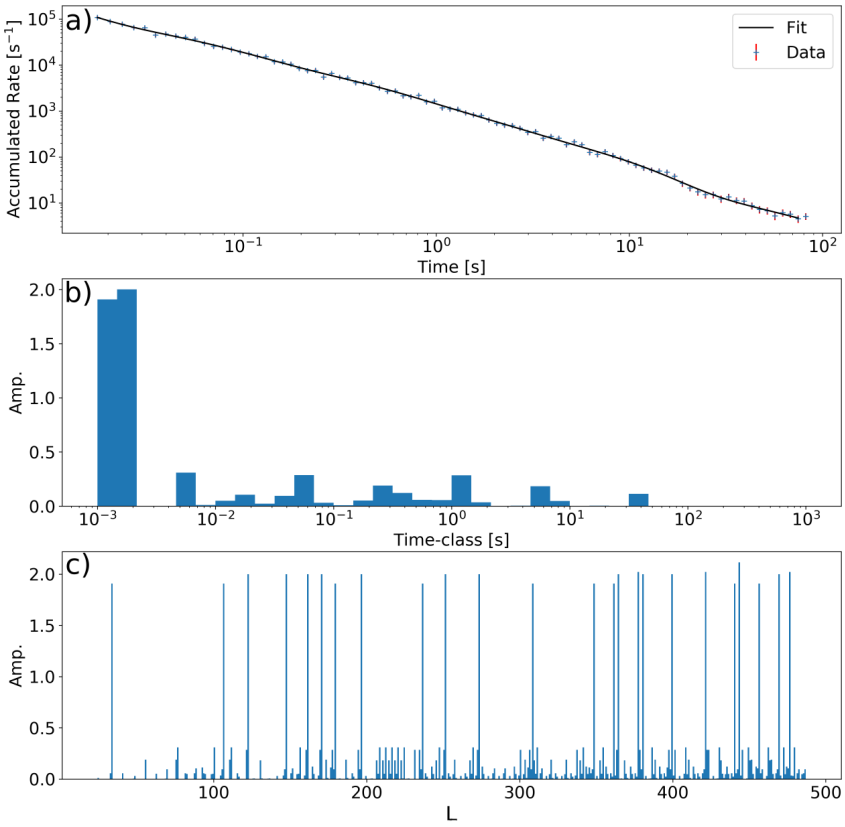

Figure 3.23: Shows the same as fig. 3.22 but for the coincidence measurement of 100 s.

3.6.3 Anionic silver dimer

The measurement files of anionic silver dimers were acquired during the first cryogenic beam time in 2015 of the CSR. Thirteen files were evaluated. At the end of each injection the ion beam was dumped in the CSR to record the dark count rate of the detectors for a minimum of 5% of the measurement time. Nine files were obtained by storing silver dimers with the mass 216 amu in the CSR. The Storage time ranged from 5 to 1000 s. Four files were acquired with the COMPACT detector at the neutral fragment position. For the remaining five files the COMPACT detector was positioned at the charged fragment position (mass ratio mother daughter = 0.5). The NICE detector was employed for four of these nine files which resulted in four coincidence measurements. The decay pattern for the diatomic anions with the mass 214 amu was recorded in four measurements. The measurement time ranged from 15 s to 110 s. All details of the mentioned measurements are listed in tab. 3.5. The decay rates observed at the CSR deviate from the expected rates of a 1/t power law. The fit function used in the following is described in chap. 3.6.2 for the anionic cobalt dimers. The paramters were limtied to 36 time classes and an amplitude range of 0 to 2.

Particle mass [amu]	Measurement time [s]	COMPACT position	Max bins	Coincidence
216	25(3)	neutral	500	false
216	60(10)	neutral	200	false
216	300(20)	neutral	100	false
216	1000(50)	neutral	100	false
216	350(50)	charged	50	false
216	5(1)	charged	500/200	true
216	15(2)	charged	1000/500	true
216	110(10)	charged	500/200	true
216	110(10)	charged	100/50	true
214	15(2)	charged	500/200	true
214	110(10)	charged	500/200	true
214	15(2)	charged	500/200	true
214	110(10)	charged	500/200	true

Table 3.5: Details on acquired measurements. The brackets in the column "measurement time" indicate the time interval for the dark count rate measurement. In the column "Max bin" corresponds the first position or the single position to to maximum number of logarithmic bins which are statistically possible for COMPACT. The maximum number of logarithmic bins for NICE follows from the second position of the column "Max bin".

COMPACT measurements

The measurements obtained with COMPACT can be split up in two main parts. The detection of neutral fragments and the detection of charged fragments. Additionally two different masses were acquired for these measurements to examine the influence of a heteroisotopic composition of the dimers on the decay process.

COMPACT on neutral fragment position

Four measurements were obtained with COMPACT at the neutral fragment position. The measurement time ranged from 25 s to 1000 s. Only particles with mass 216 amu were used for the neutral fragment measurements. For better comparison the number of time classes was in the following limited to 36. Therefore one could evaluate measurements with low statistics. Fig. 3.24 shows the fit result to the measurement for 25 s. Fig. 3.24 a) shows a fit in agreement to the data. A χ^2_{red} of 1.17 was achieved. The time class distribution shows as pronounced structure between 1 ms and 3 ms with an amplitude of $\sim$2. The remaining structures are localized and show amplitudes below 0.75. The time class distribution converts to a broad distribution of rotational states with a sparsely populated area between L = 460 and L = 560. The amplitudes above 2 in the distribution of rotational states originate form the structure between 1 ms and 3 ms in the time class distribution. The distribution of rotational states corresponds to a mean energy of 0.79 eV.

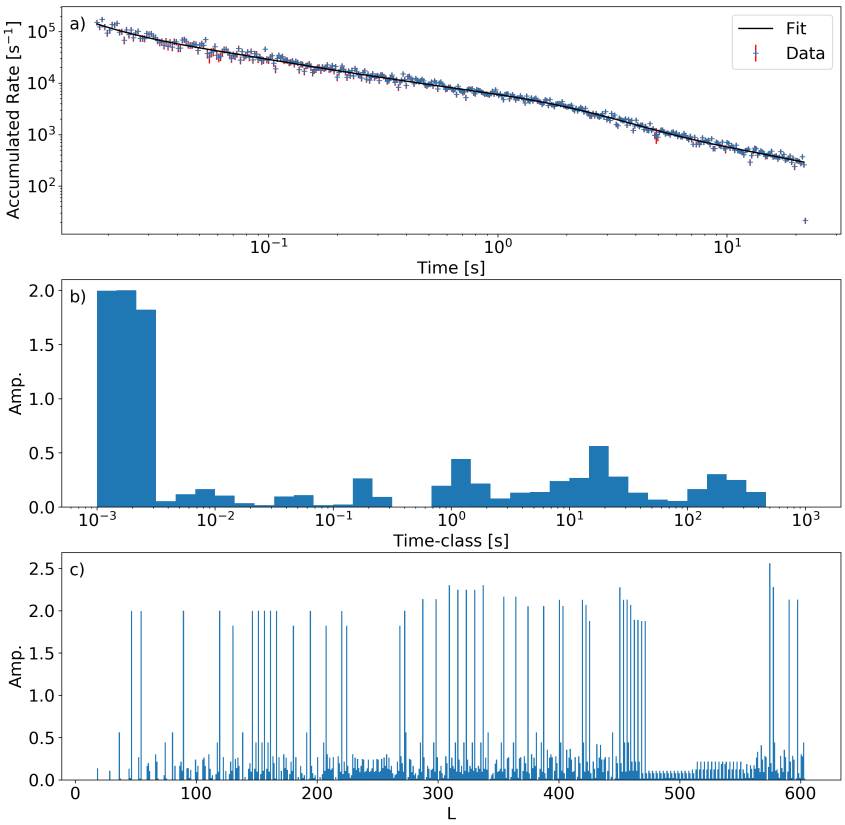

Figure 3.24: The figure shows the decay signal recorded for a measurement of 25 s (216 amu). a) Shows the normalized count rate which has been fitted by the described method with 30 time classes. b) Displays the time class distribution for a maximum amplitude of 2. c) Demonstrates the to b) equivalent distribution of rotational states.

Combining all neutral fragment measurements demonstrates a stable mean energy in the range 0.83 eV to 0.85 eV. The recorded signals of all neutral fragment measurements could be fit in good agreement with the data by the fit function. The summed results can be found in tab. 3.6. The mean energy ranged from 0.83 eV (measurement for 60 s) to 0.85 eV (measurement for 1000 s) while the χ^2_{red} varied between 0.91 (measurement for 1000 s) and 1.47 (measurement for 300 s).

Measurement time [s]	Bins	χ^2_{red}	$E_{rot,mean}$[eV]
25	500	1.17	0.84
60	200	1.12	0.83
300	100	1.47	0.84
1000	100	0.91	0.85

Table 3.6: Mean energy, χ^2_{red} and the amount of available data bins for the neutral fragment measurements of the anionic silver dimer with the mass 216 amu.

COMPACT on charged fragment position

For the particle mass 216 amu five measurements are available. The storage time ranges from 5 s to 350 s. The number of possible logarithmic bins varied from 50 to 1000. The example in the following fig. 3.25 demonstrates a measurement of 15 s with a maximum of 1000 logarithmic bins. Limiting the time classes to 36 results in fit with a $\chi^2_{red} = 1.25$. The fit to the data is shown in fig. 3.25 a). The time class distribution fig. 3.25 b) contains several localized structures with amplitudes of up to 2. The space between 2 ms and 10 ms is unpopulated. This Time class distribution converts to a broad distribution of rotational states fig. 3.25 c). A local minimum between L≈460 and L≈560 can be observed.

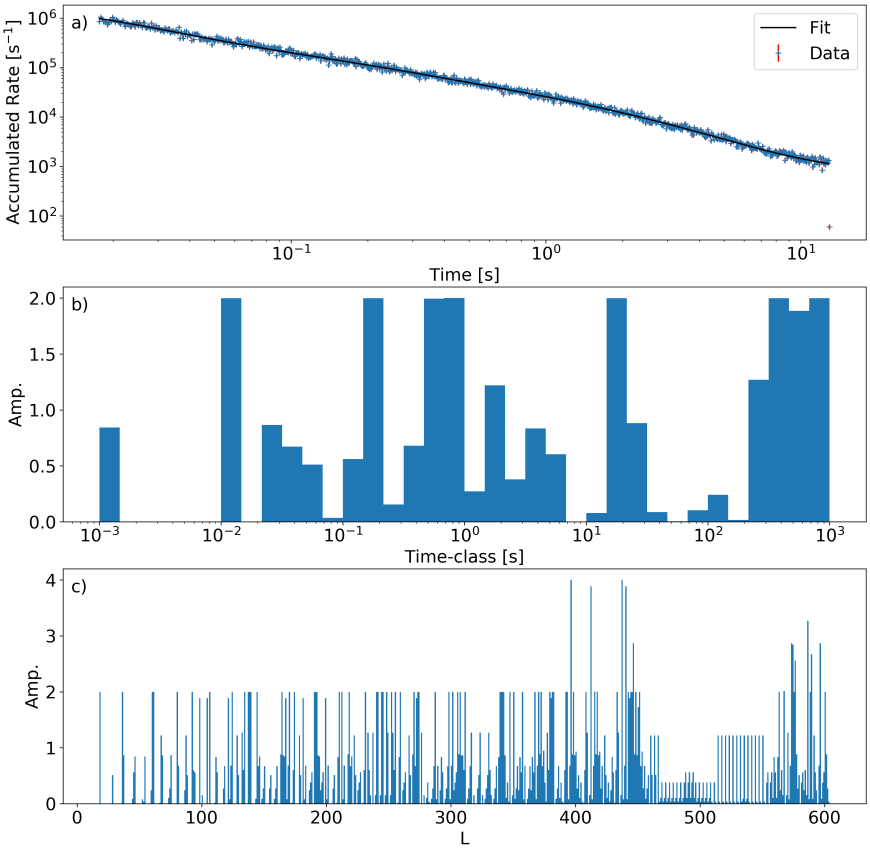

Figure 3.25: The figure shows the decay signal recorded for a measurement of 15 s(216 amu). a) Shows the normalized count rate which has been fitted by the described method with 30 time classes. b) Displays the time class distribution for a maximum amplitude of 2. c) Demonstrates the to b) equivalent distribution of rotational states.

The results for the fit to the neutral and the charged fragments show comparable results. The mean energy for the charged fragments ranges from 0.80 eV (measure-

ment for 110 s with 100 bins) to 1.00 eV (measurement of 5 s with 500 bins). The χ^2_{red} ranged for this measurement file from 1.15 (measurement for 110 s with 100 bins) to 3.81 (measurement for 350 s with 50 bins).

Measurement time [s]	Bins	χ^2_{red}	$E_{rot,mean}$[eV]
350	50	3.81	0.88
5	500	1.33	1.00
15	1000	1.25	0.86
110	500	1.17	0.89
110	100	1.15	0.80

Table 3.7: Mean energy,χ^2_{red} and the amount of available data bins for the charged fragment measurements of the anionic silver dimer with the mass 216 amu.

Changing the mass of the particle to 214 amu introduces a monoisotopic dimer. This requires a recalculation of the tunneling constants as the reduced mass influences the effective potential. The measurements of the anionic silver dimers with the mass 214 amu were fitted with same procedure as before. Limiting the number of time classes to 36 and the amplitudes to two. The storage time was either 15 s or 110 s. The statistics of the measurements allowed 200 or 500 logarithmic bins. The fit result is demonstrated in fig. 3.26 a). Here a fit with a χ^2_{red} of 1.01 was achieved. The plot in the middle of fig. 3.26 b) shows the time class distribution. A pronounced time class with an amplitude of $\sim$2 can be found around 1 ms. Three localized structures can be found from 5 ms to 100 ms, from 130 ms to 500 ms and from 700 ms to 300 s. The amplitudes of the localized structures are smaller than 1. The conversion to the rotational distribution fig. 3.26 c) yields a broad distribution with several high peaks and a gap with values below 0.5 for the amplitudes between L$\approx$460 and L$\approx$560. From this distribution a mean energy of 0.90 eV was calculated. Tab. 3.8 shows the results from the fits for the anionic dimers with mass 214 amu. The χ^2_{red} ranged from 1.04 (measurement 1 for 15 s) to 1.19 (measurement 2 for 110 s) The mean energy ranges from 0.85 eV (measurement 2 for 110 s) to 0.91 eV (measurement 2 for 15 s).

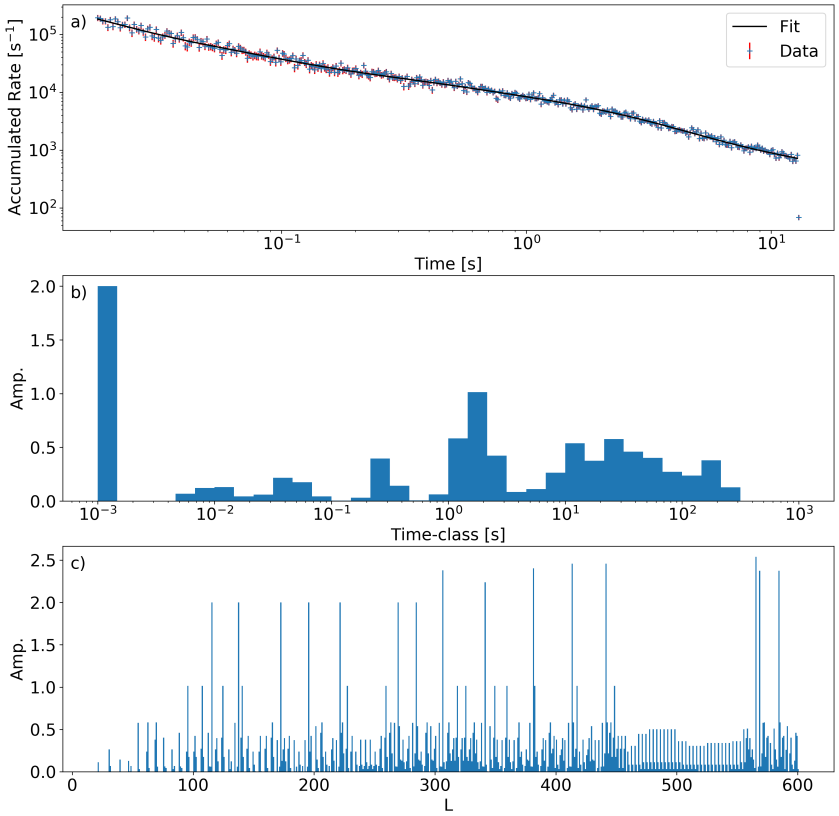

Figure 3.26: The figure shows the decay signal recorded for a measurement of 15 s (214 amu). a) Shows the normalized count rate which has been fitted by the described method with 36 time classes.b) Displays the time class distribution for a maximum amplitude of 2. c) Demonstrates the to b) equivalent distribution of rotational states.

Measurement time	Number	Bins	χ^2_{red}	$E_{rot,mean}$[eV]
15	1	500	1.04	0.9
110	1	500	1.16	0.86
15	2	500	1.12	0.91
110	2	500	1.19	0.85

Table 3.8: Mean energy, χ^2_{red} and the amount of available data bins for the charged fragment measurements of the anionic silver dimer with the mass 214 amu.

Coincidence measurements

The coincidence measurements were performed for two masses of the anionic silver dimer. The measurements can be split up in two groups. First the heteroisotopic dimer with the mass 216 amu and second the monoisotopic dimer with the mass 214 amu. For the mass 216 amu four files with storage times between 5 s and 110 s were

available. From the statistics of the files follows a range for the logarithmic bins of 200 to 1000. The fig. 3.27 in the following demonstrates the fit in agreement to the coincidence signal obtained by NICE and COMPACT with 200 logarithmic bins for the mass 216 amu. Fig. 3.27 a) shows the fit to the coincidence data which resulted in a χ^2_{red} of 0.85. The distribution of time classes in fig. 3.27 b) shows three localized structures. The first structure can be found around 1 ms, the second stucture starts at 7 ms and stops at $\sim$ 3 s. The last structure is observed from 10 s to $\sim$ 30 s. The amplitudes reach a maximum value of 0.2. The distribution of rotational states in fig. 3.27 b) shows a broad configuration. A local minimum between L≈480 and L≈520 can be found. Several peaks above 0.2 can be observed. The mean energy has been calculated to 0.85 eV for this fit.

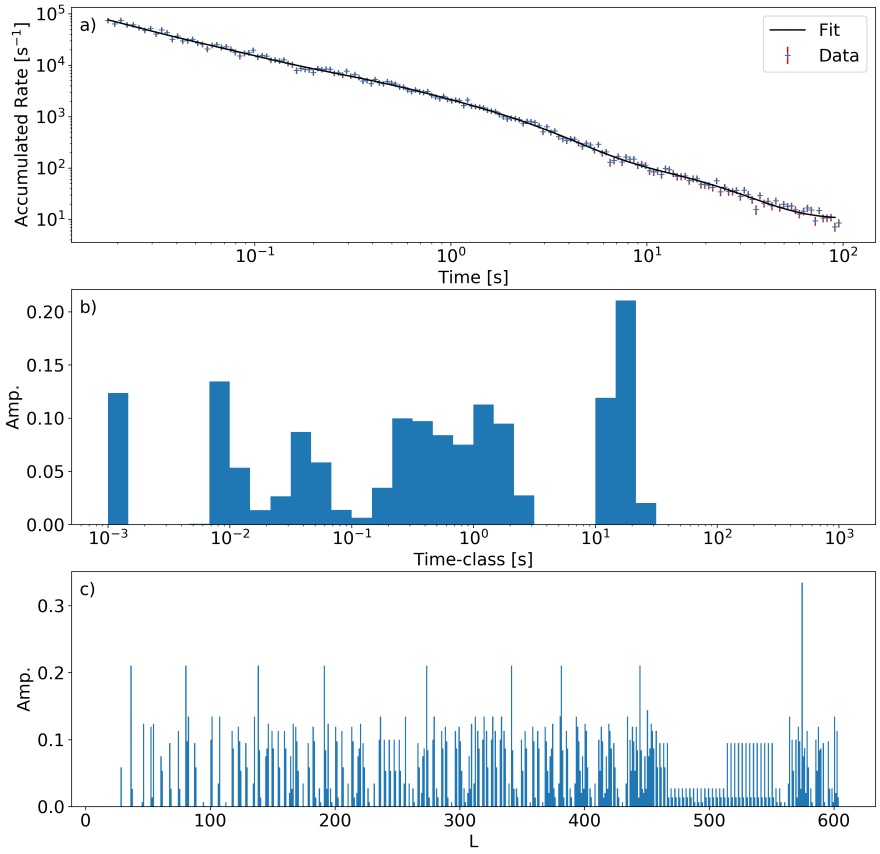

Figure 3.27: The figure shows the decay signal recorded for a coincidence measurement of 110 s (216 mau). a) Shows the normalized count rate which has been fitted by the described method with 36 time classes. b) Displays the time class distribution for a maximum amplitude of 2. c) Demonstrates the to b) equivalent distribution of rotational states.

Tab. 3.9 shows the data set for all fits to the corresponding measurement. Here the mean energy ranged from 0.84 (measurement for 110 s with 100 bins) eV to 0.86 eV (measurement for 15 s with 500 bins). The χ^2_{red} covers a broader range from 0.85 (measurement for 110 s with 500 bins) to 4.76 (measurement for 110 s with 100 bins).

Measurement time [s]	Bins	χ^2_{red}	$E_{rot,mean}$[eV]
5	200	1.06	0.85
15	500	1.12	0.86
110	200	0.85	0.85
110	50	4.76	0.84

Table 3.9: Mean energy,χ^2_{red} and the amount of available data bins for the coincidence measurements of the anionic silver dimer with the mass 216 amu.

For the second set of measurements the experiments were conducted on the anionic silver dimer with the mass 214 amu. Four measurements are available. The measurement time was set to 15 s or 110 s. The following fig. 3.28 a) shows the fit in agreement to the data with a χ^2_{red} of 0.87. The time class distribution is sparsely populated. Five small structures can be observed around 1 ms, from 7 ms to 13 ms, from 50 ms to 100 ms, from 500 ms to 7 s and from 13 s to 43 s. The first structure around 1 ms has the highest amplitude of ∼1.8. The remaining populated time classes have amplitudes below 0.3. This distribution also results in an sparsely populated distribution of rotational states. Locally several high populated states can be found as result from the pronounced time class around 1 ms. Between L≈440 and L≈560 a gap can be found. The distribution or rotational states yields a mean energy of 0.86 eV. Tab. 3.10 shows the combined information of the coincidence measurements for the anionic silver dimer with mass 214 amu. The mean energy ranges from 0.81 eV (measurement 2 for 15 s) to 0.89 eV (measurement 1 for 15 s). The χ^2_{red} ranges from 0.87 (measurement 2 for 110 s) to 1.15 (measurement 1 for 110 s).

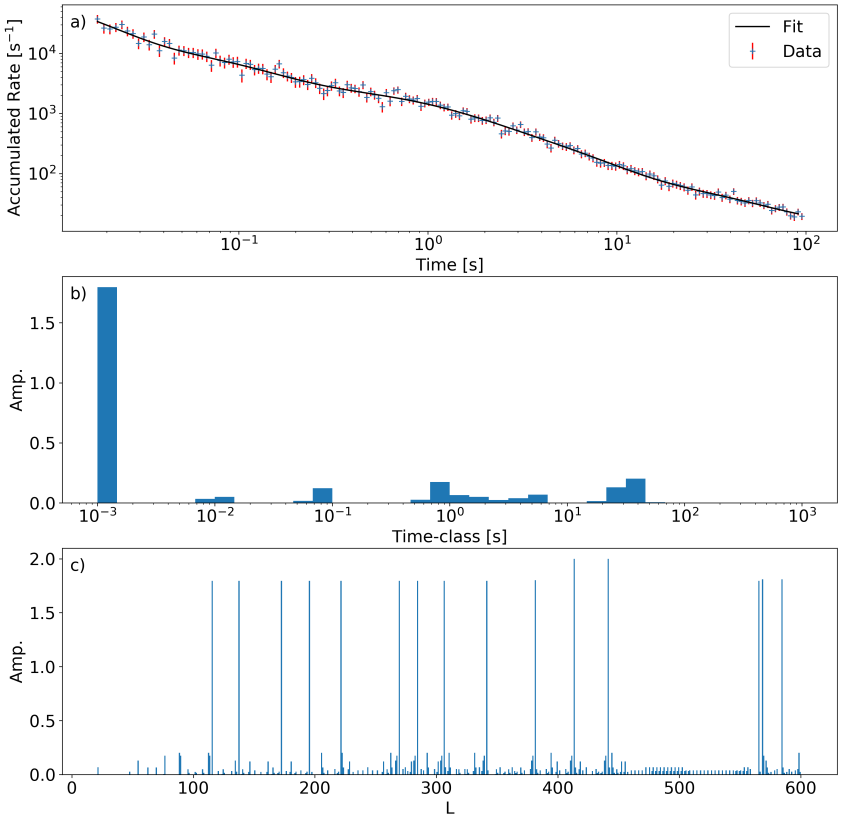

Figure 3.28: The figure shows the decay signal recorded for a coincidence measurement of 110 s (214 amu). a) Shows the normalized count rate which has been fitted by the described method with 36 time classes. b) Displays the time class distribution for a maximum amplitude of 2. c) Demonstrates the to b) equivalent distribution of rotational states.

Measurement time [s]	Number	Bins	χ^2_{red}	$E_{rot,mean}$[eV]
15	1	200	0.96	0.89
110	1	200	1.15	0.87
15	2	200	1.06	0.81
110	2	200	0.87	0.86

Table 3.10: Mean energy, χ^2_{red} and the amount of available data bins for the coincidence measurements of the anionic silver dimer with the mass 214 amu.

For the dimer with the mass 216 amu the mean energy ranges from 0.8 eV to 1 eV. The evaluation of the measurements for the mass 214 amu results in a range of 0.81 eV to 0.9 eV. Both mean energy ranges overlap and the difference in the range can be attributed to the statistics of the files.

3.6.4 Anionic carbon dimer

The measurements of the anionic carbon dimers were obtained during the first and the second cryogenic beam time of the CSR. Four measurements have been acquired from COMPACT. The storage time ranges from 23 s to 520 s. The logarithmic bins range from 50 to 200. Two measurements were acquired with COMPACT at the neutral fragment position. For the remaining two measurments COMPACT was positioned at the charged fragment position (mass ratio mother daughter = 0.5). Detailed information can be found in tab. 3.11. A process which leads to neutralization and which is not well understood [Pedersen et al. 1998] required a delay of 100 ms for the fit function on both positions. The experimental aim of the measurements was the autofragmentation process.

Year	Measurement time [s]	COMPACT position	Max bins
2015	230(30)	neutral	50
2015	23(3)	neutral	100
2015	23(3)	charged	50
2017	520(20)	charged	200

Table 3.11: Details on acquired measurements. The brackets in the column "measurement time" indicate the time interval for the dark count rate measurement. The column "Max bins" corresponds to the maximum number of logarithmic bins which are statistically possible.

Neutral fragment measurement with COMPACT

The fits are limited to 30 time classes. The low statistic of the measurements required a reduction to 30 time classes for the comparison. For neutral fragments two measurements are available with 230 s and with 23 s. For the following example in fig. 3.29 the measurement with 23 s is used due to its statistics. Fig. 3.29 a) shows the fit in agreement with the data. Limiting the fit to a minimum time of 100 ms lead to a χ^2_{red} of 1.57. The time class distribution Fig. 3.29 b) shows three structures of the occupied time classes. The main structure starts at ∼150 ms and continues to 1000 s with maximum amplitude of two. A minor structure can be found between 23 ms and ∼ 60 ms. Between 1 ms and 6 ms a second minor structure is observed. The converted occupation of rotational states Fig. 3.29 c) shows a distributed structure of peaks. The amplitudes range from 0 to 2. The mean energy of this file with 30 time classes corresponds to 6.07 eV. For the second file a mean energy could be attributed of 5.47 eV for 30 time classes with a χ^2_{red} of 3.16 which can be attributed to the low number of bins.

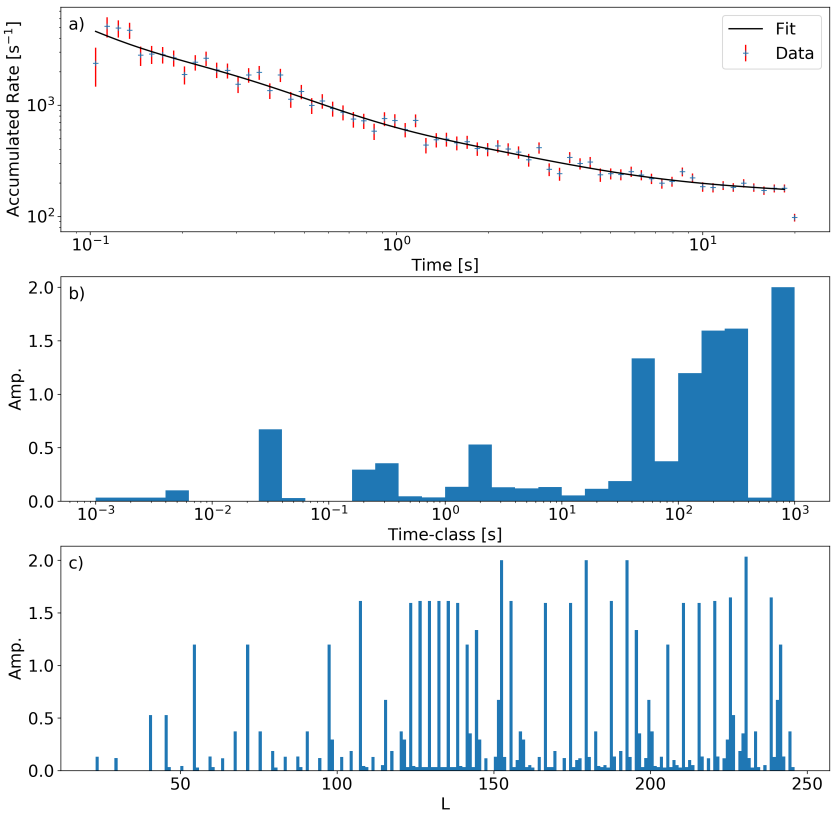

Figure 3.29: The figure shows the decay signal recorded for a measurement of 23 s. a) Shows the normalized count rate which has been fitted by the described method with 36 time classes. b) Displays the time class distribution for a maximum amplitude of 2. c) Demonstrates the to b) equivalent distribution of rotational states.

Charged fragment measurement with COMPACT

For the charged fragment the same limitation to 30 time classes was used. The two measurements of the charged fragment with COMPACT have been taken in two different beam times. A measurement for 520 s was taken during the second cryogenic beam time of the CSR. During this beam time a switching method was applied. The switching method was used due to the high intensities in the beginning of the detachment process of C_2^-. By switching off the COMPACT detector, higher beam intensities were injected into the CSR. For this mode the converter plate in front of the MCP stack of COMPACT was switched from -184 V, in the on state, to 297 V for the off state. Additionally, the voltage for the MCP front is set to 268 V. The measurement for 520 s included a 100 ms delay after the injection for the activation of COMPACT. The measurement for 23 s was acquired during the first cryogenic beam time without switching the potentials of COMPACT. In the following the measurement for 520 s will be used as an example due to its statistics. The measurement is binned into 200 logarithmic bins. Fig. 3.30 a) shows the fit

to the data. The first 100 ms were ignored for the measurement. A χ^2_{red} of 2.40 was achieved for this measurement and 30 time classes. The time class distribution fig. 3.30 b) is populated with seven localized structures of which three contain time classes with an amplitude of $\sim$ 2. The converted distribution of rotational states shows an floor of peaks with several high amplitudes of $\sim$2. The mean energy from this distribution can be derived to 5.86 eV. The second measurement for 23 s a mean energy of 6.33 eV was estimated. A χ^2_{red} of 10.3 for 30 time classes was found.

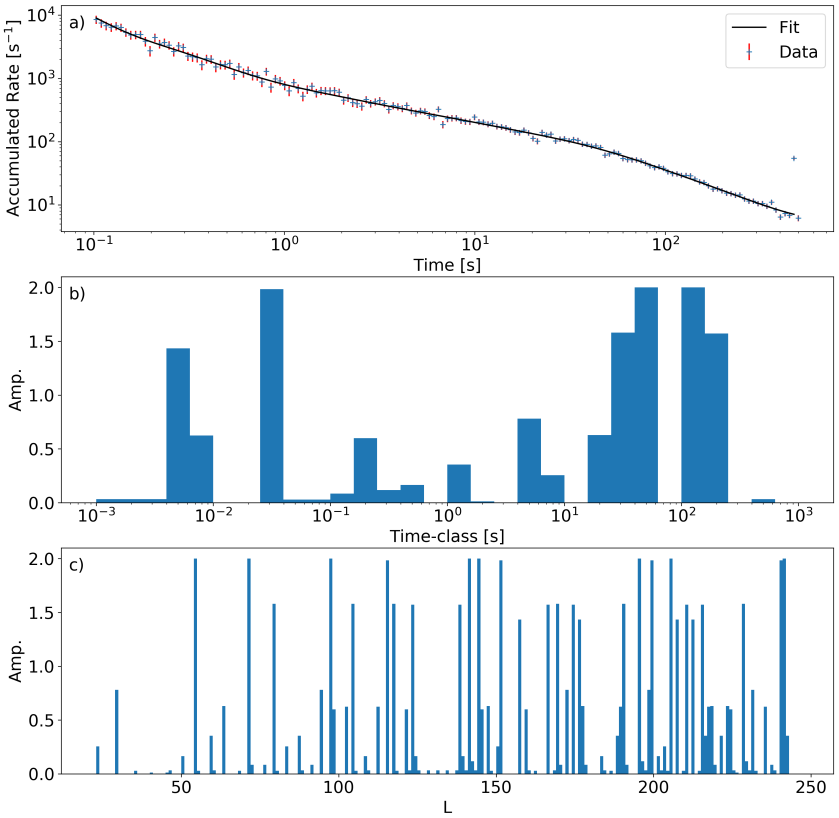

Figure 3.30: The figure shows the decay signal recorded for a measurement of 520 s. a) Shows the normalized count rate which has been fitted by the described method with 36 time classes. b) Displays the time class distribution for a maximum amplitude of 2. c) Demonstrates the to b) equivalent distribution of rotational states.

The derived mean energy of the carbon dimer lies well within in the potential depth of the electronic ground state. The determined mean energy range for the neutral fragment and for the charged fragment is overlapping.

3.6.5 Combining a Boltzmann distribution and Newton's law of cooling

The fit results in chap. 3.6.2, chap. 3.6.3 and chap. 3.6.4 demonstrated the requirement of broad distributions of the rotational states. The vibrational states are assumed to be equally populated. The resulting distribution over all vibrational states is therefore uniform. Combining a single time independent Boltzmann distribution of rotational states with the known tunneling constants of the ro-vibrational states in eqn. (3.21) creates a fit function which is not suited to fit the data. Introducing a time dependency for the Boltzmann distribution over the measurement time, which increases the width of the integrated distribution, might result in a fit in agreement with the data. In a cryogenic environment, a temperature decrease of the ensemble might link the Boltzmann distribution to a time dependency.
Combining the tunneling constants $k(\nu, L)$ derived by LEVEL16 and a single Boltzmann distribution (eqn. 3.24) as distribution of the rotational states in eqn. (3.21) results in a simple fit function. The occupation N_L of the rotational state L assuming, a Boltzmann distribution, is described by:

$$N_L = \frac{N_{All}}{z}(2L+1)e^{-\frac{E(L,0)}{k_B T}}. \tag{3.24}$$

The eqn. (3.24) requires the energy of the rotational state $E(L,0)$ (eqn. 3.20 $\Omega = 0$), the total number of particles N_{All} and the partition sum z. To calculate the partition sum z of the Boltzmann distribution of rotational states for homonuclear dimers, the following equation has to be evaluated:

$$z = 0.5 \sum_{L=0}^{L_{\max}} (2L+1)e^{-\frac{E(L,0)}{\mathrm{k_B} T}}. \tag{3.25}$$

For homonuclear dimers, a symmetry factor of 0.5 has to be included to attribute for the indistinguishable orientations of the dimer. In our cases the partition sum eqn. (3.25) has an upper limit which allows to employ a discrete method for the evaluation. The upper limit is introduced by the behavior of the modified Morse potential. Increasing the rotational quantum number L decreases the depth of the potential well until no solution for the wavefunction exists. Here the solution from LEVEL16 with the highest rotational quantum number was used as limit. To adapt the simple fit function for this work, the Boltzmann distribution (3.24) was modified with the Newton's law of cooling (3.27) to introduce a time dependency for the

temperature of the ensemble:

$$N_l = \frac{N_{\mathrm{All}}}{z}(2L+1)e^{-\frac{E(L,0)}{\mathrm{k_B}T(t)}}. \tag{3.26}$$

Newton's law of cooling describes the cooling of an ensemble with the temperature T_{Start} towards the environmental temperature T_{Env} via an exponential decrease with a cooling rate-constant k:

$$T(t) = (T_{\mathrm{Start}} - T_{\mathrm{Env}})e^{-\mathrm{k_B}t} + T_{\mathrm{Env}}. \tag{3.27}$$

Additionally, a constant offset from the dark count rate c_{Dark} needed to be included for the fit. A maximum of five parameters are needed for the fit: T_{Start},T_{Env},N_{All},k and c_{Dark}. This fit function was tested on measurements of cobalt and silver anionic dimers. Fig. 3.31 and fig. 3.32 show the result from to the data. The upper plot (a)) of both figures shows the fit of the modified Boltzmann distribution to the data. The gray shaded area corresponds to the propagated uncertainties of the individual fit parameters. The middle part of both figures (b)) shows the temperature development over time for the particle ensemble. The blue shaded area corresponds to the propagated uncertainties. The lower part of both figures (c)) demonstrates the time evolution of the Boltzmann distribution over time by changing the temperature. Each Boltzmann distribution corresponds to the equally colored vertical mark in b) (red:$\sim$0.018 s, orange:$\sim$0.5 s, blue:$\sim$2 s, cyan:$\sim$8.1 s). Fig. 3.31 shows the decay of anionic cobalt dimers stored in the CSR for 70 s. 500 time bins haven been chosen, still guaranteeing sufficient statistics in each bin. The decay signal was measured with COMPACT at the charged fragment position. The fit is in good agreement with the data ($\chi^2_{red} = 1.19$). The fit evaluated a starting temperature for the ensemble of 3100 ± 530 K and an environmental temperature of 220 ± 31 K as endpoint. As no dipole interaction is expected, the temperature decrease is relatively strong with an exponent of 0.165 s^{-1} for Newton's cooling law. The high starting temperature could be explained by the production process in a MISS source, as the particles are produced by sputtering. The fit function found a required particle ensemble of 230000 ± 13000, integrated over all injections for the Boltzmann distributions. 144398 events over all injections were counted with COMPACT. Ejecting the residual stored particles from the CSR for the dark count measurement might explain the discrepancy. The dark count rate was estimated by the fit function to 41 ± 16 s^{-1}, integrated over all injections. The dark count rate corresponds, for 102 stored injections, to a mean dark count rate of 0.40 ± 0.16 s^{-1}, which is comparable to previous measurements (e.g.0.41 ± 0.17 s^{-1} [Becker 2016]).

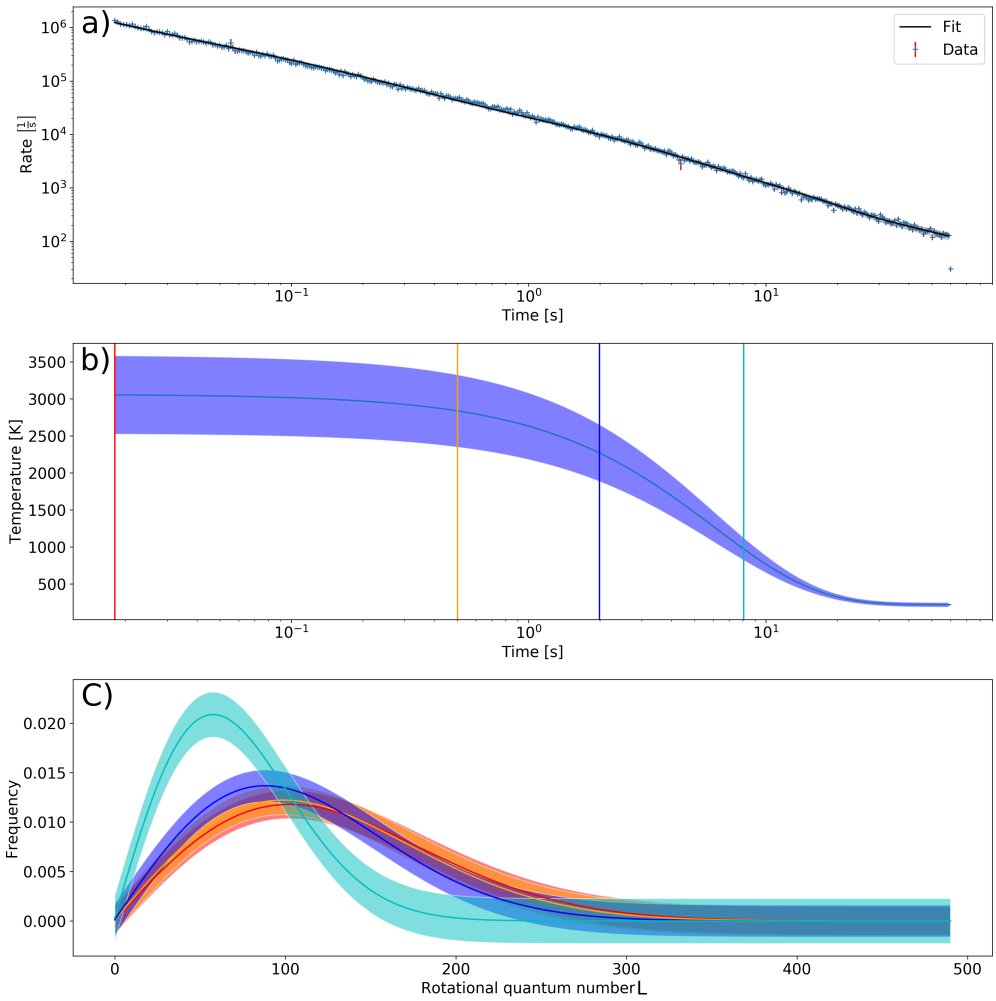

Figure 3.31: The figure is based on the data from an anionic cobalt dimer measurement with a storage time of 70 s. a) Shows the fit to the data with Boltzmann distributions coupled by Newton's law of cooling. b) Demonstrates the time dependent temperature change of the particle ensemble. c) Shows the Boltzmann distributions for the in b) given temperatures at the vertical marks of ∼0.018 s (red), ∼0.5 s (orange), ∼2 s (blue) and ∼8.1 s (cyan).

Fig. 3.32 shows the decay of anionic silver dimers stored for 25 s in the CSR. 500 time bins have been chosen, still guaranteeing sufficient statistics for each bin. The decay signal was acquired with COMPACT at the neutral fragment position. As dimer, mass 216 amu were selected. The fit is in agreement with the decay signal ($\chi^2_{red} = 1.42$). The very low starting temperature of 19 ± 37 K and an environmental temperature of 35000 ± 17000 K was found by the fit to the data. Both temperatures are unlikely to be found in an cryogenic environment or even in the harsh environment of an ion source. The fit function found a required particle ensemble of 39000 ± 1400, integrated over all injections for the Boltzmann distributions.

33425 events over all injections were counted with COMPACT. Ejecting the residual stored particles from the CSR for the dark count measurement might explain the discrepancy. The fit resulted in a dark count rate of 19 ± 20 s^{-1} summed over all injections which corresponds, for 84 stored injections, to a mean dark count rate of 0.23 ± 0.23 s^{-1}. This value agrees well with the previously observed 0.41 ± 0.17 s^{-1} [Becker 2016].

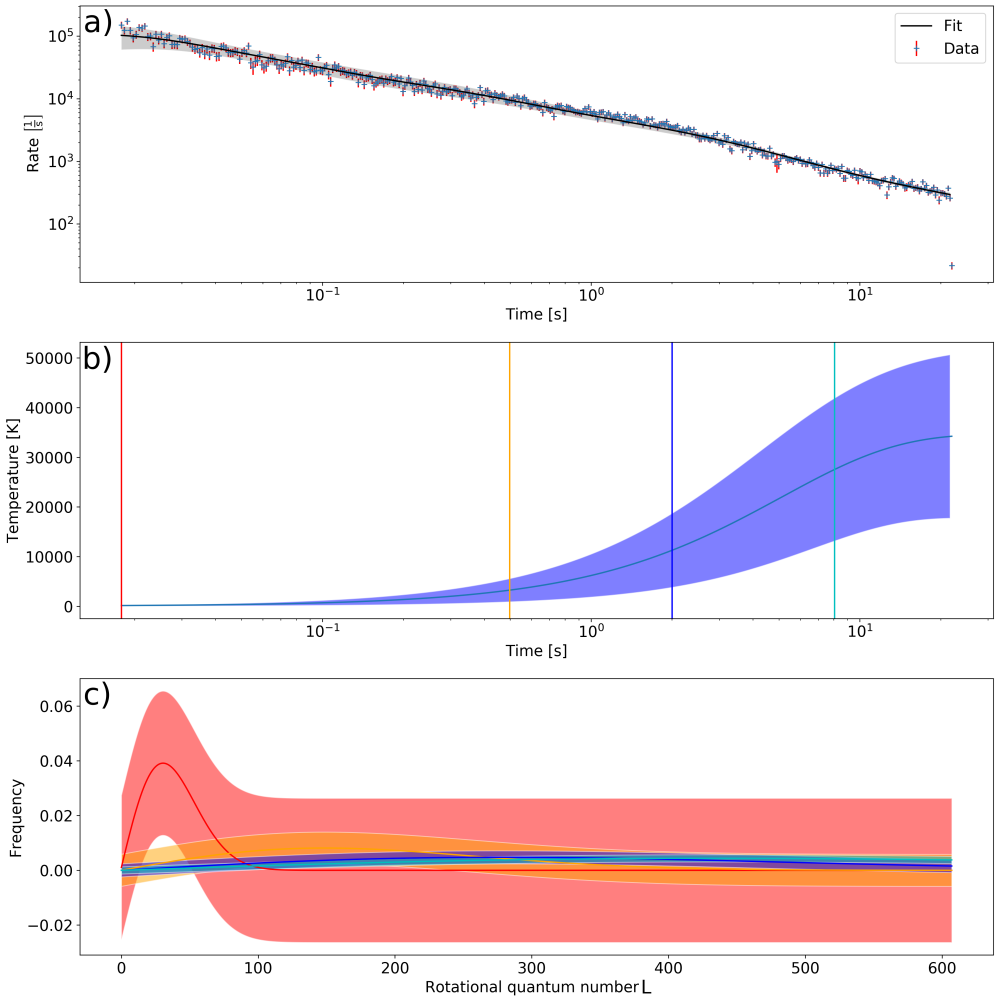

Figure 3.32: The figure is based on the data from an anionic silver dimer measurement with a storage time of 25 s. a) Shows the fit to the data with Boltzmann distributions coupled by Newton's law of cooling. b) Demonstrates the time dependent temperature change of the particle ensemble. c) Shows the Boltzmann distributions for the temperatures given in b) at the vertical marks of ∼0.018 s (red), ∼0.5 s (orange), ∼2 s (blue) and ∼8.1 s (cyan).

The results of the fits are summed up in the tab. 3.12 for better comparison.

Ion	Measurement time [s]	χ^2_{red}	T_{Start} in [K]	T_{Env} in [K]	k_{Newton} in $[s^{-1}]$	$N_{Particles}$	R_{Dark} in $[s^{-1}]$
Co_2^-	70	1.19	3062±531	220±31	0.165± 0.009	230363±13198	41±16
Ag_2^-	25	1.42	19±37	34697±17343	0.196±0.097	39311±1473	19±20

Table 3.12: Fit results for a Boltzmann distribution modified with Newton's cooling law for an anionic silver dimer and an anionic cobalt dimer.

Introducing an upper limit for the environmental temperature and the ensemble start temperature of 20 K respectively of 3500 K in the fit function yielded fits which disagreed with the data. The fit function seems to lack degrees of freedom to be adapted for the silver measurements. The temperature dependence in the fit function describes the cobalt files very well but yields contradictory results for silver measurements.

3.7 Discussion

The discussion in the following is required to evaluate the results from chap. 3.6.1 to 3.6.5.
Chap. 3.6.1 compares the slope of the decay pattern recorded by COMPACT and NICE. For the comparison three measurements were selected. The selection included one measurement of the anionic cobalt dimer and two measurements of the anionic silver dimer. To evaluate the influence of the isotopic composition on the decay pattern a monoisotopic and a heteroisotopic silver dimer were chosen for the demonstration. The MCP based detectors COMPACT and NICE differ in their size and detection efficiency. To match the decay signals recorded by COMPACT and NICE the individual dark count rate of both detector signals has been subtracted. Further more the rate recorded by COMPACT has been scaled by the fraction of rates in the first bin. Each measurement showed two congruent decay signals up to 2 s. Only the dark count rate of NICE limited the comparable time span. The comparison fails as soon as the signal is dominated by the dark count rate. For the fragmentation process as similar slope of the decay rate on both detectors is expected. Electron detachment could affect NICE as the electrons are lost in the CSR and only the neutral fragments are counted. The observed slope of the affected signal would be modified by a second decay process. Only an identical decay signal for the fragmentation process and electron detachment would mask the electron detachment in the explained comparison as linear offset. By comparing the slopes of both decay signals no direct evidence for electron detachment was found. Recent studies indicated a difference between the slope of neutral fragment and charged fragment rates for anionic silver dimers [E. K. Anderson et al. 2020]. For this experiment two MCP based detectors of the same size were employed. The detector efficiency was assumed identical for both detectors. The slope of the decay dignals for the neutral fragment and the charged fragment start to deviate after 10 ms (see fig. 3.33). The process of electron detachment was inferred to cause the difference in the slope of the rates.

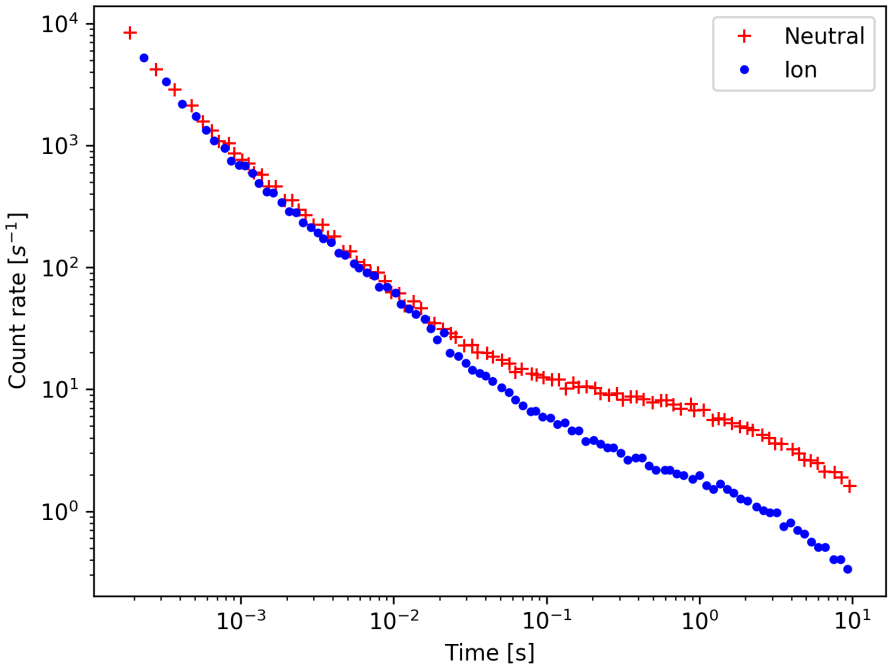

Figure 3.33: Experimental deviation between the neutral count rate and the charged fragment rate observed at DESIREE. The data points were manually extracted from [E. K. Anderson et al. 2020] and plotted for the graph.

Chapter 3.6.2 to 3.6.4 demonstrate fits to the measurements by assuming no distinct internal distribution of states. Former work assumed a continuous equal distribution of states which resulted in a 1/t power law as approximation [Fedor et al. 2005]. For short time periods less than 80 ms, it was shown to fit the observed decay curves for silver and copper anionic dimers. Using the obtained measurements from the CSR the time span could be extended to ∼0.7 s for this simple 1/t power law description. The decay process is based on tunneling. The tunneling constants have been calculated with LEVEL16. The tunneling constants were sorted by their individual times and logarithmically binned in time classes. The amplitudes from the time classes defined the weight of the individual exponential decays of the tunneling process. A distribution of up to 120 time classes could be fit to the data. The amplitudes of the time classes were limited to 2 which prevents an overpopulation of a single state. The resulting fits are in good agreement with the data. The distribution of rotational states derived from the fit is broad and integrates over the measurement time. The derived mean energy from the fits showed a distinct difference between the measured dimers. Each dimer has a certain mean energy range. For example the mean energy for the anionic cobalt dimer ranges from 1.36 eV to 1.39 eV whereas the mean energy for the anionic silver dimer ranges between 0.80 eV and 1.00 eV. The mean energy of the anionic carbon dimer ranges from 5.47 eV to 6.33 eV. The calculated mean energy lies well within the potential depth (C_2^-: -8.11 eV, Co_2^-: 1.768 eV, Ag_2^-: 1.37 eV)

To reduce the degrees of freedom for the fit and to implement a distribution which changes over time a Boltzmann distribution was coupled with Newton's law of cooling in a fit function in chap. 3.6.5. The fit agreed with the data for the anionic cobalt dimers with reasonable temperatures. Introducing this fit function to the silver measurements reveal an unexpected behavior. The temperature requirements were extreme, the parameter for the blackbody environment in the CSR was estimated to 35000 K whereas the parameter for the starting temperature in the ion source was estimated to be below 20 K. The environmental temperature is unlikely to fit the cryogenic surface of the storage ring with a temperature of 4 to 6 K. The ion source used here was of the MISS type. For these ion sources a high starting temperature is expected [Breitenfeldt et al. 2018]. Limiting the boundaries to more reasonable values produced no fit agreement for the anionic silver dimers. The derived fit function agrees with the measurement but fails in reproducing reliable environmental conditions for all tested dimers. It was shown for two approaches that the derived tunneling constants could be used to fit the data in good agreement. The required distribution of stats is in contrast difficult to derive due to the high number of degrees of freedom.

4 Summary and Outlook

During this work, the Cryogenic Trap for Fast ion beam (CTF) was equipped with a mid-IR detection system in order to introduce Laser-Induced Vibrational Emission (LIVE) spectroscopy. The aim is to expand the principle method of gas-phase fluorescence spectroscopy to large, carbon-rich ions of Polycyclic Aromatic Hydrocarbons (PAH) or fullerene. The fluorescence of these ions is expected in the mid-infrared spectral region which is not accessible by conventional fluorescence spectroscopy. Currently the CTF has been modified to suppress the infrared background radiation. At the injection of the CTF, a cryogenic aperture has been installed to reduce the infrared flux from the source beamline. Additionally, a passively cooled cryogenic multi-layer copper shield has been installed at the back of the CTF, replacing a MCP detector and blocking the infrared radiation background from the main laser viewport. Furthermore the remaining laser viewports have been sealed. The remaining infrared background still saturated the detector. In the last test a graphite coated shield surrounding the detector with two apertures for the stored ions has been introduced. The results are promising, as the detection system was not saturated. Further modifications and tests are required to demonstrate a gas-phase fluorescence spectroscopy with this device.
Additionally, this work examined the autofragmentation decay of anionic dimers of carbon, cobalt and silver. The rates between neutral fragments and charged fragments for cobalt and silver dimers were compared. Up to 2 s no deviation between the neutral and the fragment rate was found. The observation time was limited by the high dark count rate of the NICE detector and the resulting high uncertainty. To increase the observation time two comparable COMPACT detectors could be used. After the normalization of both detectors, the rates could be compared directly over 2 s with similar uncertainties. For each examined dimer (C_2^-, Co_2^- and Ag_2^-) the tunneling constants through the potential barrier was calculated with LEVEL 16. The tunneling constants were calculated in order to construct a fit function which attributes to the deviations observed from the strict 1/t power law. A fit function was constructed under the usage of time classes which sorted the decay constants in time bins. The fits showed good agreement to the data. A derived mean energy can be attributed to each dimer measurement. The heuristic description of the data with a distribution based on time classes is of limited use due to the large number of degrees of freedom. The broad distribution derived from the time classes and the possible change of the temperature of the ensemble introduced the idea to fit a time dependent distribution of rotational excitation. A second fit function which imposed on the Boltzmann distribution for the rotational excitation Newton's law of cooling was derived. The fit function are in good agreement to the data. The solutions of

the fit functions for the anionic silver dimers and the anionic cobalt dimers increasing as well decreasing temperatures. The found environmental conditions for the anionic silver dimer are also not possible inside the CSR and the used ion source. Limiting the parameter range of the fit function for the anionic silver dimer to ranges which would correspond to a deceasing temperature of the ensemble resulted in fits disagreeing with the data. It is safe to assume that the results for the anionic cobalt dimers are accidental in the range of possible temperatures. The constructed fit function with the time dependent temperature is unsuited to describe the nature of the observed decay. The missing dipole moment of the symmetric dimers suggest at most higher order multipole moments for cooling, which have long life times, possible exceeding the maximum storage time of the CSR. For the anionic silver dimers and the anionic cobalt dimers, to our best knowledge, no calculation of higher order multipole cooling lifetimes exist, but for a comparable homonuclear diatomic cation the life time was estimated to be in the order of days [Peek, Hashemi-Attar, and Beckel 1979]. The long cooling lifetime of higher order mulitpoles makes an observed cooling of the anions unlikely. Furthermore the disagreeing fit results support this argument.

Part I

Appendix

A Lists

A.1 List of Figures

A.2 List of Tables

A.3 Abbreviations

- **amu** atomic mass unit
- **a.u.** arbitrary units
- **BIB** Blocked Impurity Band
- **Chap.** Chapter

- **COMPACT** COld Movable PArticle CounTer
- **CSR** Cryogenic Storage Ring
- **CTF** Cryogenic Trap for Fast ion beams
- **DIBs** Diffuse Interstellar Bands
- **E-Cool** Electron Cooler
- **e.g**. for example
- **EIBT** Electrostatic Ion Beam Trap
- **ESR** Experimental Storage Ring
- **Fig.** Figure
- **FPGA** Field-Programmable Gate Array
- **GSI** Gesellschaft für SchwerIonenforschung
- **HV** High-Voltage
- **i.a.** amongst other things
- **JFET** Junction gate Field-Effect Transistor
- **LIVE** Laser Induced Vibrational Emission
- **MCP** Micro-Channel Plate
- **MISS** Middelton Ion Sputter Source
- **MPIK** Max-Planck-Institut für Kernphysik
- **MR ToF** Multi-Reflection Time-of-Flight Mass-Spectrometer
- **NICE** Neutral Imagining in Cryogenic Environment
- **NIST** National Institute of Standards and Technology (USA)
- **OPO** Optical Parametric Oscillator
- **PAH** Poly Aromatic Hydrocarbons
- **RF** Radio Frequency
- **Tab.** Table
- **TIA** TransImpedance Amplifier

- **ToF** Time-Of-Flight
- **UIR** Unidentified InfraRed emission bands
- **WKB** Wentzel-Brillouin-Kramers ansatz

B Publications

Cited publications

[Breitenfeldt et al. 2018] Breitenfeldt, C., K. Blaum, S. George, J. Göck, G. Guzmán-Ramírez, J. Karthein, T. Kolling, M. Lange, S. Menk, C. Meyer, J. Mohrbach, G. Niedner-Schatteburg, D. Schwalm, L. Schweikhard, and A. Wolf. "Long-term monitoring of the internal energy distribution of isolated cluster systems". In: *Physical Review Letters* 120.25 (2018), p. 253001.

[Hahn et al. 2016] Hahn, R. von, A. Becker, F. Berg, K. Blaum, C. Breitenfeldt, H. Fadil, F. Fellenberger, M. W. Froese, S. George, J. Göck, M. Grieser, F. Grussie, E. A. Guerin, O. Heber, P. Herwig, J. Karthein, C. Krantz, H. Kreckel, M. Lange, F. Laux, S. Lohmann, S. Menk, C. Meyer, P. M. Mishra, O. Novotný, A. P. O'Connor, D. A. Orlov, M. L. Rappaport, R. Repnow, S. Saurabh, S. Schippers, C. D. Schröter, D. Schwalm, L. Schweikhard, T. Sieber, A. Shornikov, K. Spruck, S. Sunil Kumar, J. Ullrich, X. Urbain, S. Vogel, P. Wilhelm, A. Wolf, and D. Zajfman. "The cryogenic storage ring CSR". in: *Review of Scientific Instruments* 87.6 (2016), p. 063115.

[Meyer et al. 2017] Meyer, C., A. Becker, K. Blaum, C. Breitenfeldt, S. George, J. Göck, M. Grieser, F. Grussie, E. A. Guerin, R. von Hahn, P. Herwig, C. Krantz, H. Kreckel, J. Lion, S. Lohmann, P. M. Mishra, O. Novotný, A. P. O'Connor, R. Repnow, S. Saurabh, D. Schwalm, L. Schweikhard, K. Spruck, S. Sunil Kumar, S. Vogel, and A. Wolf. "Radiative Rotational Lifetimes and State-Resolved Relative Detachment Cross Sections from Photodetachment Thermometry of Molecular Anions in a Cryogenic Storage Ring". In: *Physical Review Letters* 119 (2 2017), p. 023202.

[O'Connor et al. 2016] O'Connor, A. P., A. Becker, K. Blaum, C. Breitenfeldt, S. George, J. Göck, M. Grieser, F. Grussie, E. A. Guerin, R. von Hahn, U. Hechtfischer, P. Herwig, J. Karthein, C. Krantz, H. Kreckel, S. Lohmann, C. Meyer, P. M. Mishra, O. Novotný, R. Repnow, S. Saurabh, D. Schwalm, K. Spruck, S. Sunil Kumar, S. Vogel, and A. Wolf. "Photodissociation of an Internally Cold Beam of CH^+ Ions in a Cryogenic Storage Ring". In: *Physical Review Letters* 116 (11 2016), p. 113002.

Uncited publications

[Novotný et al. 2019] Novotný, O., P. Wilhelm, D. Paul, Á. Kálosi, S. Saurabh, A. Becker, K. Blaum, S. George, J. Göck, M. Grieser, F. Grussie, R. von Hahn, C. Krantz, H. Kreckel, C. Meyer, P. M. Mishra, D. Muell, F. Nuesslein, D. A.

Orlov, M. Rimmler, V. C. Schmidt, A. Shornikov, A. S. Terekhov, S. Vogel, D. Zajfman, and A. Wolf. "Quantum-state–selective electron recombination studies suggest enhanced abundance of primordial HeH+". In: *Science* 365.6454 (2019), pp. 676–679.

C Bibliography

[E. K. Anderson et al. 2020] Anderson, E. K., A. F. Schmidt-May, P. K. Najeeb, G. Eklund, K. C. Chartkunchand, S. Rosén, Å. Larson, K. Hansen, H. Cederquist, H. Zettergren, and H. T. Schmidt. "Spontaneous Electron Emission from Hot Silver Dimer Anions: Breakdown of the Born-Oppenheimer Approximation". In: *Phys. Rev. Lett.* 124 (17 2020), p. 173001. DOI: 10.1103/PhysRevLett.124.173001.

[J. D. Anderson 1982] Anderson, J. D. *Modern Compressible Flow: With Historical Perspective*. McGraw-Hill Book Company, 1982. ISBN: 0070016542.

[Becker 2016] Becker, A. "Imaging of Neutral Fragmentation Products from Fast Molecular Ion Beams: Paving the Way for Reaction Studies in Cryogenic Environment". Thesis. Ruprecht-Karls-Universität Heidelberg, 2016.

[Blaum] Blaum, K. *MISS-HD sputter source*. (Accessed: 06/28/2020). URL: https://leonid.arc.nasa.gov/DIBcatalog.html.

[Breitenfeldt et al. 2018] Breitenfeldt, C., K. Blaum, S. George, J. Göck, G. Guzmán-Ramírez, J. Karthein, T. Kolling, M. Lange, S. Menk, C. Meyer, J. Mohrbach, G. Niedner-Schatteburg, D. Schwalm, L. Schweikhard, and A. Wolf. "Long-term monitoring of the internal energy distribution of isolated cluster systems". In: *Physical Review Letters* 120.25 (2018), p. 253001.

[Campbell et al. 2015] Campbell, E. K., M. Holz, D. Gerlich, and J. P. Maier. "Laboratory confirmation of C_{60}^+ as the carrier of two diffuse interstellar bands". In: *Nature* 523.7560 (2015), p. 322.

[Chen et al. 1994] Chen, Z., I. Ben-Itzhak, C. D. Lin, W. Koch, G. Frenking, I. Gertner, and B. Rosner. "Mean-lifetime calculations of the metastable doubly charged NeAr 2+ rare-gas dimer". In: *Physical Review A* 49.5 (1994), p. 3472.

[Cook et al. 1996] Cook, D. J., S. Schlemmer, N. Balucani, D. R. Wagner, B. Steiner, and R. J. Saykally. "Infrared emission spectra of candidate interstellar aromatic molecules". In: *Nature* 380.6571 (1996), pp. 227–229.

[Demtröder 2018] Demtröder, W. "Diatomic Molecules". In: *Atoms, Molecules and Photons: An Introduction to Atomic-, Molecular- and Quantum Physics*. Berlin, Heidelberg: Springer Berlin Heidelberg, 2018, pp. 305–355. ISBN: 978-3-662-55523-1.

[Eland 1996] Eland J. H. D. and Schmidt, V. "Coincidence Measurements on Ions and Electrons". In: *VUV and Soft X-Ray Photoionization*. Ed. by D. A. Becker U. and Shirley. Boston, MA: Springer US, 1996, pp. 495–520. ISBN: 978-1-4613-0315-2. DOI: 10.1007/978-1-4613-0315-2_14.

[Ervin and Lineberger 1991] Ervin, K. M. and W. C. Lineberger. "Photoelectron spectra of dicarbon (1-) and ethynyl (1-)". In: *The Journal of Physical Chemistry*

95.3 (1991), pp. 1167–1177.

[Fedor et al. 2005] Fedor, J., K. Hansen, J. U. Andersen, and P. H̃velplund. "Non-thermal Power Law Decay of Metal Dimer Anions". In: *Physical Review Letters* 94 (11 2005), p. 113201. DOI: 10.1103/PhysRevLett.94.113201.

[Foing and Ehrenfreund 1994] Foing, B. H. and P. Ehrenfreund. "Detection of two interstellar absorption bands coincident with spectral features of C_{60}^+". In: *Nature* 369 (1994), pp. 296–298.

[Fulara, Jakobi, and Maier 1993] Fulara, J., M. Jakobi, and J. P. Maier. "Electronic and infrared spectra of C_{60}^+ and C_{60}^- in neon and argon matrices". In: *Chemical Physics Letters* 211 (1993), pp. 227–234.

[Gamow 1928] Gamow, G. "Zur quantentheorie des atomkernes". In: *Zeitschrift für Physik* 51.3-4 (1928), pp. 204–212.

[Gatchell et al. 2014] Gatchell, M., H. T. Schmidt, R. D. Thomas, S . Rosén, P. Reinhed, P. Löfgren, L. Brännholm, M. Blom, M. Björkhage, E. Bäckström, J. D. Alexander, S. Leontein, D. Hanstorp, H. Zettergren, L. Liljeby, A. Källberg, A. Simonsson, F. Hellberg, S. Mannervik, M. Larsson, W. D. Geppert, K. G. Rensfelt, H. Danared, A. Paál, M. Masuda, P. Halldén, G. Andler, M. H. Stockett, T. Chen, G. Källersjö, J. Weimer, K. Hansen, H. Hartman, and H. Cederquist. "Commissioning of the DESIREE storage rings – a new facility for cold ion-ion collisions". In: *Journal of Physics: Conference Series* 488.1 (2014), p. 012040.

[Grieser 2019] Grieser, M. personal communication. Sept. 2019.

[Haberstroh 2011] Haberstroh, C. *Sicherheitsbetrachtung CTF*. tech. rep. Technische Universität Dresden: Fakultät Maschinenwesen, Institut für Energietechnik, Bitzer Stiftungsprofessur für Kälte-, Kryo- und Kompressorentechnik, 2011.

[Hahn et al. 2016] Hahn, R. von, A. Becker, F. Berg, K. Blaum, C. Breitenfeldt, H. Fadil, F. Fellenberger, M. W. Froese, S. George, J. Göck, M. Grieser, F. Grussie, E. A. Guerin, O. Heber, P. Herwig, J. Karthein, C. Krantz, H. Kreckel, M. Lange, F. Laux, S. Lohmann, S. Menk, C. Meyer, P. M. Mishra, O. Novotný, A. P. O'Connor, D. A. Orlov, M. L. Rappaport, R. Repnow, S. Saurabh, S. Schippers, C. D. Schröter, D. Schwalm, L. Schweikhard, T. Sieber, A. Shornikov, K. Spruck, S. Sunil Kumar, J. Ullrich, X. Urbain, S. Vogel, P. Wilhelm, A. Wolf, and D. Zajfman. "The cryogenic storage ring CSR". in: *Review of Scientific Instruments* 87.6 (2016), p. 063115.

[Hales et al. 1994] Hales, D. A., C.-X. Su, L. Lian, and P. B. Armentrout. "Collision-induced dissociation of Co_n^+ (n= 2–18) with Xe: Bond energies of cationic and neutral cobalt clusters, dissociation pathways, and structures". In: *The Journal of Chemical Physics* 100.2 (1994), pp. 1049–1057.

[Heger 1922] Heger, M. L. "Further study of the sodium lines in class B stars". In: *Lick Observatory Bulletin* 10.337 (1922), pp. 141–145.

[Ho, Ervin, and Lineberger 1990] Ho, J., K. M. Ervin, and W. C. Lineberger. "Photoelectron spectroscopy of metal cluster anions: Cu_n^-, Ag_n^-, and Au_n^-". In: *The Journal of Chemical Physics* 93.10 (1990), pp. 6987–7002. DOI: 10.1063/1.459475.

[Ho, Polak, et al. 1993] Ho, J., M. L. Polak, K. M. Ervin, and W. C. Lineberger.

"Photoelectron spectroscopy of nickel group dimers: Ni_2^-, Pd_2^-, and Pt_2^-". In: *The Journal of Chemical Physics* 99.11 (1993), pp. 8542–8551.

[Hobbs, York, Snow, et al. 2008] Hobbs, L. M., D. G. York, T. P. Snow, T. Oka, Thorburn J. A., Bishof M., S. D. Friedman, B. J. McCall, B. Rachford, P. Sonnentrucker, and D. E. Welty. "A Catalog of Diffuse Interstellar Bands in the Spectrum of HD 204827". In: *The Astrophysical Journal* 680.2 (June 2008), pp. 1256–1270. DOI: 10.1086/587930. URL: https://doi.org/10.1086%2F587930.

[Hobbs, York, Thorburn, et al. 2009] Hobbs, L. M., D. G. York, J. A. Thorburn, T. P. Snow, M. Bishof, S. D. Friedman, B. J. McCall, T. Oka, B. Rachford, P. Sonnentrucker, and D. E. Welty. "STUDIES OF THE DIFFUSE INTERSTELLAR BANDS. III. HD 183143". In: *The Astrophysical Journal* 705.1 (Oct. 2009), pp. 32–45. DOI: 10.1088/0004-637x/705/1/32. URL: https://doi.org/10.1088%2F0004-637x%2F705%2F1%2F32.

[Hou et al. 2020] Hou, C.-C., H.-F. Wang, C. Li, and Q. Xu. "From Metal-Organic Frameworks to Single/Dual-Atom and Cluster Metal Catalysts for Energy Applications". In: *Energy & Environmental Science* (2020). DOI: 10.1039/C9EE04040D.

[Jenniskens] Jenniskens, P. M. *Diffuse Interstellar Band Catalog*. Ed. by P. M. Jenniskens. (Accessed: 08/31/2019). URL: https://leonid.arc.nasa.gov/DIBcatalog.html.

[Kark 2014] Kark, K. W. "Aperturstrahler V (Schwarzer Strahler)". In: *Antennen und Strahlungsfelder: Elektromagnetische Wellen auf Leitungen, im Freiraum und ihre Abstrahlung*. Eqn. 17.3, p.414. Wiesbaden: Springer Fachmedien Wiesbaden, 2014, pp. 413–430.

[Kroto 1987] Kroto, H. W. *Polycyclic Aromatic Hydrocarbons and Astrophysics*. Dordrecht: Springer Netherlands, 1987, pp. 197–206. ISBN: 978-94-009-4776-4.

[Lange, Blaum, et al. 2008] Lange, M., K. Blaum, M. W. Froese, M. Grieser, O. Heber, D. Kaiser, S. Menk, D. A. Orlov, M. Rappaport, A. Shornikov, T. Sieber, Y. Toker, J. Varju, R. von Hahn, A. Wolf, and D. Zajfman. "Commissioning of the Heidelberg Cryogenic Trap for Fast Ion Beams (CTF)". in: *MOPC110, EPAC08 Proceedings* (2008).

[Lange, Froese, et al. 2010] Lange, M., M. W. Froese, S. Menk, J. Varju, R. Bastert, K. Blaum, J. R. Crespo López-Urrutia, F. Fellenberger, M. Grieser, R. von Hahn, O. Heber, K. U. Kühnel, F. Laux, Orlov D. A., Rappaport M. L., R. Repnow, C. D. Schröter, D. Schwalm, A. Shornikov, T. Sieber, Y. Toker, J. Ullrich, A. Wolf, and D. Zajfman. "A cryogenic electrostatic trap for long-time storage of keV ion beams". In: *Review of Scientific Instruments* 81.5 (2010), p. 055105.

[R. J. Le Roy 2017] Le Roy, R. J. "LEVEL: A computer program for solving the radial Schrödinger equation for bound and quasibound levels". In: *Journal of Quantitative Spectroscopy and Radiative Transfer* 186 (2017), pp. 167–178.

[Robert J Le Roy and Liu 1978] Le Roy, Robert J and Wing-Ki Liu. "Energies and widths of quasibound levels (orbiting resonances) for spherical potentials". In: *The Journal of Chemical Physics* 69.8 (1978), pp. 3622–3631.

[Léger, d'Hendecourt, and Defourneau 1989] Léger, A., L. d'Hendecourt, and D. Defourneau. "Physics of IR emission by interstellar PAH molecules". In: *Astronomy and Astrophysics* 216 (1989), pp. 148–164.

[Lemmon, McLinden, and Friend 2020] Lemmon, E. W., M. O. McLinden, and D. G. Friend. "Thermophysical properties of fluid systems". In: *NIST Chemistry webbook, NIST Standard reference database*. Ed. by P. J. Linstrom and W. G. Mallard. Vol. 69. Gaithersburg MD, 20899, USA: National Institute of Standards and Technology, 2020. URL: https://doi.org/10.18434/T4D303.

[Leopold, Almlöf, et al. 1988] Leopold, D. G., J. Almlöf, W. C. Lineberger, and P. R. Taylor. "A simple interpretation of the Fe_2^- photoelectron spectrum". In: *The Journal of Chemical Physics* 88.6 (1988), pp. 3780–3783.

[Leopold and Lineberger 1986] Leopold, D. G. and W. C. Lineberger. "A study of the low-lying electronic states of Fe_2 and Co_2 by negative ion photoelectron spectroscopy". In: *The Journal of Chemical Physics* 85.1 (1986), pp. 51–55.

[Mellouki, Bennaji, and Yacoubi 2007] Mellouki, I., N. Bennaji, and N. Yacoubi. "IR characterization of graphite black-coating for cryogenic detectors". In: *Infrared Physics & Technology* 50.1 (2007), pp. 58–62. ISSN: 1350-4495. DOI: https://doi.org/10.1016/j.infrared.2006.05.002.

[Menk 2013] Menk, S. "Vibrational Auto-Detachment of the Sulfur Hexafluoride Anion in a Low-background Cryogenic Ion Beam Trap". Thesis. Ruprecht-Karls-Universität Heidelberg, 2013.

[Meyer et al. 2017] Meyer, C., A. Becker, K. Blaum, C. Breitenfeldt, S. George, J. Göck, M. Grieser, F. Grussie, E. A. Guerin, R. von Hahn, P. Herwig, C. Krantz, H. Kreckel, J. Lion, S. Lohmann, P. M. Mishra, O. Novotný, A. P. O'Connor, R. Repnow, S. Saurabh, D. Schwalm, L. Schweikhard, K. Spruck, S. Sunil Kumar, S. Vogel, and A. Wolf. "Radiative Rotational Lifetimes and State-Resolved Relative Detachment Cross Sections from Photodetachment Thermometry of Molecular Anions in a Cryogenic Storage Ring". In: *Physical Review Letters* 119 (2 2017), p. 023202.

[Namba and Tsuwa 1980] Namba, Y. and H. Tsuwa. "Surface properties of polished stainless steel". In: *CIRP Annals* 29.1 (1980), pp. 409–412.

[O'Connor et al. 2016] O'Connor, A. P., A. Becker, K. Blaum, C. Breitenfeldt, S. George, J. Göck, M. Grieser, F. Grussie, E. A. Guerin, R. von Hahn, U. Hechtfischer, P. Herwig, J. Karthein, C. Krantz, H. Kreckel, S. Lohmann, C. Meyer, P. M. Mishra, O. Novotný, R. Repnow, S. Saurabh, D. Schwalm, K. Spruck, S. Sunil Kumar, S. Vogel, and A. Wolf. "Photodissociation of an Internally Cold Beam of CH^+ Ions in a Cryogenic Storage Ring". In: *Physical Review Letters* 116 (11 2016), p. 113002.

[Oja and Suuberg 1998] Oja, V. and E. M. Suuberg. "Vapor pressures and enthalpies of sublimation of polycyclic aromatic hydrocarbons and their derivatives". In: *Journal of Chemical & Engineering Data* 43.3 (1998), pp. 486–492.

[Pang 1997] Pang, T. *Introduction to Computatinal Physics*. Cambridge, England: Cambridge University Press, 1997.

[Pedersen et al. 1998] Pedersen, H. B., C. Brink, L. H. Andersen, N. Bjerre,

P. Hvelplund, D. Kella, and H. Shen. "Experimental investigation of radiative lifetimes of vibrational levels at the electronic ground state of C 2-". In: *The Journal of chemical physics* 109.14 (1998), pp. 5849–5855.

[Peek, Hashemi-Attar, and Beckel 1979] Peek, J. M., A.-R. Hashemi-Attar, and C. L. Beckel. "Spontaneous emission lifetimes in the ground electronic states of HD+ and H2+". In: *The Journal of Chemical Physics* 71.12 (1979), pp. 5382–5383.

[Rahman and Schiffer 1986] Rahman, A. and J. P. Schiffer. "Structure of a one-component plasma in an external field: a molecular-dynamics study of particle arrangement in a heavy-ion storage ring". In: *Physical review letters* 57.9 (1986), p. 1133.

[Schlemmer et al. 1994] Schlemmer, S., D. J. Cook, J. A. Harrison, B. Wurfel, W. Chapman, and R. J. Saykally. "The unidentified interstellar infrared bands: PAHs as carriers?" In: *Science* 265.5179 (1994), pp. 1686–1689.

[Schmidt et al. 2017] Schmidt, H. T., G. Eklund, K. C. Chartkunchand, E. K. Anderson, M. Kamińska, N. de Ruette, R. D. Thomas, M. K. Kristiansson, M. Gatchell, P. Reinhed, S. Rosén, A. Simonsson, A. Källberg, P. Löfgren, S. Mannervik, H. Zettergren, and H. Cederquist. "Rotationally Cold OH^- Ions in the Cryogenic Electrostatic Ion-Beam Storage Ring DESIREE". in: *Physical Reviev Letters* 119 (7 2017), p. 073001.

[Schmidt et al. 2018]– "Erratum: Rotationally Cold OH^- Ions in the Cryogenic Electrostatic Ion-Beam Storage Ring DESIREE [Phys. Rev. Lett. 119, 073001 (2017)]". In: *Physical Review Letters* 121 (7 2018), p. 079901.

[Seelig et al. 1998] Seelig, P., S. Borneis, A. Dax, T. Engel, S. Faber, M. Gerlach, C. Holbrow, G. Huber, T. Kühl, D. Marx, K. Meier, P. Merz, W. Quint, F. Schmitt, M. Tomaselli, L. Völker, H. Winter, M. Würtz, K. Beckert, B. Franzke, F. Nolden, H. Reich, M. Steck, and T. Winkler. "Ground State Hyperfine Splitting of Hydrogenlike $^{207}Pb^{81+}$ by Laser Excitation of a Bunched Ion Beam in the GSI Experimental Storage Ring". In: *Phys. Rev. Lett.* 81 (22 1998), pp. 4824–4827. DOI: 10.1103/PhysRevLett.81.4824.

[Spruck et al. 2015] Spruck, K., A. Becker, F. Fellenberger, M. Grieser, R. von Hahn, V. Klinkhamer, O. Novotný, S. Schippers, S. Vogel, A. Wolf, and C. Krantz. "An efficient, movable single-particle detector for use in cryogenic ultra-high vacuum environments". In: *Review of Scientific Instruments* 86.2 (2015), p. 023303.

[Sunil and Jordan 1988] Sunil, K. K. and K.D. Jordan. "Determination of the energies and spectroscopic constants of the low-lying electronic states of aluminum dimers (Al_2, Al_2^+, an Al_2^-)". In: *The Journal of Physical Chemistry* 92.10 (1988), pp. 2774–2781.

[Tielens 2008] Tielens, A. G. G. M. "Interstellar Polycyclic Aromatic Hydrocarbon Molecules". In: *Annual Review of Astronomy and Astrophysics* 46.1 (2008), pp. 289–337.

[Touschek 1961] Touschek, B. "The Frascati storage rings". In: (1961).

[Walker et al. 2015] Walker, G. A. H., D. A. Bohlender, J. P. Maier, and E. K. Campbell. "Identification of more interstellar C_{60}^+ bands". In: *The Astrophysical*

Journal 812.1 (2015), p. L8.

[Wiza 1979] Wiza, J. L. "Microchannel plate detectors". In: *Nuclear Instruments and Methods* 162.1-3 (1979), pp. 587–601.

[Wollnik and Przewloka 1990] Wollnik, H. and M. Przewloka. "Time-of-flight mass spectrometers with multiply reflected ion trajectories". In: *International Journal of Mass Spectrometry and Ion Processes* 96.3 (1990), pp. 267–274.

[Zajfman et al. 1997] Zajfman, D., O. Heber, L. Vejby-Christensen, I. Ben-Itzhak, M. Rappaport, R. Fishman, and M. Dahan. "Electrostatic bottle for long-time storage of fast ion beams". In: *Physical Review A* 55 (3 1997), R1577–R1580.

Danksagung

An dieser Stelle möchte ich den Menschen danken, die mich in allen Phasen meiner Doktorarbeit unterstützt haben.

Besonderen Dank geht an Prof. Dr. Klaus Blaum, der es mir ermöglicht hat meine Doktorarbeit über Messungen am tiefkalten Speicherring CSR und das LIVE Projekt an der tiefkalten Ionenfalle CTF anzufertigen.

Ebenfalls möchte ich Priv.-Doz. Dr. Robert Moshammer für die Begutachtung meiner Arbeit danken.

Bei Dr. Sebastian George möchte ich mich ganz besonders bedanken für die jahrelange Betreuung in physikalischen Fragen und die Unterstützung auch in persönlich schwierigen Situationen.

Meinen Kollegen vom LIVE Projekt Ulrich Grötzinger, Dr. Holger Kreckel und Dr. Sunil Kumar Sudhakaran möchte ich für die unerschütterliche Zusammenarbeit danken.

Bei Dr. Oldřich Novotný möchte ich mich für die unermüdliche Hilfestellung bei Fragen zur Datenaufnahme und den Detektoren bedanken.

Dr. Christian Meyer, Felix Nüßlein und Viviane Schmidt gilt auch meine Dankbarkeit für die vielen Diskussionen und die vorhandene Hilfsbereitschaft.

Mein Dank gilt auch Dr. Robert von Hahn der mir jeder Zeit sein offenes Ohr geliehen hat und mir gegebenenfalls Hilfe zur Verfügung gestellt hat.

Auch bei Dr. Manfred Grießer, Dr. Florian Grussie, Damian Müll, Daniel Paul und Prof. Dr. Andreas Wolf möchte ich mich für die aufmunternde Worte, die gelegentliche Hilfestellung und die obligatorischen wissenschaftlichen Diskussionen bedanken.

Dirk Kaiser, der Werkstatt unter der Leitung von Christian Kaiser, den Operateuren unter der Leitung von Manfred König sowie dem Elektronik-Labor (Rolf Epking, Oliver Koschorreck, Peter Werle und Natalie Zahn) möchte ich für die unzähligen Reparaturen, Modifikationen und Beratungen in letzter Minute danken.

Zum Schluss möchte ich noch meiner Mutter danken. Sie hat mich immer ermutigt und in jeder Lage unterstützt. Ohne sie wäre dieses Studium so nicht möglich gewesen. Auch meinen Freunden gilt großer Dank. Sie haben mich spontan aus dem Trott gerissen und Dingen neuen Schwung sowie einen anderen Blickwinkel verliehen.

Danke!